ORGANIZATION OF BACTERIAL CELL DIVISION RING, AND BACTERIAL MORPHOLOGY AND GROWTH UNDER MECHANICAL COMPRESSION

by

Fangwei Si

A dissertation submitted to The Johns Hopkins University in conformity with the requirements for the degree of Doctor of Philosophy.

Baltimore, Maryland

August, 2015

© Fangwei Si 2015

All rights reserved

Abstract

This dissertation studies fundamental questions in biomechanics and biophysics of bacterial cell division. Specifically, we examine morphology and growth of prototypical bacterial cells by employing both experimental and theoretical tools. We use novel techniques in fluorescence microscopy and microfluidics to reveal the organization of the bacterial division ring (Z-ring). We also examine bacterial morphology and growth under mechanical compression, and explain the experimental data using existing mechanochemical models.

The bacterial division ring (Z-ring) is essential for cytokinesis in bacteria. The Z-ring is a ring-shaped cell division complex and whose primary component is FtsZ, a filamentous tubulin homologue that serves as a scaffold for the recruitment of other cell division related proteins. FtsZ forms filaments and bundles. In the cell, it has been suggested that FtsZ filaments form the arcs of the ring, and are aligned in the cell circumferential direction. Using polarized fluorescence microscopy in live *Escherichia coli* cells, we measure the structural organization of FtsZ filaments in the Z-ring. The data suggests a disordered organization: a substantial portion of FtsZ filaments is

aligned in the cell axis direction. FtsZ organization in the Z-ring also appears to depend on the bacterial species. Taken together, the unique arrangement of FtsZ suggests novel unexplored mechanisms in bacterial cell division.

Related to cytokinesis, bacterial cell morphology and growth are controlled by a combination of physical and chemical processes. In standard medium, *Escherichia coli* cells are rod-shaped, and maintain a constant diameter during exponential growth. We demonstrate that by applying compressive forces to growing rod-shaped *E. coli*, cells no longer retain their rod-like shapes but grow and divide with a flat pancake-like geometry. The deformation is reversible: deformed cells can recover back to rod-like shapes in several generations after compressive forces are removed. During compression, the cell elongation rate, proliferation rate, DNA replication rate, and protein synthesis are not significantly different from those of the normal rod-shaped cells. Quantifying the rate of cell wall growth under compression reveals that the cell wall growth rate depends on the local cell curvature. MreB not only influences the rate of cell wall growth, but also influences how the growth rate scales with cell geometry. The result is consistent with predictions of a mechanochemical model, and suggests an active mechanical role for MreB during cell wall growth. The developed compressive device is also useful for studying bacterial cells in unique geometries.

Dissertation Advisor: Dr. Sean X. Sun

Dissertation Readers:

ABSTRACT

Professor, Dr. Sean X. Sun, Mechanical Engineering

Professor, Dr. Konstantinos Konstantopoulos, Chemical and Biomolecular Engineering

Assistant Professor, Dr. Ishan Barman, Mechanical Engineering

Acknowledgments

The past six years of doctoral study at Johns Hopkins University will always be a unforgettable part of my life. During this time I grew from a college student educated in math/mechanics to a researcher who is aimed at answering fundamental biological questions. Along this journey, I feel grateful and fortunate that I could obtain help from many generous people. First I would like to thank my advisor Dr. Sean Sun. His keen and creative suggestions have inspired me to think about questions in different ways. His patient advice and guidance have helped me navigate the research field. Also I'm grateful to every member of our lab. They have continuously inspired me with their thoughtful and creative suggestions. These people include Dr. Osman Yogurtcu, Dr. Bo Li, Dr. Lan Ganhui, Dr. Hongyuan Jiang, Dr. Alfredo Celedon, Dr. Evgeny Stukalin, Dr. Jin Seob Kim, Dr. Sitikantha Roy, Dr. Yizeng Li, Dr. Sam Walcott, Nash Rochman, Sarita Koride, Flori Yellin, Jiaxiang Tao and Yoshitaka Sei.

I also would like to thank our collaborator Dr. Denis Wirtz, who generously provided most of the experimental facilities during my research. Without his support, it would not have been possible to accomplish any of my projects. Also I would like

ACKNOWLEDGMENTS

to express my gratitude to everyone in Dr. Wirtz's lab that have helped me on many occasions. These include Dr. Terrence Dobrowsky, Dr. Lijuan He, Dr. Saumendra Bajpai, Dr. Shyam Khatau, Dr. Meng Horng Lee, Dr. Pei-Hsun Wu, Dr. Christopher Hale, Dr. Brian Daniels, Dr. Stephanie Fraley, Dr. Dong-Hwee Kim, Dr. Yu-Tai Chang, Dr. Daniele Gikes, Dr. Zev Binder, Dr. Allision Chambliss, Dr. Anjil Giri, Dr. Wei-Chiang Chen, Jake Sarnecki, Jenna Graham, Jude Phillip, Hasini Jayatilaka, Ivie Aifuwa, Tania Perestrelo and Nicolas Perez.

I would like to thank our collaborator Dr. William Margolin and his lab member Dr. Kimberly Busiek, who generously provide us various strains necessary for all of our projects on bacteria.

I also would like to thank our collaborator Dr. Konstantinos Konstantopoulos, who has helped me on mammalian cell projects and serves on my dissertation committee. I am also grateful to his lab members Dr. Kimberly Stroka, Dr. Bryan Grabias, Bin Sheng Wong and Christopher Yankaskas.

I would like to thank Dr. Jeff Wang and Huy Vo who helped me with microfluidics and micro fabrication, as well as Dr. Wang's lab members Dr. Cyrus Beh, Dr. Tushar Rane and Helena Zec.

I am also grateful to Michael McCaffery and Erin Pryce at Johns Hopkins Integrated Imaging Center, who taught me how to use all of the microscopes.

I also would like to thank Dr. Jie Xiao and her lab member Dr. Xinxing Yang, who collaborated with me on projects of bacteria division.

ACKNOWLEDGMENTS

I thank Dr. Ishan Barman who serves as on my dissertation committee. I have benefited from his expertise in spectroscopy.

Last but not least, I will always be thankful to my parents. They have been continuously supporting me throughout this journey. I also thank all of my friends with whom I have shared many beautiful memories. I am truly grateful to all of the people mentioned above.

Contents

CONTENTS

List of Tables

List of Figures

Chapter 1

Introduction

Bacteria such as *Escherichia coli* are some of the simplest single cell organisms. All of the essential life functions of bacteria are accomplished by molecular machines (proteins) operating at the nanoscale. The molecular mechanisms typical involve many protein complexes working together, and can be understood using principles of mechanics and chemistry at the molecular scale. Some of these molecular systems such as the chemoreceptor array and the MinCDE system [1, 2] are well studied. The bacterial chemoreceptor arrays have been found to be hexagonally packed trimers of receptors dimers. The array can sense low levels of chemoattractants and transmit signals that ultimately control the rotation of the flagella. The MinCDE system regulates the location of the Z-ring by inhibiting the assembly of FtsZ outside of the midcell region. MinC inhibits polymerization of FtsZ *in vitro* and have been shown to oscillate from cell pole to cell pole *in vivo*. However, the mechanisms behind many

other essential processes such as cytokinesis, DNA segregation and maintenance of cell shape are not well established. The main difficulties can be ultimately traced to the resolution limit of light microscopy, which prevents observation of molecular processes occurring in individual bacterial cells. Here, we utilize novel fluorescence microscopy techniques to investigate the organization of the bacterial division ring (Z-ring), which is a key question in understanding the role of the Z-ring during cytokinesis. We also construct new microfluidic devices to manipulate single bacterial cells to reveal the molecular mechanisms behind cell shape control and growth.

1.1 Organization of FtsZ filaments in the bacterial division ring

FtsZ, a prokaryotic homologue of tubulin, is an essential protein in binary fission of prokaryotic cells [3]. *In vitro*, FtsZ forms short protofilaments and long bundles [4]. *In vivo*, along with membrane-binding FtsA and several other partners, FtsZ assembles into a ring-like structure (Z-ring) and facilitates cytokinesis [5,6]. Because cell division involves constriction of the rigid bacterial cell wall, it has been hypothesized that the Z-ring generates a mechanical force. Several force generation mechanisms have been proposed [7,8]. These mechanisms are inferred from the unique biophysical properties of FtsZ [9], and direct observations of constriction in a reconstituted FtsZ-lipid system [10]. Several high-resolution structural studies of the Z-ring have appeared: In

Caulobacter crescentus, cryo-electron tomography studies showed that FtsZ filaments are aligned in the circumferential direction of the cell [11]. Cryo-electron microscopy of vitreous sections of Enterococcus gallinarum is also available [12]. Recent super resolution microscopy studies [13–15] seem to suggest that higher order Z-ring structures may exist. Here, we focus on examining the orientation of FtsZ filaments in the *E. coli* Z-ring. In particular, while it is commonly suggested that FtsZ filaments are bundled and oriented in the circumferential direction of the cell, no direct *in vivo* evidence of this organization is available in it E. coli. Using polarized fluorescence microscopy, we quantitatively measure the orientation of FtsZ filaments in the Z-ring. Results seem to indicate that FtsZ filaments in the Z-ring are disorganized, with a large portion of filaments oriented in the cell axis direction in *E. coli*. This finding raises new questions about the division mechanism and the potential role of FtsZ.

1.2 Bacterial morphology and growth under mechanical compression

Bacteria exist in a wide variety of forms, ranging from spheres, rods, and helices to branched, tapered, and flat morphologies [3, 16]. While the genetic differences that result in different bacterial shapes are known, actual molecular mechanisms that connect genes with organismal morphology are less clear. It is thought that a combination of physical and biochemical mechanisms gives rise to the final cell

wall shape [16–21]. In the Gram-negative *E. coli*, a single peptidoglycan (PG) layer in the cell wall is responsible for the rod-like shape. The PG layer is a covalently bonded network of long, rigid glycan strands cross-linked by relatively short and flexible peptide bridges. It is a strong but elastic network that provides mechanical strength to counteract internal turgor pressure and prevent cell lysis [22–24]. With the cooperation of the actin homolog MreB, *E. coli* grows by inserting PG into multiple sites in the lateral cell wall [23]. MreB is essential for the rod-like cell shape since it directly or indirectly recruits and positions PG biosynthesis machinery. It has been shown that when MreB is depleted, cells rapidly stop elongating, increase their diameter and grow with spherical morphology [25–27]. Existing experiments and biophysical models have demonstrated that MreB also contributes to the stiffness of cell wall and may exert inward forces on the wall, retaining the rod-like shape and preventing surface wrinkling in growth due to turgor pressure [19, 28–32].

From a mechanochemical prospective, since the PG layer can be considered as a single macromolecule, it has been proposed that the growth dynamics of the cell wall can be understood in terms of a mechanochemical energy [33]. This model predicted that, when nutrient and other variables are held constant, the rate of wall growth is controlled by the change in the cell wall mechanochemical energy. This leads to an explanation of the steady cell radius, which is the stable radius at which the cell wall mechanochemical energy is a minimum. In practice, rod-like bacterial cells do not change their radius and only elongate. The elongate rate is controlled by many

factors, including DNA replication and protein synthesis. Therefore, it is difficult to observe the presence of the steady radius in laboratory settings. A different approach is to externally perturb the rod shaped cell and observe how the bacterial cell adapts to perturbations [32, 34–36]. For example, filamentous *E. coli* cells growing in a curved shape along microchamber walls retain their bent shape when removed from the constraint [34]. Another experiment found that *E. coli* cells can pass through micro channels that are narrower than the cell diameter, and the cell shape became irregular [35]. In both cases, cells recover their rod-like shape after sufficient growth outside the confinement. Thus, *E. coli* cell is able to plastically adapt its morphology instead of growing as a straight, cylindrical rod in confined spaces. In addition to geometrical confinement, external mechanical forces have a similar effect on cell shape. It has been shown that when *E. coli* cells are bent by a torque coming from fluid flow, cell grows more on the side under tension, leading to a curved shape that is maintained after the torque is removed [37, 38]. These experiments show that growth dynamics of the cell can be further examined in these alternative settings.

Chapter 2

Organization of FtsZ filaments in the bacterial division ring

In this chapter, we employ PFM to investigate FtsZ attached to a GFP or a yellow fluorescent protein (YFP) in live bacterial cells. We compare polarized fluorescence from live cells with purified proteins in vitro to infer organizational features of FtsZ filaments in the Z-ring. In our study, linearly polarized filters are placed in both excitation and emission light paths in a custom epi-fluorescence microscopy system to enhance the contrast of polarized fluorescence signal [39]. To quantify the degree of fluorophore alignment with a laboratory axis, we define a polarization anisotropy, $P = (I_{||} - I_{=})/(I_{||} + I_{=})$, where $I_{||}$ is the emitted fluorescence intensity when the polarizer is positioned parallel to the Y direction of the microscope stage, and $I_{=}$ is the intensity when the polarizer is in the X-direction (Fig. 2.1). Thus, changes in

P with respect to the angle between fluorophore dipole and light polarization vector will show the direction of alignment of GFP or YFP tagged FtsZ in the Z-ring. P also does not depend on the absolute emission intensity (see 2.1.2). We analyze P quantitatively, and obtain a probability distribution of FtsZ filament orientations in vitro and in vivo.

2.1 Polarized fluorescence microscopy

Polarized fluorescence microscopy (PFM) is a powerful tool for analyzing dynamic organization of proteins in live cells. Excited by linearly polarized light, a fluorophore will emit fluorescence with an intensity that is proportional to the square of the cosine of the angle between the fluorophore electric dipole vector and the polarization vector [40]. Thus, PFM can reveal the orientational organization of the fluorophore and any protein that is rigidly attached to the fluorophore [41,42]. For example, using green fluorescent protein (GFP) attached to septin in budding yeast, PFM revealed an organizational transition in septin filaments during yeast cell division [43].

2.1.1 Microscopy configuration

In preparation for fluorescence microscopy of purified proteins, 1.5μl of protein in buffer was dropped on a cleaned glass slide and covered with a cover-glass. For live cells. 20μl of diluted cell culture was dropped onto a cleaned glass slide, and

mixed with 20μl 3wt% low-melting agarose solution [44]. Then 4μl 0.5wt% Casamino acids solution was immediately mixed into the cell-agarose mixture [44] followed by placement of a cover-glass on top. Microscopy was performed soon after solidification of the agarose.

The fluorescence microscope used in this study was a 3-I Marianas Live Cell Imaging Workstation (Intelligent Imaging Innovations, Inc., Denver, CO) with a 1.45 numerical aperture α-Plan-Fluor 100X oil objective (Carl Zeiss Microscopy, LLC, Thornwood, NY). Linear glass polarized filters (Edmund Optics Inc., Barrington, NJ) were placed in both excitation and emission paths (Fig. 2.1), which insures that the excitation and emission polarizations were exactly parallel to each other either along the lab X-axis or Y-axis. All the samples were illuminated by 488nm xenon arc lamp light and the images were captured by a Cascade II 512B EMCCD camera (Roper Scientific, Sarasota, FL). For all polarized fluorescence microscopy measurements, Z-stacks were scanned with a step depth of 100nm and captured with exposure times of 500ms and interval times of 500ms.

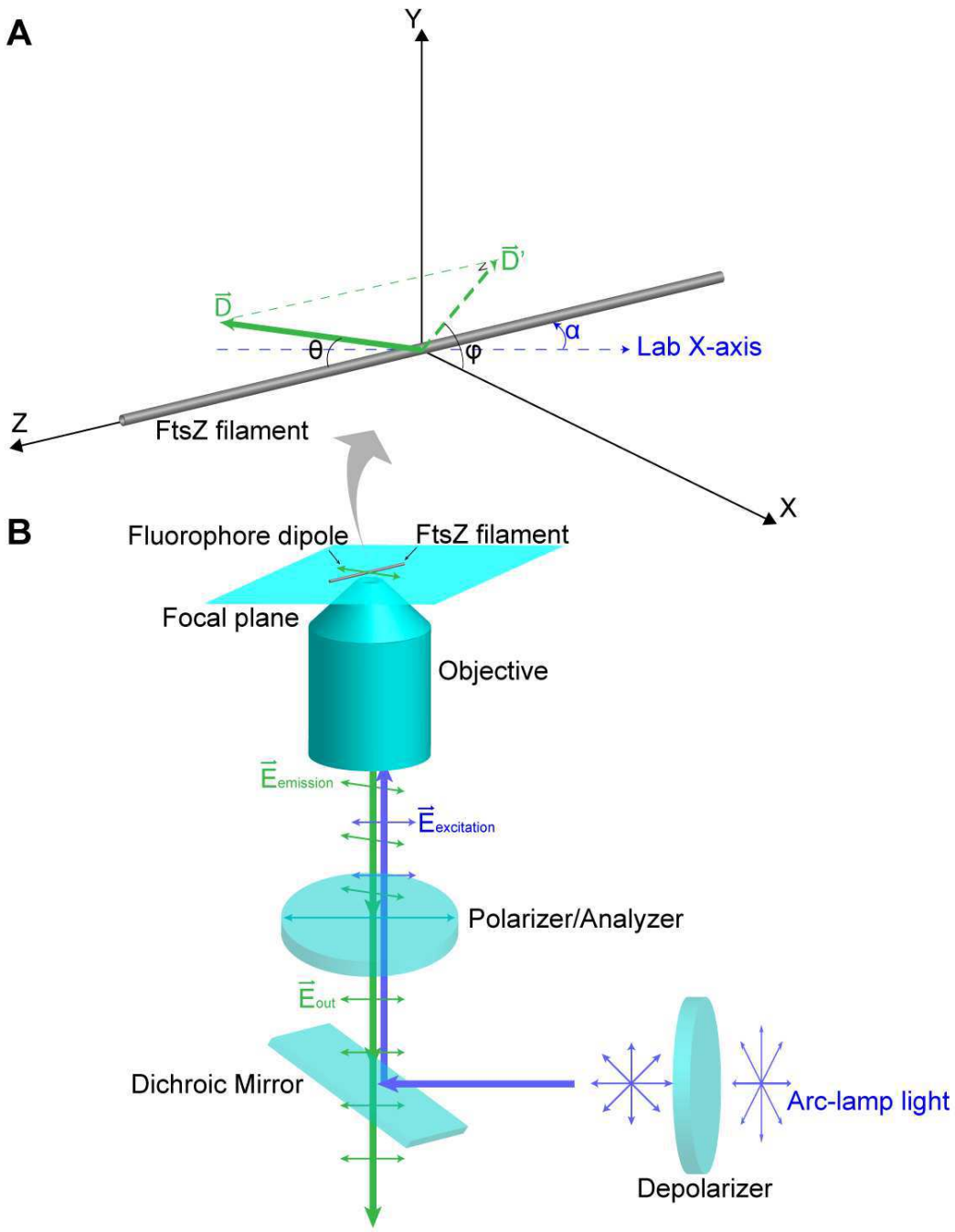

Figure 2.1: The microscopy setup showing the arrangement of the polarizers and the coordinate system describing the direction of the fluorophore attached to FtsZ filaments. (**A**) For protofilaments and bundles, we define the orientation of the fluorophore with respect to filament direction using angles θ and ϕ, where $\mathbf{D}$ is the fluorophore dipole vector and $\mathbf{D}'$ is its projection on the XY plane. (**B**) The microscopy setup using two polarizers. The sample is analyzed with respect to the polarization direction. The angle between the lab X-axis and the filament is defined by α. The polarization anisotropy is plotted as a function of the angle α. The same setup is used for *in vitro* and *in vivo* experiments.

2.1.2 Image processing

All image analysis and processing were performed using imageJ (NIH, Bethesda, MD) and Matlab (Mathworks, Inc., Natick, MA). In processing images of purified protein, protofilaments and bundles which are straight and lying horizontally on the cover-glass were selected. Two Z-stacks of images, one each for polarizer in X and Y directions, were recorded. These images correspond to intensity measurements $I_{||}$ and $I_{=}$. For each stack, 5 consecutive slices out of 20 where the protofilaments or bundles were well-focused were selected and averaged. The background noise was cut by first histogramming the intensity of all background pixels, and then removing pixels that had intensity below an intensity cutoff I_c. The cutoff is chosen at 1.5 standard deviations above the most probable background intensity, which corresponds to the most likely noise intensity. All of our results are insensitive to this cutoff value. Angles between protofilaments or bundles and the lab X-axis were carefully measured.

In processing images from the side view of cells, to insure all processed cells are lying horizontally, only cells that exhibited uniform fluorescence from pole to pole during Z-stack scan were selected. Again, two stacks of images for X-axis and Y-axis polarizer alignment were analyzed. For each stack, 2 consecutive slices out of 40 where the top of Z-ring are in focus were picked out and averaged. The background noise was cut in the same way as purified protein images. The angle between the Z-ring and the lab X-axis was carefully measured.

In processing images from the cross-sectioned view of cells, only the cells standing

vertically to the cover-glass which displayed circular cross-section were selected. For either X-axis or Y-axis polarizer alignment, 5 consecutive slices out of 40 where the cross-section of the Z-ring was in focus were picked out and averaged. The background noise was cut in the same way as above. Then the ring was divided into 18 angular slices corresponding to angle with respect to the lab Y-axis (Fig. 2.10). Intensity in each angular slice is recorded and analyzed.

Note that the final calculated polarization parameter P does not depend on the absolute emission intensity. However, most microscopes show some degree of polarization anisotropy. Nevertheless, this anisotropy should not be a function of the cell orientation or filament orientation. This anisotropy can be corrected by scaling the average emission intensities $I_{||}$ and $I_{=}$ so that they are equal. This also is equivalent to making $\int \mathrm{d}\alpha P(\alpha)$ by adding an overall constant to the $P(\alpha)$ curve. We have used this correction step to remove the microscope anisotropy.

2.2 Strains preparation

2.2.1 Strains and growth conditions

Strains for fluorescent detection of FtsZ *in vivo* all carried GFP or YFP fusions to FtsZ and were expressed as merodiploids, which replaced the native FtsZ. *E. coli* strains were as follows: WM3452 is XL1-Blue containing a plasmid (pDSW209-FtsZYFP338) expressing an isopropyl-beta-D-thiogalactopyranoside (IPTG)-inducible

FtsZ with an EYFP gene inserted at residue 338 of FtsZ, within the nonconserved linker domain. WM2026, used as a strain with FtsZ-GFP, expresses an IPTG-inducible chromosomal FtsZ-GFP fusion (GFP fused to the C terminus of FtsZ) at the lambda attachment site in WM1074 (TX3772). WM3486, derived from WM2026, is a strain with a deletion of MinCDE system. WM3498, carrying pDSW209-GFP-FtsZ in WM1074, is used as the strain with GFP fused to N terminus of FtsZ, whereas WM3497, carrying pDSW209 in WM1074, is used as a vector control as it expresses GFP only. The *C. crescentus* strain EG444 used here contains a xylose-inducible FtsZCc-EYFP integrated at the xylX chromosomal locus.

All *E. coli* strains were cultured on LB with 50μg/ml ampicillin. An overnight culture was diluted 1:40 into LB medium with 50μg/ml ampicillin, incubated with shaking until an OD600 of 0.3-0.4, and IPTG added to induce FtsZ-YFP, FtsZ-GFP, GFP-FtsZ or cytoplasmic GFP expression. Specifically, 50μM IPTG was used for WM3452 and 100μM for WM2026, WM3486, WM3498 and WM3497. *C. crescentus* strains were cultured on PYE (peptone yeast extract) with 25μg/ml kanamycin at 28°C [45]. Overnight cultures were diluted 1:40 into PYE with 25μg/ml kanamycin, incubated with shaking until an OD600 of 0.3-0.4, and 0.6 wt% xylose was added to induce FtsZCc-EYFP.

2.2.2 Protein purification and polymerization *in vitro*

To purify FtsZ and its fluorescently tagged derivatives, strains expressing each protein were grown from overnight cultures at a 1:100 dilution in 1.5-4.5 liters of Luria-Bertani (LB) broth supplemented with appropriate antibiotics (tetracycline, 5μg/ml; ampicillin, 100μg/ml). Cultures were grown at 37°C and induced during logarithmic phase using a final concentration of 1mM IPTG. Cells were collected after 2-5 hours by centrifugation at 10,000 X g. Pellets were resuspended using 40 ml lysis buffer (50mM Tris pH 8.0, 300mM NaCl, 10mM $MgCl_2$, 1mM EDTA) per liter of cells. Resuspended cells were incubated with lysozyme (4 mg/ml), phenylmethylsulfonyl fluoride (PMSF; 1mM), and beta-mercaptoethanol (0.1%) for one hour on ice. Cells were lysed using 10 cycles of sonication (50% duty cycle, output control 5, 30 seconds per cycle) and centrifuged at 10-12,000 X g. The resulting crude extract was brought to a final concentration of 35% $(NH_4)_2SO_4$, incubated on ice for 15 minutes, and centrifuged at 10,000 X g to reduce the amount of contaminating protein.

Following the ammonium sulfate cut, the pellet was homogenized in 25mM piperazine-N, N-bis[2-ethanesulfonicacid] (PIPES) pH 6.5 and centrifuged at 10,000 X g. The supernatant was brought to a final concentration of 1M sodium glutamate, 10mM $MgSO_4$, and 1mM guanosine triphosphate (GTP) and incubated at 37°C for 30 minutes to promote polymerization. Polymerized protein was pelleted by centrifugation

at 12,000 X g, resuspended in PIPES pH 7.4 buffer, and incubated on ice for 1 hour to depolymerize the protein. The resuspended pellet was centrifuged at 10,000 X g and the supernatant containing the depolymerized protein was stored at -80°C. The final concentration of each protein preparation was measured using the Bradford assay (native FtsZ, 3.2mg/ml; FtsZ1-338-YFP-FtsZ339-383 (referred throughout as FtsZ-YFP for simplicity), 0.3mg/mL; FtsZ-GFP, 0.1mg/ml; GFP-FtsZ, 1.4mg/ml). The final concentrations of each protein preparation was measured using the Bradford assay (native FtsZ, 3.2mg/ml; FtsZ-YFP, 0.3mg/ml; FtsZ-GFP, 0.1mg/ml; GFP-FtsZ, 1.4mg/ml; Caulobacter FtsZ-YFP 0.75-1mg/ml).

To polymerize bundles of FtsZ, wild-type FtsZ and FtsZ-YFP protein were diluted into 25mM PIPES with 1M sodium glutamate at pH 6.5 to final concentrations of 70 μg/ml and 200 μg/ml, respectively. Then, final concentrations of 1mM GTP and 10mM Magnesium sulfate were added. On the other hand, to polymerize single filaments of FtsZ, final concentrations of wild-type FtsZ and FtsZ-YFP were both 20μg/ml. Final concentration of 1mM GTP was added, and that of Magnesium sulfate was reduced to 4mM.

For polymerization of C-terminal FtsZ-GFP bundles, final concentrations of wild-type FtsZ and FtsZ-YFP were 70μg/ml and 120μg/ml, respectively. For polymerization of C-terminal FtsZ-GFP protofilaments, final concentrations of wild-type FtsZ and FtsZ-YFP were both 20μg/ml. For polymerization of N-terminal GFP-FtsZ protofilaments, final concentrations of wild-type FtsZ and FtsZ-YFP were both

50μg/ml. Concentrations of GTP and magnesium sulfate are the same as FtsZ-YFP. To polymerize Caulobacter FtsZ-YFP, Caulobacter FtsZ-YFP were diluted into 25mM PIPES at pH 6.5 to a final concentration of 300μg/ml. Final concentrations of 1mM GTP and 10mM Magnesium sulfate were added.

2.2.3 Plasmid Construction

E. coli strains used for protein purification were constructed as follows: to fuse GFP to the amino-terminus of FtsZ (GFP-FtsZ), a plasmid-encoded copy of *E. coli* FtsZ was subcloned 3 to the GFP gene in plasmid pDSW207 using SacI and HindIII restriction sites. In this plasmid vector, the GFP gene is encoded upstream of the multiple cloning site. The resulting ApR plasmid was transformed into *E. coli* XL1-Blue, yielding strain WM3775. A carboxy-terminal fusion of GFP to FtsZ (FtsZ-GFP) was made by amplifying FtsZ with a forward primer encoding a SacI restriction site and a reverse primer encoding both a PstI restriction site and a tetra-asparagine linker to promote flexibility between FtsZ and GFP. The insert was digested with SacI and PstI and ligated into plasmid pDSW208. The GFP gene is located downstream of the multiple cloning site in pDSW208, allowing carboxy-terminal fusions of the inserted gene to GFP. The resulting ApR pDSW208-FtsZ plasmid was transformed into XL1-Blue to create strain WM3776. To construct an FtsZ-YFP fusion that would produce an FtsZ protein with an internal YFP, the EYFP gene was PCR-amplified with primers 1201 (GTT CAG CAG CCA GTG ATG GAT CGC AGT AAA GGA GAA

GAA CTT TTC ACT) and 1202 (CGG AGC CAT CCC ATG CTG CTG GTA TTT GTA TAG TTC ATC CAT GCC ATG). The sequences corresponding to FtsZ are underlined. The amplified product was then used as a mega-primer for the Quikchange mutagenesis kit, using pDSW208-FtsZ (no fusion to GFP) as a template, inserting the EYFP between amino acid residues 338 and 339 of FtsZ to make FtsZ1-338-YFP-FtsZ339-383 (FtsZ-YFP). This corresponds to the linker region between the polymerization domain (1-320) and the C-terminal tail (370-383) of FtsZ. The FtsZ-YFP fusion was cloned into pDSW208 and transformed into XLI-Blue to make strain WM3308. Native FtsZ was overproduced from strain WM971, which carries FtsZ downstream of the T7 promoter of expression vector pET11a; this strain was a gift from Harold Erickson.

2.2.4 Cell Synchronization

C-terminal FtsZ-GFP *E. coli* strain was cultured in M9 media with 0.2% acetate. In this minimal nutrient media, the doubling time of *E. coli* cells is elongated to 3 hours; the DNA copy number is always between 1N-2N [46]. To synchronize the cell cycle, DL-serine hydroxamate (SigmaAldrich, S4503) was added to a final concentration of 1 mg/ml, which stops cell cycle at a new round of DNA replication. Ongoing rounds of replication still progress to completion [46]. Then, serine hydroxamate was washed out after all ongoing DNA replications are completed. Cells resumed the cell cycle in good synchrony. Polarization microscopy was done within the first cell

cycle after the synchronization, and data from two time points before and after the formation of visible septum were analyzed and compared.

2.2.5 Z-linker Constructs

In their polarized fluorescence microscopy experiments, Kampmann et al. [47] created a fusion of Saccharomyces cerevisiae protein Nic96 to GFP that was functional *in vivo* and yielded a high amplitude in anisotropy readings. This construct, Nic96-GFP(-8/-5), is composed of Nic96 protein that is truncated at its C-terminal alpha helix by 8 amino acid residues and GFP that is truncated at its N-terminal alpha helix by 5 amino acid residues. The fusion of the two truncated proteins yields a single, rigid alpha helix at the fusion site RETYST/ELF, where RETYST are residues 826-831 of Nic96 and ELF are residues 6-8 of GFP. To create a more rigid linker between FtsZ and GFP, the Nic96-GFP linker region (RETYSTELF) was inserted between FtsZ and the remainder of GFP (residues 9-238) forming FtsZ-Nic96$_{\mathrm{linker-trunc}}$GFP. To make this construct, we first amplifed FtsZ with a forward primer encoding a SacI site and the N-terminus of ftsZ (#1430) and a reverse primer encoding the C-terminus of FtsZ, the linker region RETYSTELF, and residues 9 and 10 of GFP (#1733). In a separate reaction, we amplified *gfp* using a forward primer that also encoded the C-terminus of FtsZ, the linker region RETYSTELF, and residues 9 and 10 of GFP (#1732) and a reverse primer encoding the C-terminus of GFP and a PstI site (#1736). We then used combinatorial PCR to combine both PCR products using primers #1430 and

#1736. The final PCR product was digested with SacI and PstI restriction enzymes and ligated into vectors pDSW208 and pDSW208-*flag*, which contains a flag sequence between EcoRI and SacI sites. pDSW208-ftsZ-nic96$_{\mathrm{linker-trunc}}$gfp and pDSW208-flag-ftsZ-nic96$_{\mathrm{linker-trunc}}$gfp were transformed into XL1-Blue cells yielding WM4363 and WM4364, respectively.

Similar to the approach used by Kampmann et al. [47], we truncated the C-terminal alpha helix of FtsZ by 4 amino acid residues and fused it directly to N-terminally truncated GFP to create $_{\mathrm{trunc}}$FtsZ-truncGFP. We made this construct by first amplifying truncated ftsZ (encoding residues 1-379) using a forward primer encoding a SacI site and the N-terminus of ftsZ (#1430) and a reverse primer encoding residues 374-379 of FtsZ and residues 6-11 of GFP (#1735). In a separate reaction, we amplified gfp (residues 6-238) using a forward primer encoding residues 374-379 of FtsZ and residues 6-11 of GFP (#1734) and a reverse primer encoding the C-terminus of GFP and a PstI site (#1736). We used combinatorial PCR to combine both PCR products using primers #1430 and #1736. The final PCR product was digested with SacI and PstI restriction enzymes and ligated into vectors pDSW208 and pDSW208-*flag*. pDSW208-$_{\mathrm{trunc}}$ftsZ-$_{\mathrm{trunc}}$gfp and pDSW208-flag-$_{\mathrm{trunc}}$ftsZ-$_{\mathrm{trunc}}$gfp were transformed into XL1-Blue cells yielding WM4365 and WM4366, respectively.

2.3 Mathematical modeling

2.3.1 Mathematical expression of polarized light

The experiment measures fluorescence emission intensities from FtsZ tagged with a flurophore as a function of the angle of the incident polarized light. When interacting with the fluorophore, only the projection of excitation light in the direction of the fluorophore dipole is absorbed, and then emitted. Therefore,

$$\mathbf{E}_{emission} \propto (\mathbf{E}_{excitation} \cdot \mathbf{D})\mathbf{D} \tag{2.1}$$

where $\mathbf{D}$ is the fluorophore dipole vector [48]. This is because the rotational correlation time of fluorophores such GFP and YFP is significantly longer than their fluorescence lifetime [40, 49]. Thus, the emission intensity is an accurate reporter of the orientation of the fluorophore with respect to the incoming polarized light. As shown in Fig. 2.1, after filtering by the polarizer, the excitation light has an orientation parallel to the focal plane. Thus, neglecting phases, the incoming excitation electric vector is

$$\mathbf{E}_{in} = \sqrt{I_{in}}\mathbf{p} \tag{2.2}$$

where I_{in} is the intensity of the excitation light, and $\mathbf{p}$ is a unit vector in the direction of the electric vector. After passage through the microscope objective, some depolarization occurs and the excitation light is no longer fully polarized in the $\mathbf{p}$ direction. Taking into account this depolarizing effect, the new excitation light will have com-

ponents in other directions perpendicular to $\mathbf{p}$. The degree of depolarization depends on the numerical aperature. The microscope objective we use has a numerical aperature NA=1.45. This depolarization phenomenon is well studied and the relationship between $\mathbf{E}_{in}$ and $\mathbf{E}_{excitation}$ is known [50, 51]. We include this depolarization effect in our data analysis for the incoming as well as the outgoing polarized light (see 2.3.2).

2.3.2 Calculation of depolarization from objective

After passage through the objective, some depolarization occurs and the excitation light is no longer fully polarized in the $\mathbf{p}$ direction. Taking into account this depolarizing effect, the excitation light after passing through the objective can be written as

$$\mathbf{E}_{in} = \sqrt{I_{in}}(I_p\mathbf{p} + I_q\mathbf{q} + I_r\mathbf{r}) \tag{2.3}$$

where $\mathbf{q}$ is a unit vector perpendicular to the polarization direction, $\mathbf{r}$ is a unit vector in the direction of propagation, and $I_{p,q,r}$ are the components of $\mathbf{E}_{excitation}$ in $(\mathbf{p}, \mathbf{q}, \mathbf{r})$ directions. In our experiment, $\mathbf{q}$ correspond to the Lab X -axis (shown in Fig. 2.1); $\mathbf{r}$ correspond to the Lab Y-axis and $\mathbf{p}$ is orthogonal to $(\mathbf{q}, \mathbf{r})$. The microscope objective we use has a numerical aperture of $NA = 1.45$. If we integrate over the electrical field in the focal plane, we have $I_p = 0.62$, $I_q = 0.08$ and $I_r = 0.30$ [50].

When interacting with the fluorophore *in vitro*, the incoming light is also the light exciting the fluorophore: $\mathbf{E}_{in} = \mathbf{E}_{excitation}$. Only the projection of excitation light on

the orientation of fluorophore dipole is absorbed, and then emitted

$$\mathbf{E}_{emission} \propto (\mathbf{E}_{excitation} \cdot \mathbf{D})\mathbf{D} \tag{2.4}$$

where $\mathbf{D}$ is the fluorophore dipole vector [48]. This is because the rotational correlation time of fluorophores such GFP and YFP is significantly longer than their fluorescence lifetime [40, 49]. Also for GFP and YFP used in this study, the fluorphores' absorption and emission transition dipoles are mostly parallel [49, 52]. The emitted light is then filtered by the analyzer, and the analyzed light is collected by the camera. Taking into account depolarization effects of the emission through a high numerical aperture objective, the emitted fluorescence intensity collected by the camera is

$$\begin{aligned} I_{out} &\propto (\mathbf{E}_{out})^2 \propto I_{in}\left[K_p(\mathbf{E}_{emission}\cdot\mathbf{p})^2 + K_q(\mathbf{E}_{emission}\cdot\mathbf{q})^2 + K_r(\mathbf{E}_{emission}\cdot\mathbf{r})^2\right] \\ &\equiv I_{in} f(\mathbf{p},\mathbf{q},\mathbf{r},\mathbf{D}) \end{aligned} \tag{2.5}$$

where $\mathbf{E}_{out}$ is the final electric vector reaching the camera, $K_{p,q,r}$ is the fraction of the component of $\mathbf{E}_{out}$ in the directions of $(\mathbf{p},\mathbf{q},\mathbf{r})$ [51]. Here, for an objective with $NA = 1.45$, we use $K_p = 0.377$, $K_q = 0.011$ and $K_r = 0.144$.

We also vary the polarizer direction with respect to the lab axis and compare the emission intensities when the polarization is parallel and perpendicular to $\mathbf{p}$-axis. Therefore, the excitation field in the parallel direction is

$$\mathbf{E}_{in,||} = \sqrt{I_{in}}(I_p\mathbf{p} + I_q\mathbf{q} + I_r\mathbf{r}) \tag{2.6}$$

$$\begin{aligned} I_{||} &\propto I_{in}\left[K_p(\mathbf{E}_{out,||}\cdot\mathbf{p})^2 + K_q(\mathbf{E}_{out,||}\cdot\mathbf{q})^2 + K_r(\mathbf{E}_{out,||}\cdot\mathbf{r})^2\right] \\ &\equiv I_{in} f_{||}(\mathbf{p},\mathbf{q},\mathbf{r},\mathbf{D}) \end{aligned} \tag{2.7}$$

and (note (I_p, I_q) have changed places)

$$\mathbf{E}_{in,=} = \sqrt{I_{in}}(I_q\mathbf{p} + I_p\mathbf{q} + I_r\mathbf{r}) \tag{2.8}$$

$$\begin{aligned} I_{=} &\propto I_{in}\left[K_q(\mathbf{E}_{out,=}\cdot\mathbf{p})^2 + K_p(\mathbf{E}_{out,=}\cdot\mathbf{q})^2 + K_r(\mathbf{E}_{out,=}\cdot\mathbf{r})^2\right] \\ &\equiv I_{in} f_{=}(\mathbf{p},\mathbf{q},\mathbf{r},\mathbf{D}) \end{aligned} \tag{2.9}$$

where the $||$ polarizer direction is along $\mathbf{p}$ and the $=$ polarizer direction is along $\mathbf{q}$.

2.3.3 Mathematical modeling of measured polarization

For small bundles of FtsZ *in vitro*, at the molecular-level, the fluorophore dipole is fluctuating rapidly on the time scale of the experiment. The probability distribution of the fluorophore dipole needs to be considered to quantitatively analyze the data. As shown in Fig. 2.1, we use two angles, θ and ϕ, to define $\mathbf{D}$. Therefore, the average collected fluorescence intensity is

$$\langle I_{||}\rangle \propto \langle I_{in} f_{||}(\mathbf{p},\mathbf{q},\mathbf{r},\mathbf{D})\rangle \propto I_{in}\int_0^{2\pi}\int_0^{\pi} f_{||}(\mathbf{p},\mathbf{q},\mathbf{r},\mathbf{D})\rho(\mathbf{D})\sin\theta d\theta d\phi \tag{2.10}$$

and similarly for $\langle I_{=}\rangle$. $f_{||}(\mathbf{p},\mathbf{q},\mathbf{r},\mathbf{D})$ is the function that descibes the interaction between dipoles and excitation light. The probability distribution $\rho(\mathbf{D})$ is the orien-

tational distribution of the dipole, which we take as

$$\rho(\mathbf{D}) = p(\phi)p(\theta) \tag{2.11}$$

where the distribution functions are angular Gaussians:

$$p(\phi) = p(\phi; a, \phi_0) = \frac{e^{a\cos(\phi-\phi_0)}}{\int_0^{2\pi} e^{a\cos(\phi-\phi_0)}d\phi} \tag{2.12}$$

$$p(\theta) = p(\theta; b, \theta_0) = \frac{e^{b\cos[2(\theta-\theta_0)]}}{\int_0^{\pi} e^{b\cos[2(\theta-\theta_0)]}\sin\theta d\theta} \tag{2.13}$$

Here a and b are parameters describing the widths of the angular distributions. ϕ_0 and θ_0 are the centers of the distributions, which represent the most probable orientation of the fluorophore. The denominators in these expressions are simply normalization factors.

For fluorophores attached to FtsZ *in vivo*, the direction of the fluorophore dipole in the lab coordinate system, $\mathbf{D}$, can be computed as

$$\mathbf{D} = \mathbf{R}\cdot\mathbf{u}(\theta,\phi) \tag{2.14}$$

where $\mathbf{u}$ is the direction of the fluorophore dipole in the local frame with respect to the filament and $\mathbf{R}$ is a rotation from the local frame of the filament to the local cell frame (Fig. 2.2). This rotation matrix is given in the 2.23. Given the filament angular distribution, the total measured fluorescence intensity is then

$$\langle I_{||}\rangle \propto I_{in}\int_0^{2\pi}\int_0^{\pi}\int_0^{2\pi}\int_0^{2\pi}\int_0^{\pi} f_{||}(\mathbf{p},\mathbf{q},\mathbf{r},\mathbf{D})\rho(\theta,\phi)\Gamma(\beta,\gamma,\psi)\sin\theta d\theta d\phi\sin\gamma d\psi d\beta d\gamma \tag{2.15}$$

where ρ is the fluorophore angular distribution with respect to the filament. ρ has been determined *in vitro* and we use the same distribution corresponding to each construct to compute the *in vivo* data. Γ is the filament orientation distribution, which is the objective of our measurement. The definitions of angles (β, γ, ψ) are given in Fig. 2.2. In the fluorescence measurement, cytoplasmic FtsZ, which has an isotropic angular distribution, will contribute to the final signal. Therefore, the filament angular distribution in Eq. 2.15 is a sum from the cytoplasmic component and the Z-ring component: $\Gamma = \Gamma_1 + \Gamma_2$. It was reported that 30-40% of FtsZ resides in the Z-ring [53]. From our own data, we find that 40% of the labeled FtsZ is in the Z-ring. Within the cropped Z-ring image, FtsZ in the Z-ring is 70% of the total signal and the cytoplasmic FtsZ accounts for 30%. Therefore, the cytoplasmic angular distribution should be $\Gamma_2 = 0.3/8\pi^2$. The Z-ring FtsZ distribution, Γ_1, is described by the filament angular distributions in the local cell frame as $\Gamma_1 = 0.7 \cdot p(\beta)p(\gamma)p(\psi)$, where the individual distribution functions are similar to Eq. 2.12 and 2.13,

$$p(\beta) = p(\beta; c, \beta_0) = \frac{e^{c\cos(\beta-\beta_0)}}{\int_0^{2\pi} e^{c\cos(\beta-\beta_0)} d\beta} \tag{2.16}$$

$$p(\gamma) = p(\gamma; d, \gamma_0) = \frac{e^{d\cos[2(\gamma-\gamma_0)]}}{\int_0^{\pi} e^{d\cos[2(\gamma-\gamma_0)]} \sin\gamma d\gamma} \tag{2.17}$$

and $p(\psi)$ is also similarly defined. (c, d) are again the width parameters of the distribution. From the measured polarization data, we again fit parameters $(c, d, \beta_0, \gamma_0)$ to obtain the average orientation as well as the distribution widths. Table 2.4.2 and 2.5.3 show the final best-fit parameters.

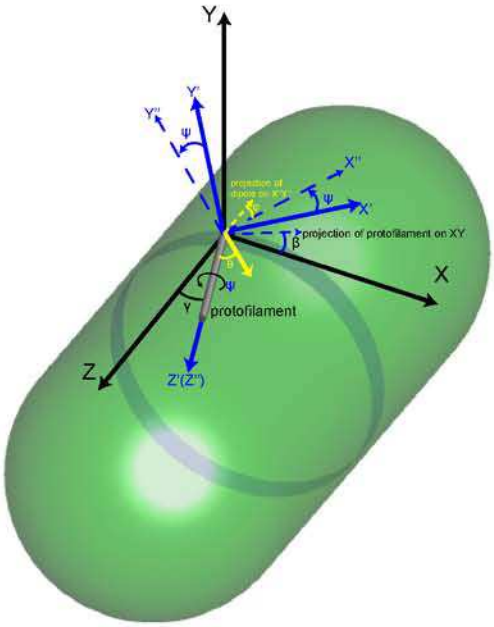

Figure 2.2: Coordinate system describing the orientation of the fluorophore dipole with respect to the protofilament in the local frame of the cell (X, Y, Z). In reality, filaments in the cell are not precisely aligned in the same direction. The protofilament orientation is described by an orientational distribution. The relationship between the fixed cell frame and the local frame of the fluctuating filament (X'', Y'', Z'') is given by the rotation matrix $\mathbf{R}$. The rotation procedure is given in the text.

2.4 Polarization anisotropy of FtsZ protofilament bundles *in vitro*

2.4.1 PFM Measurements of FtsZ protofilament bundles *in vitro*

We first calibrated and tested PFM using FtsZ protofilaments *in vitro*. FtsZ can polymerize into bundles or protofilaments, mainly depending on the concentration

of magnesium [4]. We polymerized FtsZ tagged with GFP (at C- or N-terminal ends) or YFP (at an internal linker near the C-terminal end) into protofilaments at a concentration of 1-2μM [54]. While most protofilaments were short ($\approx$100nm), a small percentage was of sufficient length (>300nm) to resolve the filament axis in the microscope. Electron microscopy images of these longer filaments showed that they are predominately small bundles, with 2 or 3 protofilaments in the bundles (Fig. 2.3). We collect data from these small protofilament bundles (also referred to as small bundles below), as well as large bundles with higher concentration of magnesium.

The measured fluorescence intensities noticeably changed as we rotated the polarizer (Fig. 2.3A). Fig. 2.3C plots the polarization anisotropy, P, as a function of the angle between FtsZ bundles and the lab X-axis. For *E. coli* FtsZ-YFP, FtsZ-GFP, GFP-FtsZ and *C. crescentus* FtsZ-YFP, P for large and small protofilament bundles reaches a peak at 90° and is lowest at 0°, although the amplitude of the peak for the small protofilament bundle is less than that of the large bundle (Fig. 2.3C). This result is direct evidence that when the filament is oriented parallel to the Y-axis ($\alpha = 90°$), $I_{||} > I_{=}$ and the polarization anisotropy reaches a maximum; when the filament is oriented parallel to the X-axis ($\alpha = 0°$ or 180°), $I_{=} > I_{||}$ and the polarization anisotropy reaches a minimum. This is possible only if the average direction of the GFP and YFP dipole is approximately parallel to the axis of FtsZ protofilaments or bundle. From this data, we also performed a quantitative analysis and extract angular distribution of GFP and YFP dipoles around the FtsZ filament

(see below).

2.4.2 Calculation of orientation distribution of fluorophore dipoles *in vitro*

To obtain a quantitative understanding of fluorophore orientation around the FtsZ filament, it is necessary to consider an angular distribution (described by a probability density) of fluorophores around the filament axis. The mathematical details are given in 2.3, and the basic idea is illustrated in Fig. 2.1. For a given filament in the illumination plane with spatial orientation described by angle α, we define a unit vector, $\mathbf{D}$, describing the direction of the fluorophore dipole. This vector is mathematically specified by angles (ϕ, θ). Since the fluorophore fluctuates rapidly, these angles are distributed probabilistically with average orientations (ϕ_0, θ_0) and standard deviations $(\sqrt{1/a}, \sqrt{1/b})$. We use angular Gaussian functions to describe the angular distributions. The observed fluorescence intensities are then computed by considering the projection of $\mathbf{D}$ in the direction of the incoming polarized light, and then integrating over all possible fluorophore dipole directions. Due to the high numerical aperature of the microscope, some depolarization of the incoming and outgoing light is present. These depolarization effects are taken into account in our calculation. The formula for the dipole distribution are given in the 2.3.

By collecting fluorescence data from randomly oriented FtsZ filaments, we can

calculate the polarization anisotropy as

$$P(\alpha) = \frac{\langle I_{||} \rangle - \langle I_{=} \rangle}{\langle I_{||} \rangle + \langle I_{=} \rangle} = P(\alpha; a, b, \phi_0, \theta_0) \tag{2.18}$$

where α is the angle of the filament with respect to the lab X-axis (Fig. 2.1). This function is experimentally measured. The signal is also a function of the dipole angular distribution with unknown parameters (ϕ_0, θ_0, a, b). Therefore by fitting the experimental curve, we can obtain information about the orientational probability distribution of the fluorophore with respect to the filament.

Using nonlinear optimization in Matlab, we have determined the parameters for a, b, ϕ_0 and θ_0 that best explain the experimental data. In Fig. 2.4, we see that for the *in vitro* FtsZ-YFP small protofilament bundles, we can only obtain a good fit to the experimental data when the average orientations are $\theta_0 = 0°$ and $\phi_0 = 0°$. Thus, the most probable orientation of the fluorophore is parallel to the protofilament. However, the distributions are quite broad (relatively small a and b values), the probability of observing other fluorophore orientations are quite high. These results suggest that the fluorophore has an angular distribution roughly equal to the distribution shown in Fig. 2.4 around the protofilament direction.

The fitted results for FtsZ-YFP bundles show generally the same θ_0 and ϕ_0 values, but with narrower distribution widths (Fig. 2.4B). This is reasonable since in a bundle, fluorophore fluctuations are presumably more constrained. PFM is able to measure this change in orientational distribution.

Results from GFP-FtsZ and FtsZ-GFP and *C. crescentus* FtsZ-YFP protofilament

bundles are also examined using this approach. We find that θ_0 and ϕ_0 are all similar, indicating that the fluorophore generally is aligned with the filament direction. All of the fitted results are summarized in Table 2.4.2. This alignment does not appear to depend on the position of fluorophore label, although the width of the distributions does show some variation. Since the linker between GFP and FtsZ is relatively disordered, this observed alignment is likely from non-specific interactions between GFP and FtsZ filament, possibly from surface electrostatic charges. FtsZ-filaments themselves may also have an electric dipole, which can further align the attached fluorophore.

In vitro orientation with respect to FtsZ	a (width of $p(\phi)$)	b (width of $p(\theta)$)	ϕ_0	θ_0
FtsZ-YFP	0.87	0.12	0°	0°
FtsZ-YFP Bundle	0.01	0.19	0°	0°
FtsZ-GFP	0.79	0.14	0°	0°
FtsZ-YFP Bundle	1.26	0.25	0°	0°
GFP-FtsZ	1.00	0.17	0°	0°
C. crescentus FtsZ-YFP	0.92	0.13	0°	0°

Table 2.1: Best fit parameters for angular distributions in Eq. 2.12 and 2.13, describing the orientation of the fluorophore with respect to the FtsZ filament *in vitro*.

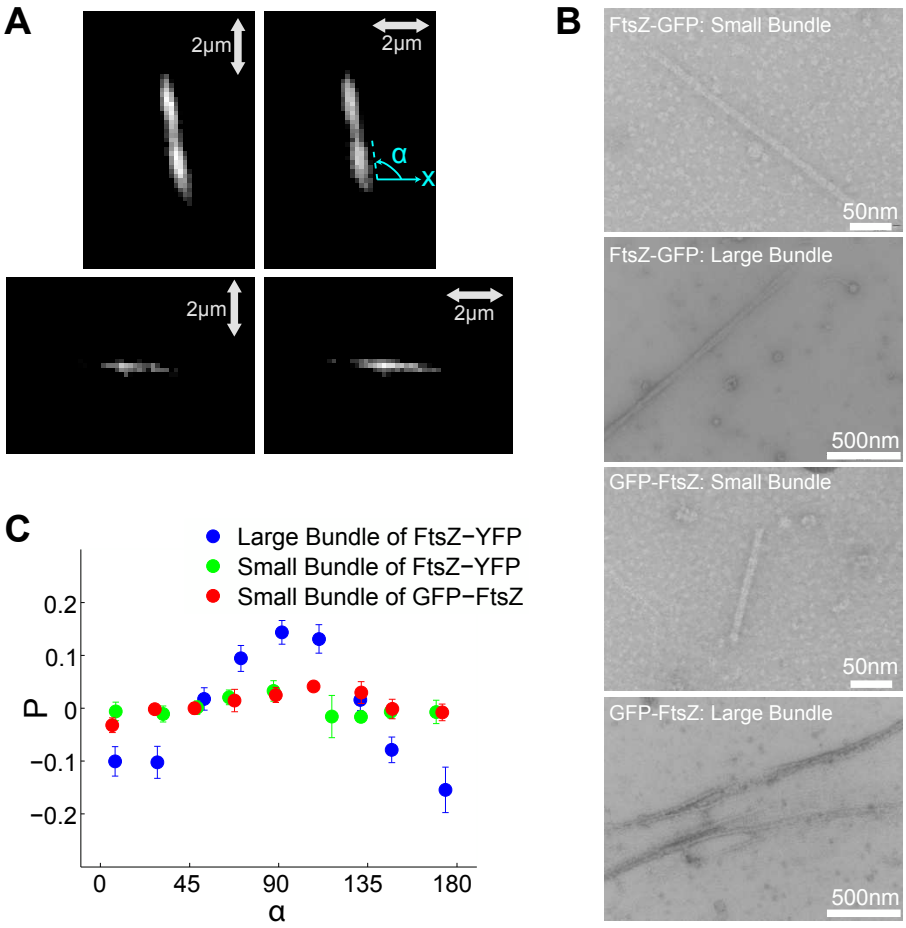

Figure 2.3: Polarized fluorescence measurement of purified FtsZ *in vitro*. (**A**) Polarized fluorescence images and (**B**) Electron microscopy (EM) images are shown for small and large FtsZ bundles. The EM images show parallel protofilaments of FtsZ bundled together. Fluorescence images are obtained when the linear polarizer is parallel and perpendicular to the X-axis. α is the angle between the bundle and the X-axis. (**C**) Largest polarization anisotropy, $P = (I_{||} - I_{=})/(I_{||} + I_{=})$, occurs when the angle between the bundle and the X-axis is 90°. Large bundles of FtsZ show a stronger anisotropy than small protofilament bundles. Error bars correspond to the standard error of the mean. C-terminal YFP large bundles (174 samples) and small bundles (92 samples), and N-terminal GFP small bundles (64 samples), all show a similar orientational alignment (see also Fig. 2.4). These results indicate that the fluorophore dipole is roughly parallel to the bundle.

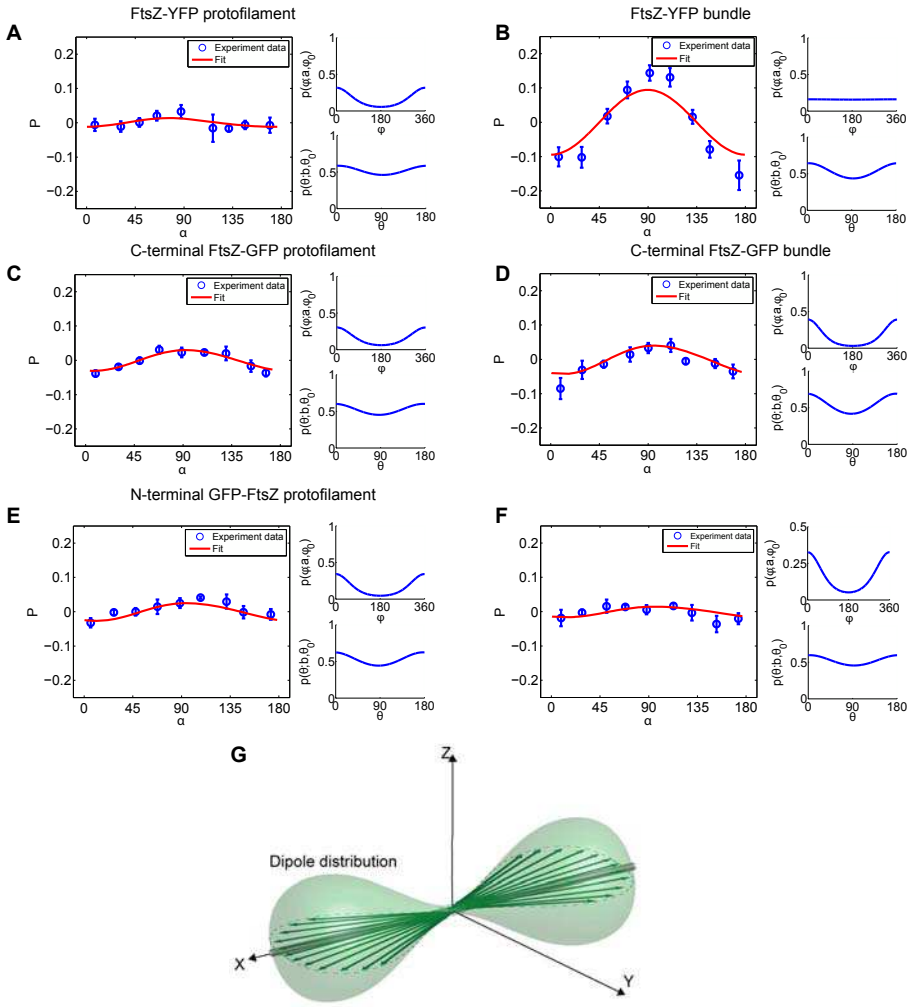

Figure 2.4: Calculation of orientational distribution of fluorophore dipole *in vitro*. The fitted fluorophore distributions for polarization data from (**A**) FtsZ-YFP protofilaments and (**B**) bundles, and (**C**) C-terminal FtsZ-GFP protofilaments, (**D**) C-terminal FtsZ-GFP bundles, (**E**) N-terminal GFP-FtsZ protofilaments, and (**F**) C-terminal FtsZ-YFP in *C. crescentus*. The best fit distributions for C-terminal FtsZ-YFP, FtsZ-GFP and N-terminal GFP-FtsZ protofilaments all show highest probability at $\theta_0 = \phi_0 = 0$, which is the orientation where the fluorophore dipole is parallel to the filament. (Note PFM is unable to decipher whether the dipole is parallel or antiparallel to the filament.) (**G**) A cartoon of the 3D orientational distribution of fluorophore dipoles around the FtsZ filament. There is some orientational disorder. The *average* dipole directions are along the filament.

2.5 Polarization anisotropy of FtsZ-ring in live cells

2.5.1 Optical anisotropy of bacterial cell body and correction of PFM data

To determine the alignment of FtsZ filaments in the Z-ring *in vivo*, we first imaged *E. coli* and *C. crescentus* cells expressing freely diffusing GFP or YFP in the cytoplasm to determine the possible existence of intrinsic polarization of the cell body. Many types of biological materials exhibit optical birefringence where transmitted or reflected light becomes polarized [39, 55]. As common for many biomaterials, we found that the bacterial cell itself is optically anisotropic. For instance, the peptidoglycan layer, the cell membrane or other protein structures in the cell could be birefriengent, which will influence the results of polarized microscopy. If this is the case, depolarized light emitted within the cell body can become partly polarized. To examine this, we performed polarized microscopy on *E. coli* that only expresses freely diffusing GFP in the cytoplasm (Fig. 2.5 and 2.6). The freely rotating GFP molecules should only emit completely depolarized fluorescence. In our measurement, we also use a relatively long exposure time so that rotational diffusion should give isotropic fluorescence.

Our measurements show that fluorescent signals from diffusing GFP still shows

some polarization anisotropy. The anisotropy is small (Fig. 2.6A). This result implies that the bacterial cell is optically anisotropic and converts the isotropic fluorescence emitted from freely diffusing GFP into partly polarized light. To quantitatively describe this intrinsic anisotropy, we can decompose the incoming and outgoing light into two components. One component is along the cell axis (Z in Fig. 2.2) and the other component is along the circumferential direction (X). We use a parameter C which is the ratio of the circumferential component to the axial component to describe the amount of optical anisotropy:

$$\mathbf{E}_{excitation} = \mathbf{B}(\alpha) \cdot \mathbf{E}_{in} \tag{2.19}$$

where $\mathbf{B}$ is a transmission matrix that depends on the angle of the cell with respect to the incoming light $\mathbf{E}_{in}$.

$$\mathbf{B} = \begin{pmatrix} C\cos\alpha & 0 & C\sin\alpha \\ 0 & 1 & \\ -\sin\alpha & 0 & \cos\alpha \end{pmatrix} \tag{2.20}$$

Similarly, the light received by the photo detector is also a similar function of the emitted light.

$$\mathbf{E}_{out} = \mathbf{B}(\alpha) \cdot \mathbf{E}_{emission} \tag{2.21}$$

The fit shows $C = 0.984$, which means the circumferential component is roughly 2 percents smaller than the axial part. Similar measurements for free YFP in *C. crescentus* also shows polarization anisotropy, with $C = 0.975$ (Fig. 2.7).

With the quantitative result from the freely diffusing GFP, we then use this intrinsic anisotropy to correct the data for all *E. coli* strains with GFP or YFP fused with FtsZ in the Z-ring (Fig. 2.6 and 2.7). Here we assume the cellular optical anisotropy effects are equal for all different strains because of the same cell wall structure. After the correction, all polarization anisotropy plots show smaller amplitudes, which means the Z-ring is less anisotropic if the cellular optical anisotropy is considered (Fig. 2.6). However, *C. crescentus* FtsZ-YFP data shows a different maximum after correction (Fig. 2.7).

2.5.2 PFM Measurements of FtsZ-ring in live cells

To analyze polarization signal from fluorophores attached to FtsZ in the Z-ring, we imaged *E. coli* cells from the side as well as at a cross section (Fig. 2.8, 2.9 and 2.10). In the side view, series of Z-stacks were scanned in order to determine variations in the fluorophore dipole orientation from the top to the middle of the Z-ring (Fig. 2.8A). Images were taken from several hundred cells with random orientations on the slide. Here, we plot P as a function of the angle between the Z-ring and lab X-axis. Interestingly, FtsZ-YFP and FtsZ-GFP strains both showed significant polarization anisotropy (Fig. 2.8C and D), even after correction for the intrinsic anisotropy of transmitted fluorescence. The polarization anisotropy now shows an opposite behavior as compared to purified protofilament bundles: it reaches a maximum at 0° and minimum at 90°. This anisotropy is also most pronounced for light coming from the

very top of the Z-ring (Fig. 2.8A, slice a). These results suggest that there is a significant portion of fluorophores that are aligned in the cell-axis direction.

In *E. coli*, FtsZ filaments are tethered to the inner membrane through a C-terminal link between FtsZ and FtsA [56]. Fluorophores attached to the C-terminal domain may adopt a different orientation than the *in vitro* situation due to interaction with FtsA. To check this, we also examined FtsZ with an N-terminal GFP *in vivo*. We found that just as in the *in vitro* purified protein situation, N-terminal GFP-FtsZ strain *in vivo* shows the same polarization anisotropy as the C-terminal FtsZ-YFP and FtsZ-GFP, suggesting that the relative orientation of the fluorophore and the filament axis is not perturbed *in vivo* (Fig. 2.8E). Thus, when the Z-ring is aligned with the X-axis ($\alpha = 0°$), $I_{||} > I_{=}$; when the Z-ring is perpendicular to the X-axis ($\alpha = 90°$), $I_{=} > I_{||}$. These results suggest that in *E. coli*, FtsZ filaments are not completely oriented in the circumferential ring direction. A substantial portion of the filaments is oriented in the cell-axis direction. In fact, this conclusion does not change if we consider a fluctuating fluorophore described by orientational distributions. The measured polarization anisotropy of *in vivo* data is also analyzed quantitatively (see 2.3).

Cell-axis alignment of FtsZ filaments can also explain polarization anisotropy measured from the cross sectional view (Fig. 2.10). Fluorescently labeled FtsZ-rings show polarization anisotropy as a function of the circumferential angle (Fig. 2.10C). Here, P shows two maxima at 90° and 270°. As the fluorophore fluctuates around the fila-

ment, there is a component of the fluorophore dipole in the direction of the polarized light, even when the filament is perpendicular to the plane of the cross-section. However, cross-sectional data cannot unambiguously distinguish circumferential and axial alignments.

In contrast, polarization anisotropy for FtsZ-YFP in *C. crescentus* shows a different behavior (Fig. 2.9A and B). After correcting for the intrinsic anisotropy, P reaches a maximum at 90° and minimum at 0°. While most papers in the literature simply assume circumferential alignment of FtsZ in bacteria, there have been studies that explicitly imaged FtsZ filaments *in vivo* [11, 12]. This study, performed using cryo-electron microscopy in *C. crescentus*, found that FtsZ filaments are aligned in the circumferential direction. Here, we find that PFM is indicating that the fluorophores are generally aligned circumferentially. Thus, our results are consistent with the interpretation that *C. crescentus* FtsZ filaments are aligned in the circumferential direction, but a substantial portion of filaments in *E. coli* are aligned in the cell-axis direction (Fig. 2.15).

2.5.3 Calculation of orientation distribution of FtsZ filaments in live cells

To quantify the degree of FtsZ alignment in the cell, we computed and compared the expected polarization anisotropy for FtsZ aligned in the circumferential and cell-

axis directions. 3D nature of the Z-ring, fluctuations of the attached fluorophore, and variations in FtsZ filament orientations are considered. Having examined the orientation of the fluorophores *in vitro*, it is then possible to obtain estimates of the filament orientation it in vivo. Since N- and C-terminal GFP and YFP tagged FtsZ all show similar polarization results both *in vitro* and *in vivo*, it is reasonable to conclude that in the live cell the fluorophore orientation on the FtsZ protofilaments are similar to the *in vitro* situation. Using the orientational distributions of fluorophores with respect to protofilaments *in vitro*, we can then infer the orientational distribution of FtsZ filaments *in vivo* by fitting the polarization data from the side view. As shown in (Fig. 2.2), we use two spatial angles β and γ to describe filament orientations in the local frame of the cell. The direction of the fluorophore dipole in the local frame of the cell, $\mathbf{D}$, can be computed as (Fig. 2.11A)

$$\mathbf{D} = \mathbf{R} \cdot \mathbf{u}(\theta, \phi) \tag{2.22}$$

where $\mathbf{u}$ is the direction of the fluorophore dipole in the local frame with respect to the filament and $\mathbf{R}$ is a rotation from the filament frame to the local cell frame (Fig. 2.2). Since the orientation of the fluorophore is defined by angles θ and ϕ in the frame (X'', Y'', Z''), we first find (X', Y', Z') by rotating along the Y-axis by γ and then along the Z-axis by β. To go from (X', Y', Z') to (X'', Y'', Z''), we then rotate along Z' by angle ψ. Thus, the overall rotation from the lab frame (X, Y, Z)

to (X'', Y'', Z'') is specified by three angles (β, γ, ψ). The rotation matrix is

$$\mathbf{R} = \begin{pmatrix} \cos\beta\cos\gamma\cos\psi - \sin\beta\sin\psi & -\cos\beta\cos\gamma\sin\psi - \sin\beta\cos\psi & \cos\beta\sin\gamma \\ \sin\beta\cos\gamma\cos\psi + \cos\beta\sin\gamma & -\sin\beta\cos\gamma\sin\psi + \cos\beta\cos\gamma & \sin\beta\sin\gamma \\ -\sin\gamma\cos\psi & \sin\gamma\sin\psi & \cos\gamma \end{pmatrix} \tag{2.23}$$

Note ψ has no direct bearing on the direction of the filament, it simply defines the fluorophore position with respect to the filament.

Since there are many filaments that can potentially orient in any direction, therefore as before, the overall FtsZ organization can be described by orientational distribution functions $P(\beta)$ and $P(\gamma)$ given explicitly in Eq. 2.16 and 2.17. These distributions are again characterized by average orientations and widths. In the live cell fluorescence measurement, cytoplasmic FtsZ, which has an isotropic angular distribution, will contribute to the final signal. Therefore, the fluorophore angular distribution is a sum from the cytoplasmic component and the Z-ring component: $\Gamma = \Gamma_1 + \Gamma_2$. It was reported that 30-40% of FtsZ resides in the Z-ring [53, 57]. From our own data, we find that 40% of the labeled FtsZ is in the Z-ring. Within the cropped Z-ring image, FtsZ in the Z-ring is 70% of the total signal and the cytoplasmic FtsZ accounts for 30%. Therefore, the cytoplasmic angular distribution should be $\Gamma_2 = 0.3/8\pi^2$. The Z-ring FtsZ distribution, Γ_2, is described by the filament angular

distributions in the local cell frame as $\Gamma_2 = 0.7 \times p(\beta)p(\gamma)p(\psi)$, where

$$p(\beta) = p(\beta; c, \beta_0) = \frac{e^{c\cos(\beta-\beta_0)}}{\int_0^{2\pi} e^{c\cos(\beta-\beta_0)} d\beta} \tag{2.24}$$

$$p(\gamma) = p(\gamma; d, \gamma_0) = \frac{e^{d\cos[2(\gamma-\gamma_0)]}}{\int_0^{\pi} e^{d\cos[2(\gamma-\gamma_0)]} \sin\gamma d\gamma} \tag{2.25}$$

$p(\psi)$ is also similarly defined. Given the filament angular distribution, the total measured fluorescence intensity is then

$$\langle I_{||} \rangle \propto I_{in} \int_0^{2\pi} \int_0^{\pi} \int_0^{2\pi} \int_0^{2\pi} \int_0^{\pi} f_{||}(\mathbf{p}, \mathbf{q}, \mathbf{r}, \mathbf{D}) \rho(\theta, \phi) \Gamma(\beta, \gamma, \psi) \sin\theta d\theta d\phi \sin\gamma d\psi d\beta d\gamma \tag{2.26}$$

where ρ is the fluorophore distribution with respect to the filament. ρ has been determined *in vitro* and we use the same distribution to compute the *in vivo* data.

To examine the *in vivo* data, we checked two preferred (average) orientations of the filament (Fig. 2.11), one oriented in the axial direction (Fig. 2.11B) and one oriented in the circumferential direction (Fig. 2.11C). We fixed β_0 and γ_0 in those orientations and fitted the widths c and d. We used the data from the very top slice to avoid any geometrical effects. The results and fitted distributions are shown in Fig. 2.11 for FtsZ-YFP. We see that both types of fits give similar results (Fig. 2.11). Both axial and circumferential filament orientations show significant angular scatter, suggesting that the filaments are disorganized. In Fig. 2.11, we also show the computer generated filament organization derived from the fitted distributions. Both axial and circumferential average orientation give a similar disorganized picture, with significant portions of filaments in the axial and circumferential directions. In

addition, we can also check intermediate average orientations (in between axial and circumferential for β_0 and γ_0), and the results are essentially the same as shown. If we define axially aligned filaments as those whose angles with the cell axis that are smaller than 45 degrees, we can calculate the percentage of these filaments from our orientation distributions. We obtain that 52% of FtsZ-YFP, 34% of FtsZ-GFP, 42% of GFP-FtsZ are axially aligned. Therefore, quantitative analysis suggests an overall disorganized picture for FtsZ in the ring.

Similar results were obtained for C-terminal FtsZ-GFP (Fig. 2.12) and N-terminal GFP-FtsZ (Fig. 2.13). Indeed, it is possible to fit this data with other average orientations. But the fitted distributions all are very broad, showing significant disorganized arrangement. In Fig. 2.11, 2.12 and 2.13, we show representative FtsZ filament arrangements in the Z-ring based on the fitted distributions, the results from these strains are consistent with each other. The fitted distributions are quantitatively in agreement with those obtained from the FtsZ-YFP data. The pictorial representation of filament orientations are also consistent.

2.5.4 Axial versus circumferential alignment in *Caulobacter crescentus*

To check whether the polarized fluorescence measurements agree with previous cryo-electron microscopy results for *Caulobacter crescentus*, we imaged C-terminal

In vivo FtsZ orientation	c (width of $p(\beta)$)	d (width of $p(\gamma)$)	β_0	γ_0
E. coli FtsZ-YFP axial	4.98	1.10	0°	0°
E. coli FtsZ-YFP circumferential	5.00	0.00	0°	0°
E. coli FtsZ-GFP axial	5.00	0.11	0°	0°
E. coli FtsZ-GFP circumferential	5.00	0.06	0°	0°
E. coli GFP-FtsZ axial	5.00	0.28	0°	0°
E. coli GFP-FtsZ circumferential	5.00	0.00	0°	0°
C. crescentus FtsZ-YFP axial	5.00	0.00	0°	0°
C. crescentus FtsZ-YFP circumferential	0.00	4.93	0°	0°

Table 2.2: Best fit parameters for angular distributions in Eq. 2.16 and 2.17, describing the orientation of the FtsZ filaments in the Z-ring with respect to the cell axial and circumferential directions. We use two different average orientations: axial and circumferential. The fitted parameters indicate broad angular distributions and are consistent with each other. The pictorial representations of these distributions are shown in Fig. 2.11, 2.12, 2.13, 2.14, 2.15

$FtsZ_{Cc}$-YFP of *C. crescentus* (courtesy of L. Shapiro Lab) from the side using the same setup and imaging procedures. After correction for the intrinsic polarization of the cell body, the curve shows a pronounced maximum at $\alpha = 90°$ (Fig. 2.14). Using the same fitting procedure, we find that only the circumferential organization can explain this data (Fig. 2.14B). This is consistent with the cryo-EM results of Ref. [11]. Thus, our measurement appears to reproduce prior results from a different technique. Quantitative fits reveals that the filaments are narrowly distributed in the

circumferential direction; 0% of the filaments are aligned within 45 degrees of the axial direction. These results are consistent with earlier EM findings.

Fig. 2.15 depicts the organization of the Z-ring as inferred from the quantitative analysis. The orientations of the filaments are directly selected from the fitted orientational distributions. Quantitative results from the fitted orientational distributions are given in Table 2.5.3.

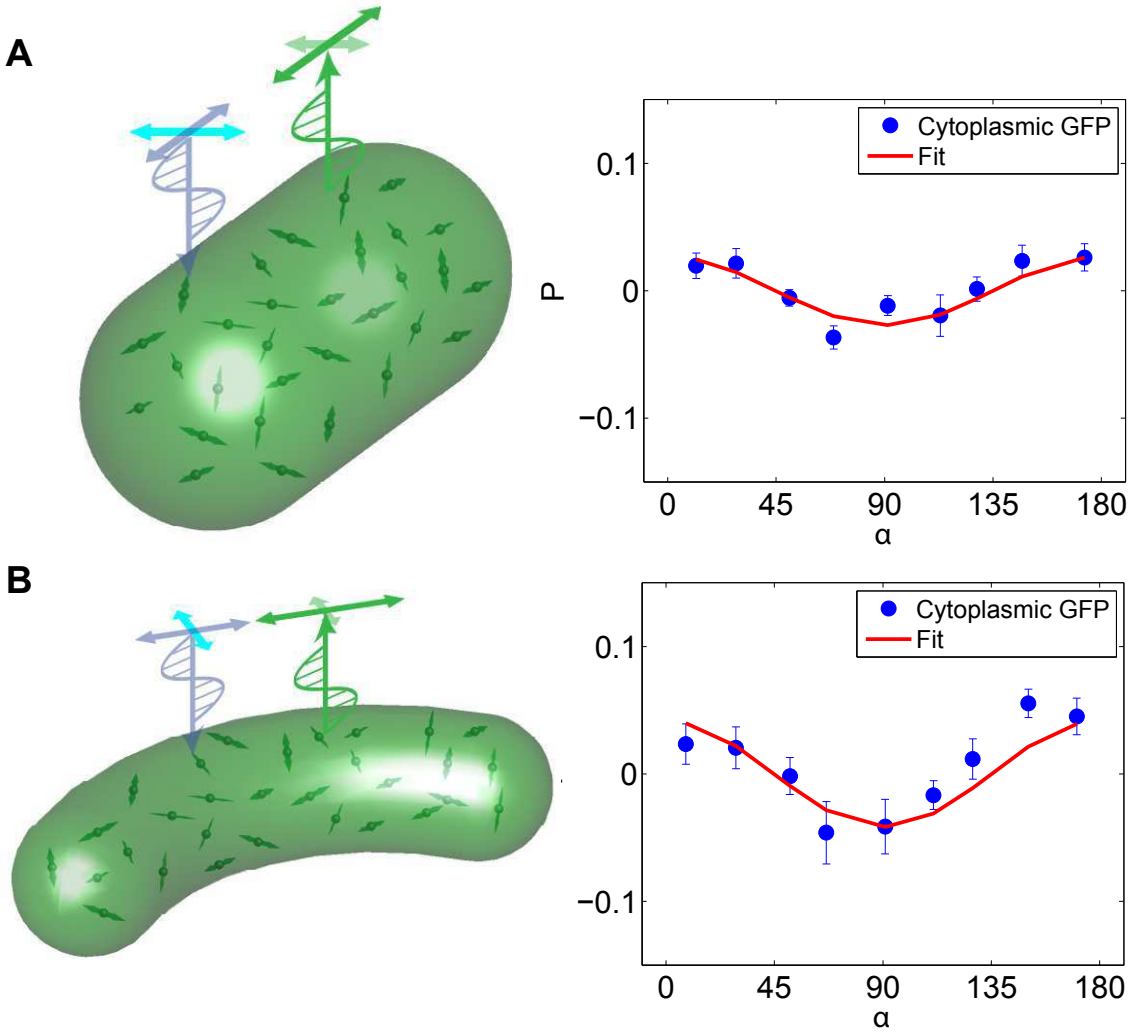

Figure 2.5: PFM of freely diffusing GFP in bacterial cells. (**A**) *E. coli* cells expressing free GFP are imaged from the side-view (213 cells included). As the angle between the cell-axis and the lab axis, α, changes, the images show an intrinsic polarization anisotropy. The reason for this unclear; it is likely the result of birefringence of biomaterials such as the peptidoglycan cell wall. The results can be used to derive an anisotropy factor, C, which can be used to correct the intensity from fluorophores attached to FtsZ. (**B**) *C. crescentus* cells with freely diffusing YFP show a similar intrinsic anisotropy (133 cells included).

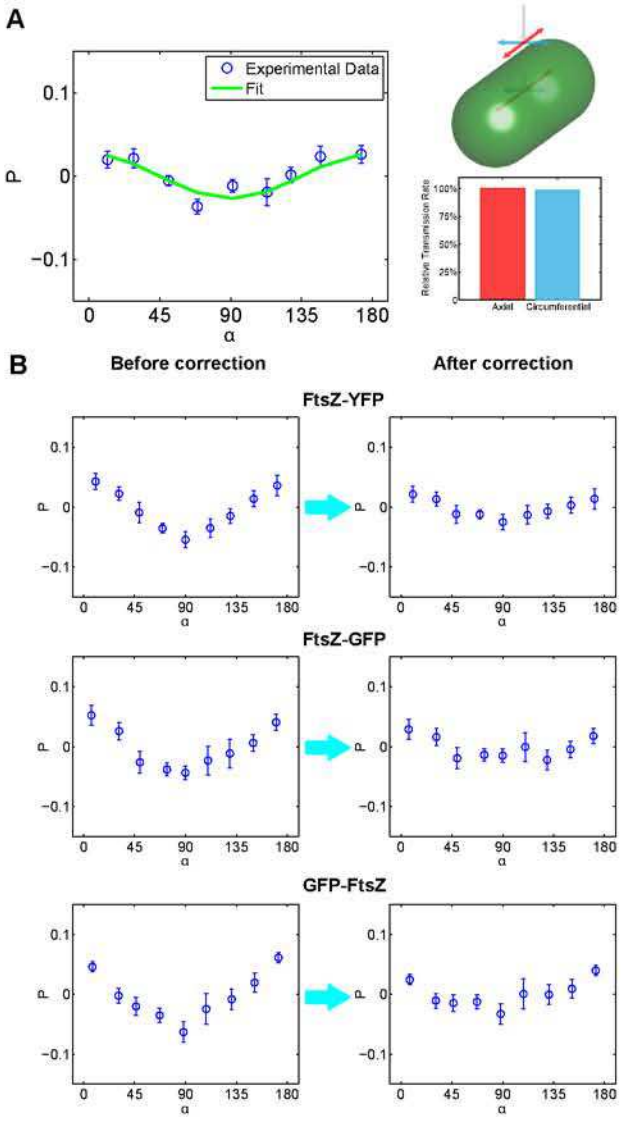

Figure 2.6: (**A**) Intrinsic polarization anisotropy in bacterial cells with freely diffusing GFP in *E. coli*. The angle α is the angle of the cell axis with respect to the lab X-axis. The intrinsic anisotropy could arise from birefringence of biomaterials such as the cell wall. (**B**) We can use the free GFP data as a calibration reference to correct anisotropy results from fluorophores attached to FtsZ. The correction accounts for anisotropic transmission of excitation and emitted light.

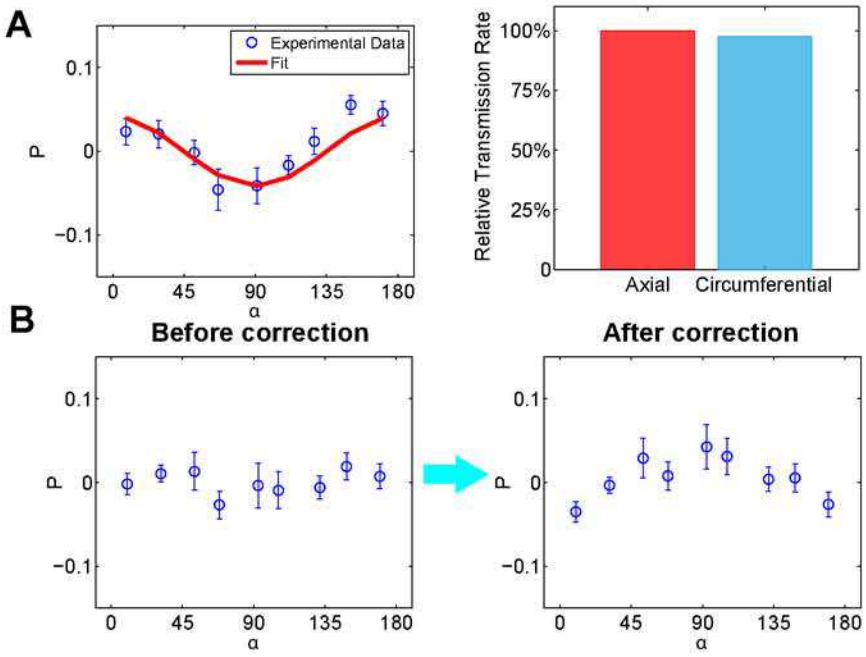

Figure 2.7: (**A**) Intrinsic polarization anisotropy in bacterial cells with freely diffusing YFP in *C. crescentus*. The intrinsic anisotropy could arise from birefringence of biomaterials such as the cell wall. (**B**) We can use the free YFP data as a calibration reference to correct anisotropy results from FtsZ-YFP.

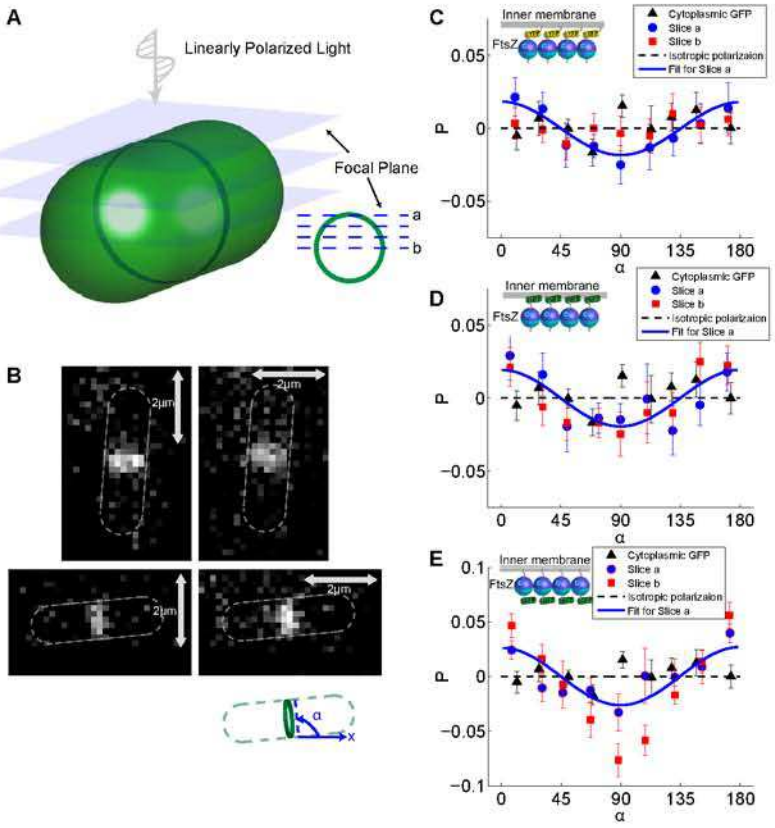

Figure 2.8: PFM of FtsZ filaments *in vivo* in *E. coli*. (**A**) Fluorescence images are collected from a side view (cells laying flat). To obtain 3D information, emitted fluorescence intensities are collected at different planes across the Z-ring. (**B**) Fluorescence images obtained at the top of the ring (plane a) for polarizer in the vertical and horizontal directions. α is the angle between the Z-ring and the X-axis. (**C**,**D**,**E**) Corrected polarization anisotropy as a function of α for it E. coli cells with different FtsZ fluorophore labels. Here, blue and green halves of FtsZ are the C- and N-terminal ends, respectively. 284 FtsZ-YFP (**C**), 206 FtsZ-GFP (**D**) and 56 GFP-FtsZ (**E**) cells are measured. Error bars correspond to the standard error of the mean. Fluorescence collected at two imaging planes, a and b, both show similar degree of anisotropy. As a negative control, corrected polarization anisotropy from cells expressing free GFP is also shown. Blue line is a quantitative fit to the data using a distribution of filament orientations, which indicates a disordered organization of FtsZ filaments.

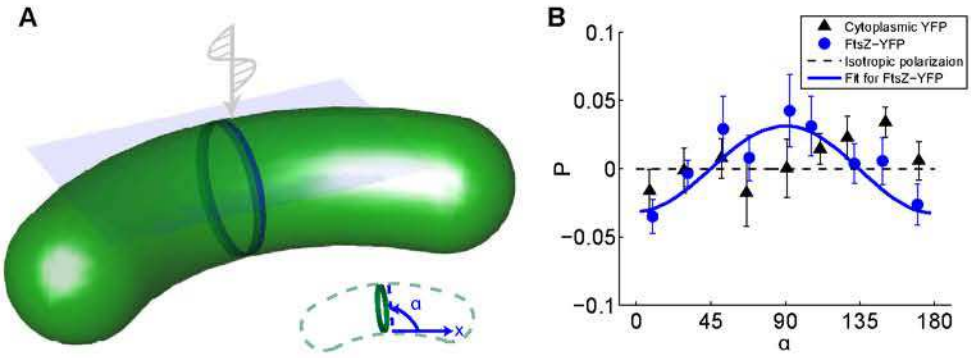

Figure 2.9: PFM of FtsZ filaments *in vivo* in *C. crescentus*. (**A** and **B**) Corrected polarization anisotropy as a function of α for *C. crescentus* cells expressing FtsZ-YFP. 87 cells are included. Blue line is a quantitative fit to the data, which indicates a circumferential alignment of FtsZ filaments.

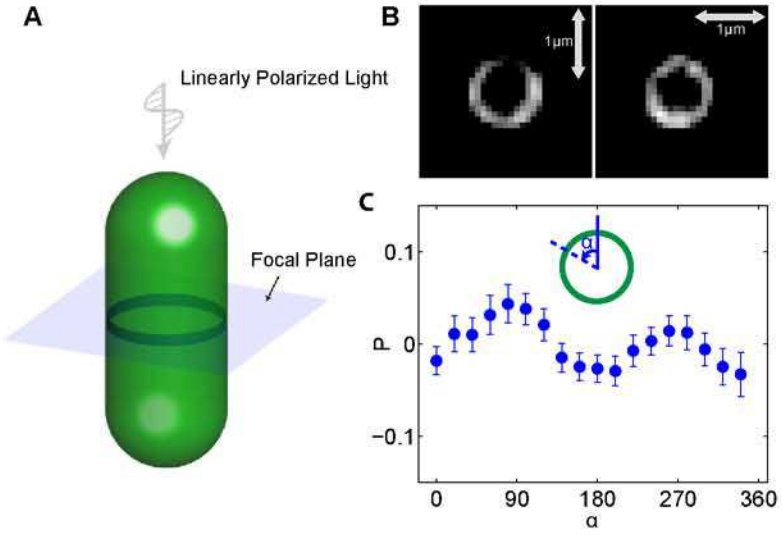

Figure 2.10: PFM of FtsZ from a cross-sectional view. (**A**) Cells with FtsZ-YFP are made to stand vertically with respect to the microscope stage. The emitted light is collected from the Z-ring. (**B**) Images obtained when the polarizer is oriented in the X and Y-axes directions. 38 cells are used to obtain the plot. Arrows denote scale bars of $1\mu m$. (**C**) The polarization anisotropy as a function of the angle around the ring in the X-Y plane. Error bars correspond to the standard error of the mean.

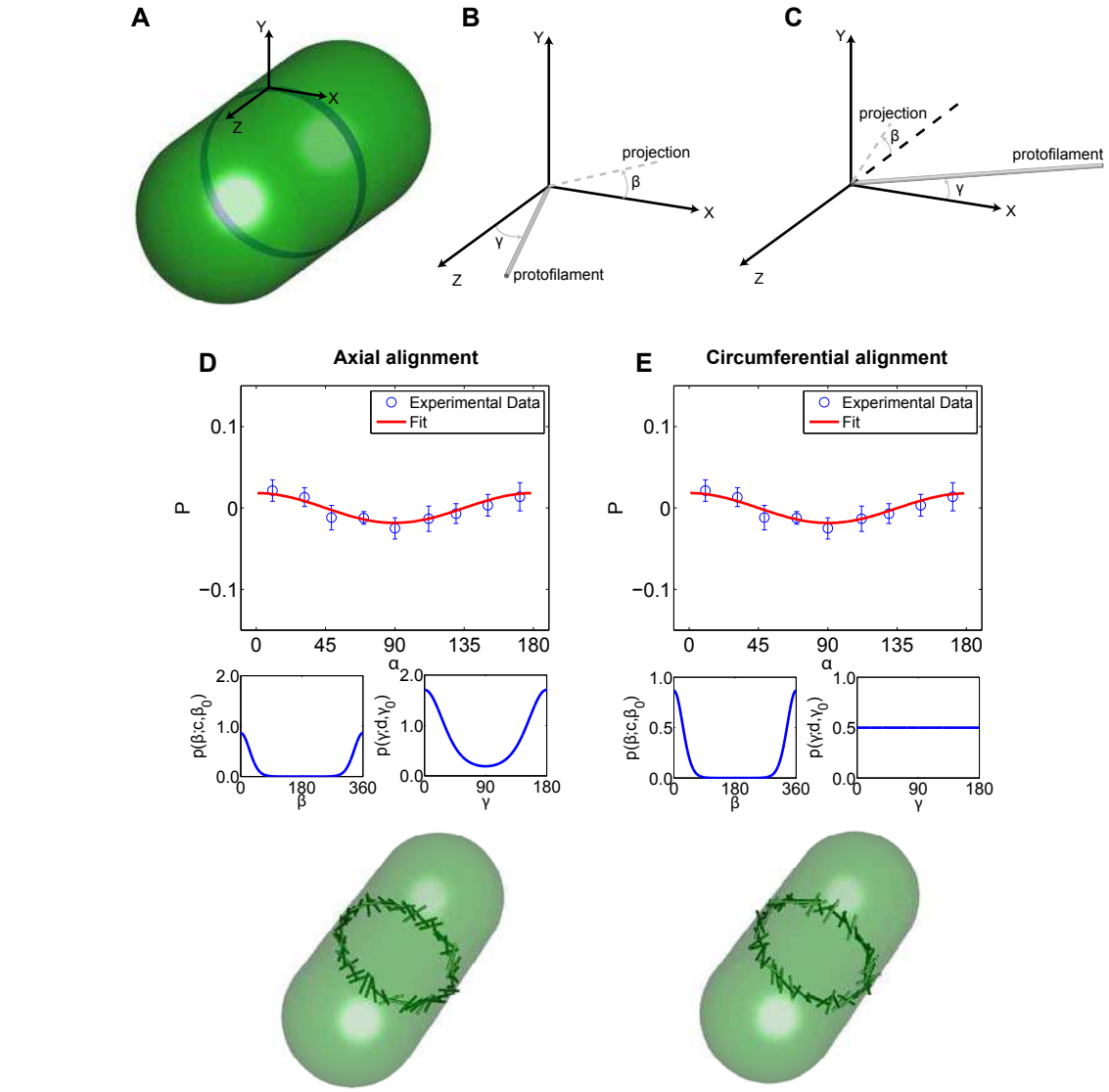

Figure 2.11: Analysis of the polarization anisotropy data from the side view for FtsZ-YFP in *E. coli*. (**A**) From images collected at the top of the Z-ring (slice a in Fig. 2.8), the lab coordinate frame is defined with z-axis in the cell axis direction. ((**B**) and (**C**)) Two average orientations of the FtsZ filaments are used to fit the data, the axial direction (B), and the circumferential direction (**C**). The filament orientations are defined by angles of γ and β. (**D**) Angular distribution fitted from the axial average orientation. We used the fitted distribution to generate the sample Z-ring organization which shows both axial and circumferential alignment. (**E**) The fitted distribution using the circumferential average orientation. The fitted distribution for γ is essentially uniform, consistent with (**D**). The generated Z-ring from this distribution is also essentially the same as in **D**, suggesting a disorganized orientation for FtsZ in the Z-ring.

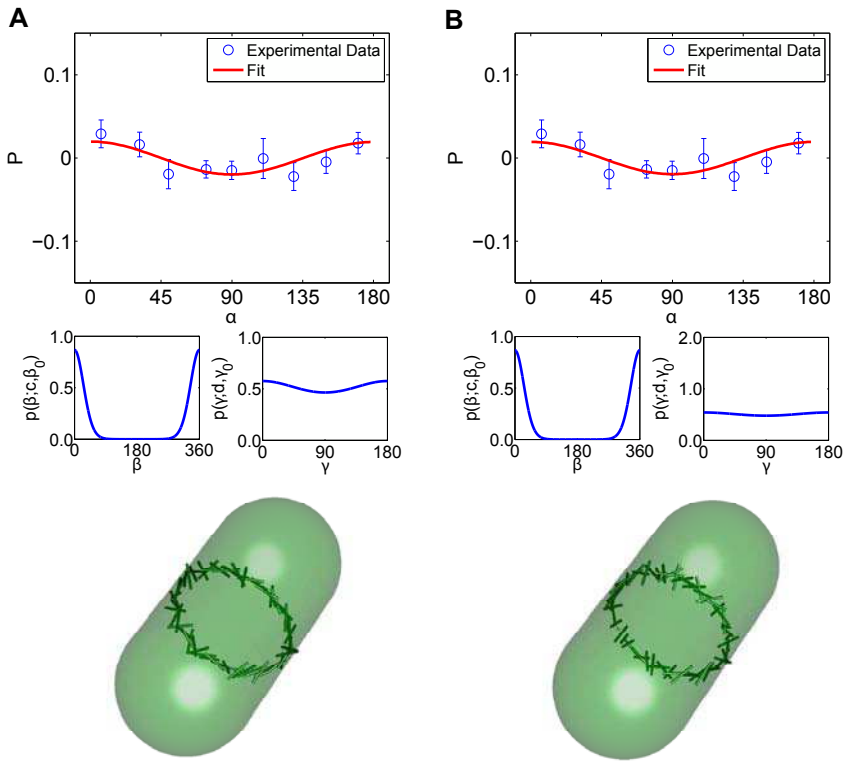

Figure 2.12: Analysis of the polarization anisotropy data from the side view for C-terminal FtsZ-GFP in *E. coli*. The results are similar to FtsZ-YFP. (**A**) is the fit using an average axial orientation (see Fig. 2.11). (**B**) is the fit using a circumferential average orientation. Once again, The distribution for γ is quite wide to almost uniform. The results suggest a disorganized Z-ring.

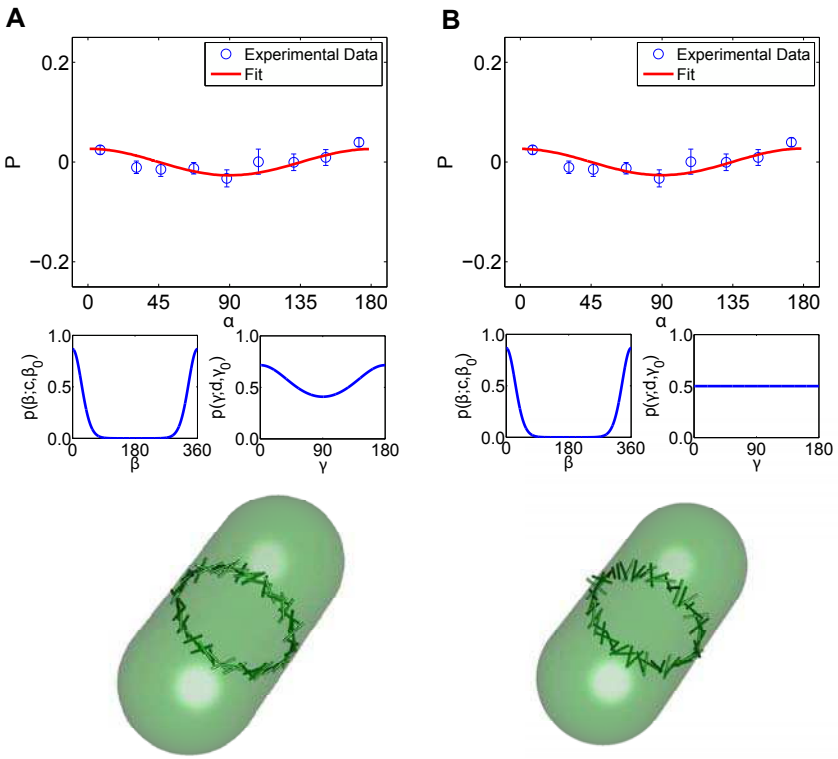

Figure 2.13: Analysis of the polarization anisotropy data from the side view for N-terminal GFP-FtsZ in *E. Coli*. (**A**) is the fit using an average axial orientation (Fig. 2.11). (**B**) is the fit using a circumferential average orientation. The results are consistent with those obtained from FtsZ-YFP and FtsZ-GFP.

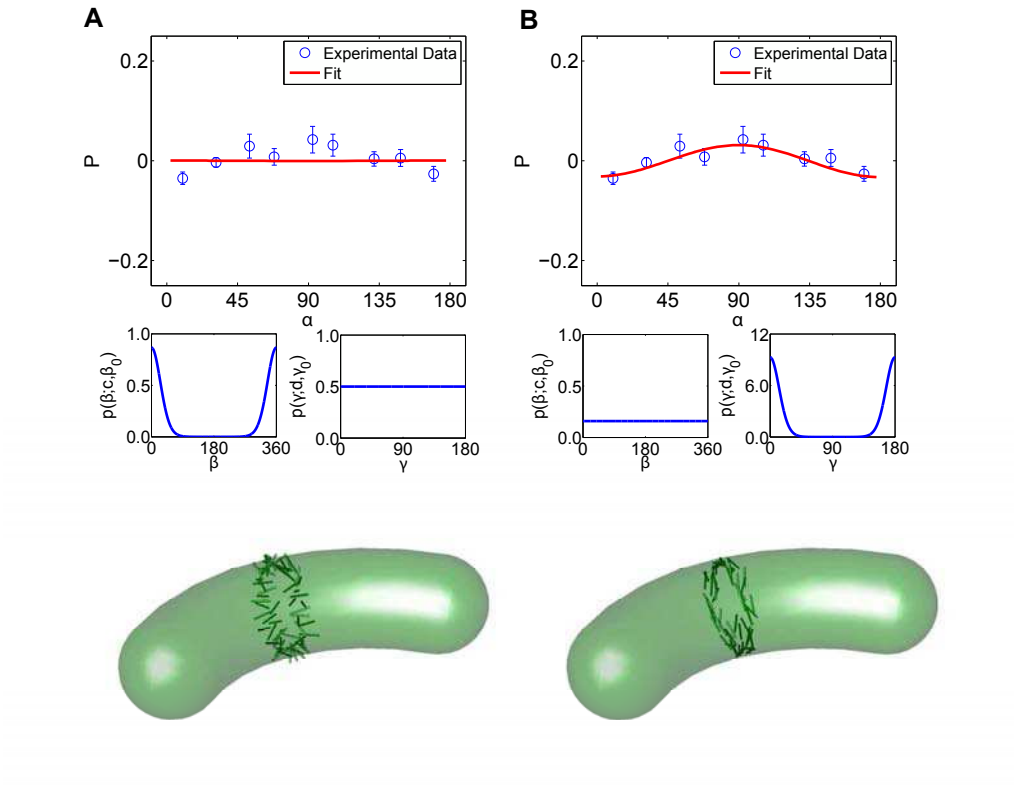

Figure 2.14: Analysis of the polarization anisotropy data from the side view for C-terminal FtsZ-YFP in *C. crescentus*. (**A**) is the fit using an average axial orientation (see Fig. 2.11). (**B**) is the fit using a circumferential average orientation. Now, the axial orientation cannot explain the data but the circumferential orientation fits the data well. Therefore, we conclude that FtsZ in *C. crescentus* is oriented in the circumferential direction.

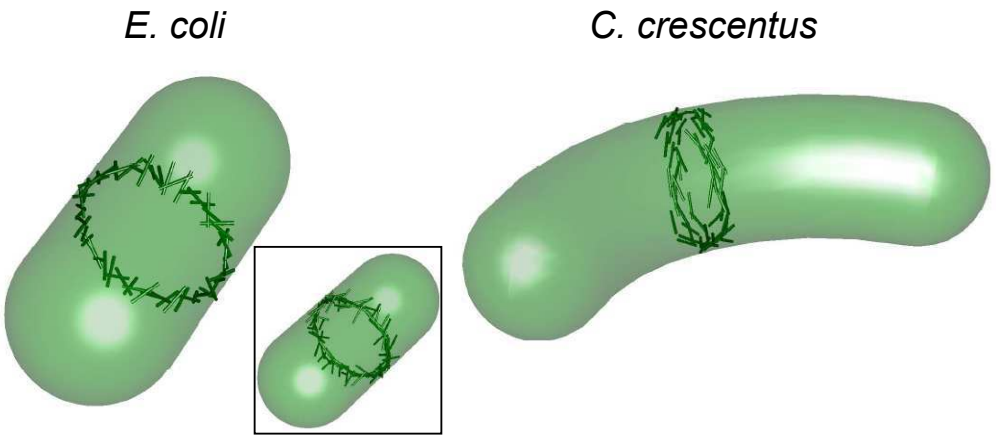

Figure 2.15: Pictorial representation of FtsZ filament organization in *E. coli* and *C. crescentus*. The angular orientation of filaments is generated from probability distributions fitted to experimental data. The results indicate that FtsZ filaments are disorganized in *E. coli* but aligned circumferentially in *C. crescentus*. For it E. coli, a Z-ring organization where regions of the ring are circumferential and toward the edge is axial could also explain our data (inset). Higher-resolution studies are needed to distinguish between these models.

2.6 Dividing versus non-dividing cell

To check whether FtsZ organization changes during cell division and septum formation, we examined the polarization signal for dividing versus non-dividing cells. Two methods were utilized. In the first method, we classify cells by the presence of a visible septum (Fig. 2.16, A and B). These cells show similar level of polarization anisotropy. There is no difference between cells with septum and without. Next, we synchronize cells in grown in poor nutrient conditions. We synchronized C-terminal FtsZ-GFP *E. coli* cells using DL-serine hydroxamate, which stops cell cycle by halting the new round of DNA replication. After washing out serine hydroxamate, cells resumed the cell cycle. Polarization microscopy is performed within the first cell cyle, and data is collected before and after the formation of visible septum. In side view, the polarization anisotropy results are shown in Fig. 2.16. Again, we find no significant difference in FtsZ organization in dividing vs. non-dividing cells (Fig. 2.16). In both of these phases, FtsZ filaments appears to be similarly disorganized before and after division. This suggests that FtsZ organization remains relatively constant throughout division. In a previous study, we measured the overall fluorescence as a function of contraction radius. It was found that the fluorescence intensity is constant during contraction, suggesting that the total number of FtsZ molecules remained relatively constant (6). These previous results, combined with the polarization results, suggest a picture of a disordered Z-ring contraction by increasing the filament density. However, the Z-ring appears to be different in poor nutrient conditions and fluores-

cence signal from the ring is significantly less. The polarization signal is also less pronounced in the poor nutrient condition. Therefore, these results suggest that the Z-ring is similarly disorganized before and during cell division, although the actual composition of the ring and the number of FtsZ filaments depend on nutrient level of the medium.

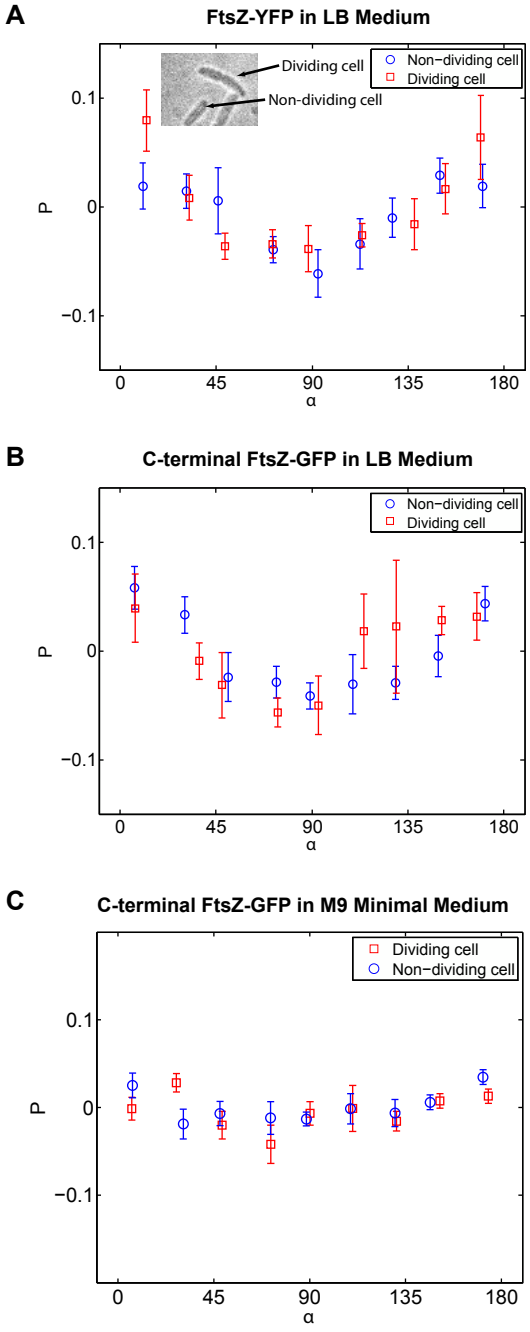

Figure 2.16: Comparison of polarization anisotropy for dividing and non-dividing *E. coli*. (**A**) FtsZ-YFP. (**B**) C-terminal FtsZ-GFP. Both results show no discernible difference between dividing and non-dividing cells, suggesting that FtsZ organization does not change during division.

2.7 Additional Controls

2.7.1 Results for Septin in Yeast

To check that our results are not artifacts from the microscopy apparatus, we use the same setup to measure polarization anisotropy in a system with verified filament alignment. In *Saccharomyces cerevisiae*, the division protein septin forms a filamentous ring at the division site. It was found that during cytokinesis, the orientation of septin filaments rotate from the cell axis direction to the circumferential direction [43]. This orientation change coincides with the formation of two split division rings. Fig. 2.17 shows the polarization anisotropy results obtained for *S. cerevisiae* strain Cdc12-ConGFP4 (courtesy of A. Gladfelter Lab), which was used in the original experiment. Our apparatus completely reproduces the polarization change, which indicates that our measured polarization anisotropy is not an instrument artifact.

2.7.2 Engineering FtsZ-GFP linkages

In the constructs examined so far, the fluorophore is linked to FtsZ via a flexible linker either at the C-terminal or N-terminal end. These constructs all showed similar behavior, suggesting a disordered FtsZ organization. As a positive control, we can engineering rigid linkers between FtsZ and fluorophores, so that a more accurate picture of FtsZ orientation can be obtained. The rigid linker can also potentially

rotate the fluorophore dipole with respect to the filament, which would give a different polarization anisotropy signal. And this rotation can be observed in live cells, then we can be confident that the GFP-dipole is an accurate reporter of the FtsZ filament orientation. We attempted to do this by both truncating the linker as well as inserting a rigid helical section Nic96 from *Saccharomyces cerevisiae*.

Several constructs of this type are made. These are:

- Z-Nic96linker-truncGFP (clone F10)= *E. coli* FtsZ (residues 1-383, full-length)-Nic96 (residues 826-831 of the 839aa protein)-GFP (residues 6-238 of the 238aa protein)
- FLAG-Z-Nic96linker-truncGFP (clone H4)
- truncZ-truncGFP (clone E2) = *E. coli* FtsZ (residues 1-379 of the 383aa protein)-GFP (residues 6-238 of the 238aa protein)
- FLAG-truncZ-truncGFP (clone G1)
- Z-mCherry-Z (clone 2)= *E. coli* FtsZ (residues 1-176 of the 383aa protein)-SGSS (linker peptide)-mCherry-SGAPG (linker peptide)-*E. coli* FtsZ (residues 177-383 of the 383aa protein)

Many of these constructs were unfortunately not viable. From two that did grow and show fluorescence signal (F10 and E2), no signficant polarization anisotropy was detected (Fig. 2.18). These constructs are likely disordered, which cannot report on

the organization of FtsZ effectively. If a rigid linker between FtsZ and fluorophore could be found, then a clearer picture of FtsZ in the Z-ring can be obtained.

2.7.3 Polarization anisotropy of FtsZ in cells without MinCDE

The MinCDE system regulates the location of the Z-ring by inhibiting the assembly of FtsZ outside of the midcell region. MinC inhibits polymerization of FtsZ *in vitro* and have been shown to oscillate from cell pole to cell pole *in vivo* [54, 58, 59]. Cells without MinCDE will form Z-rings not only in midcell but also near the cell poles. To check whether the orientation of FtsZ filaments in the Z-ring is affected by the Min system, we performed polarization microscopy for MinCDE deletion strain WM3486 with FtsZ-GFP. *E. coli* cells without MinCDE have multiple Z-ring at mid cell or near the cell poles (Fig. 2.19). Again, our quantitative analysis show that the organization of FtsZ filaments is disordered. This is true for the mid cell as well as polar Z-rings (Fig. 2.19). The orientation distributions of FtsZ fitted by circumferential and axial alignments both show disordered organization (Fig. 2.19), and results seem to suggest that Z-rings are slightly more disordered in these cells. However the difference is small, This suggests that the MinCDE system is only inhibiting the assembly of FtsZ, but not significantly regulating the organization of FtsZ filaments once the Z-ring has formed. This is reasonable since the Z-ring typically assembles in

regions of low MinC concentration.

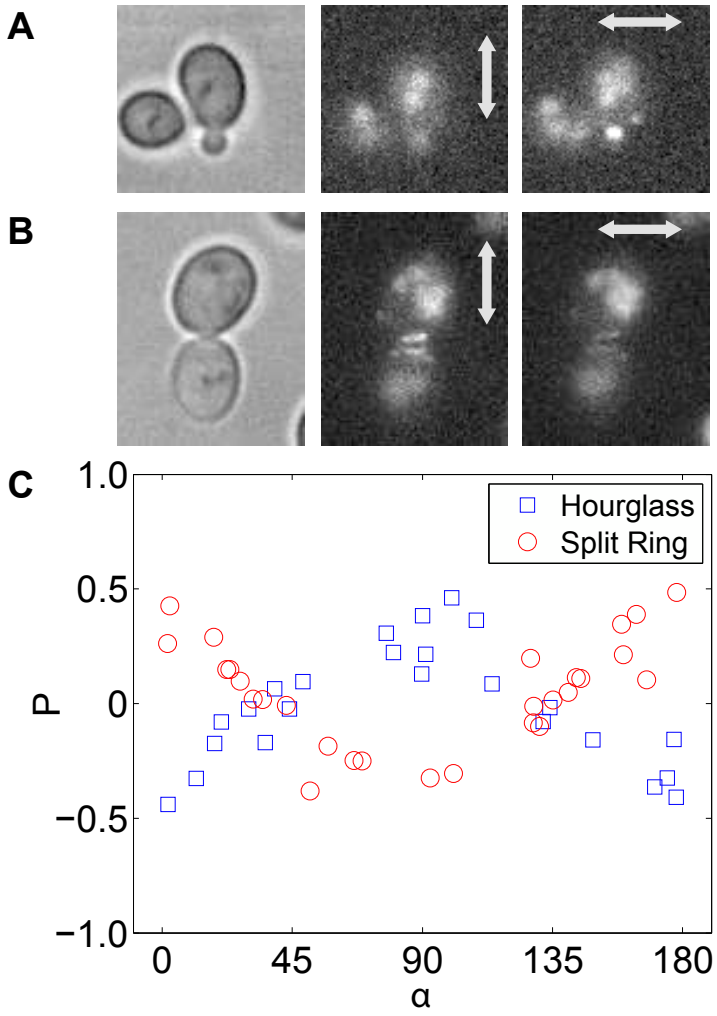

Figure 2.17: Polarization control using *S. cerevisiae*. (**A**) Images of Cdc12-ConGFP4 in the hourglass phase. Fluorescence images with vertical and parallel polarizer. (**B**) Images of Cdc12-ConGFP4 in the split ring phase. Fluorescence images with vertical and parallel polarizer. (**C**) Measured polarization anisotropy as a function of the angle of the cell with respect to the Lab X-axis. The complete rotation in polarization anisotropy is observed.

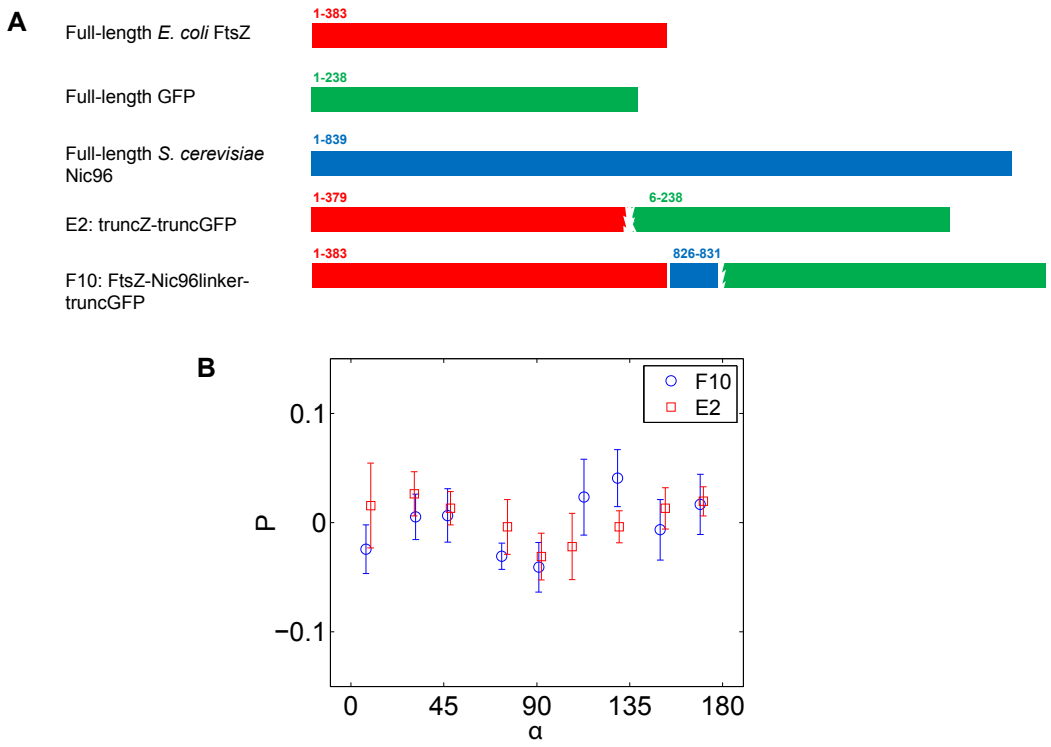

Figure 2.18: Polarization anisotropy data for Z-linker constructs F10 and E2. (**A**) The E2 construct is obtained by deleting several residues in the C-terminal linker between FtsZ and GFP. The F10 construct is obtained by inserting a segment of Nic96 between FtsZ and GFP. (**B**) The polarization data for these constructs, unfortunately, did not show discernible anisotropy.

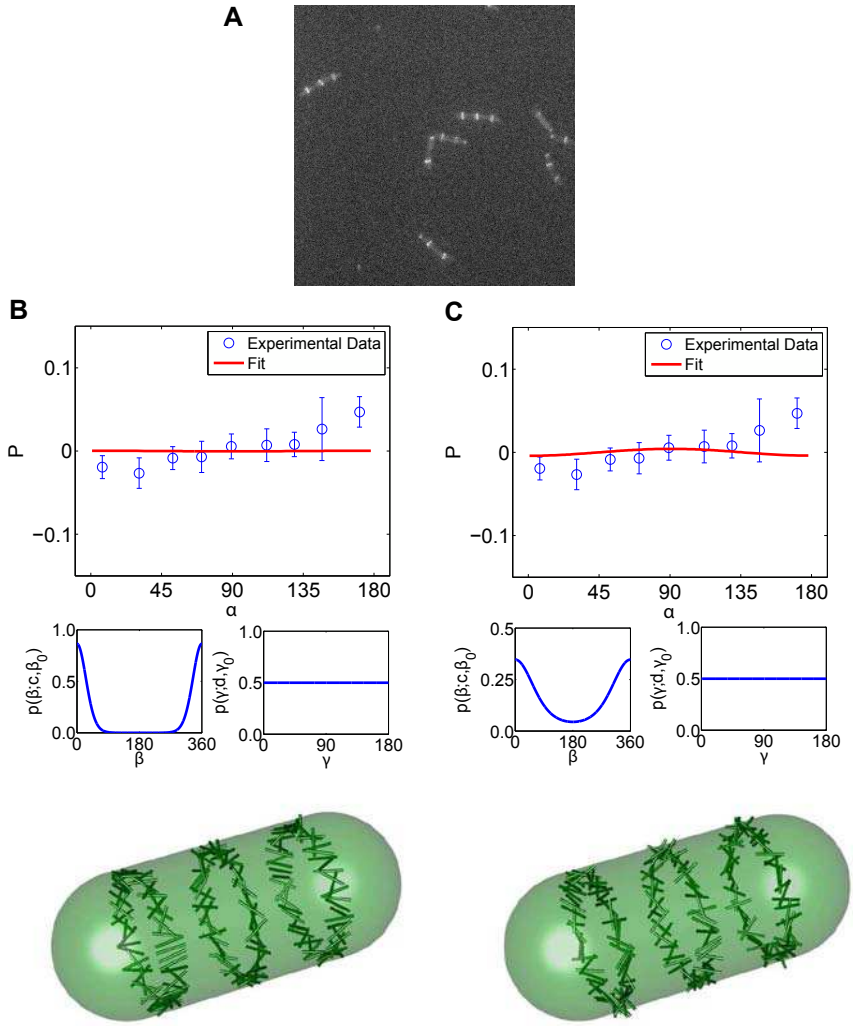

Figure 2.19: Analysis of the polarization anisotropy data from the side view for FtsZ-GFP in a MinCDE deletion strain of *E. coli*. 176 cells are included. (**A**) fluorescent image show that most cells have two or three Z-rings (B) Fit to the polarization anisotropy using an average axial orientation (see Fig. 2.11). (**B**) Fit to the polarization anisotropy using a circumferential average orientation. The distribution for γ is almost uniform for all Z-rings in these cells. The results suggest a disorganized Z-ring when the MinCDE system is not present.

2.8 Discussion

The organization and alignment of FtsZ filaments in the Z-ring have important implications for the mechanism of bacterial cytokinesis. Using PFM to probe the spatial orientation of FtsZ in live bacterial cells, we found that the data suggests that FtsZ filaments are disordered in *E. coli*. This is in contrast to the primarily circumferential alignment of filaments generally assumed to exist at Z-rings. This result is also consistent with results from super resolution measurements of Z-ring structure in *E. coli* [13]. Interestingly, *C. crescentus* FtsZ filaments do exhibit such a circumferential alignment, in agreement with data from cryo-electron tomography. The reasons for the different alignment of *C. crescentus* FtsZ vs. the others are not known. The difference in the cell diameter in *E. coli* and *C. crescentus* may play an important role here. However, *C. crescentus* FtsZ has a much longer peptide linker connecting its core polymerization domain with the C-terminal tail than does FtsZ of *E. coli*, perhaps changing the interaction of *C. crescentus* FtsZ with membrane curvature. The degree of curvature of FtsZ filaments in cells is not known, but it is possible that most straight FtsZ filaments align in the cell-axis direction in *E. coli* to avoid having to conform to an energetically unfavorable curved circumferential direction. Unlike the axial to circumferential switch characteristic of septins at the yeast bud neck during cytokinesis, *E. coli* FtsZ did not undergo any cell-cycle dependent organizational changes, as FtsZ filaments were similarly disorganized before and after initiation of visible septation.

Conclusions from the measurement require that the fluorophore dipole is an accurate reporter of the FtsZ-filament direction. To minimize possible artifacts, we have measured multiple fluorophores tagged at multiple locations on FtsZ, and found consistent results. We have also manipulated the linker between GFP and FtsZ, and searched for constructs with a different GFP dipole orientation. It is also possible that somehow the cellular environment affects how GFP fluctuates around the filament. We cannot completely rule out these effects. From the best available data, however, we can tentatively conclude that FtsZ filaments are disordered in *E. coli*, and oriented in the circumferential direction in *C. crescentus*.

Our finding of disordered orientation of FtsZ filaments raises additional questions. For instance, it is possible that the Z-ring has a mixed organization of randomly oriented filaments, as illustrated in Figure 5, and a segregated organization, where a central region of circumferential filaments with less organized orientation at the rim of this core [60, 61]. Since the PFM has poor spatial resolution, we cannot exclude this possibility. In addition, in *E. coli* cells with fluorescently tagged FtsZ, occasionally the Z-ring seems to lose coherence and develop into spiral-like structures [62, 63]. It is unclear how disordered FtsZ filaments can organize into a helical spiral. One possible explanation may be inferred from recent findings about MreB, another cytoskeletal bundle thought to exist as a helical spiral in prokaryotic cells [64]. High-resolution imaging revealed that directed movement of MreB seems to generate the observed helices, but actual MreB filaments are short and motile in *B. subtilis* [65, 66]. A

similar explanation could be valid for FtsZ.

Recently, it has been shown that artificially membrane-targeted FtsZ filaments can generate a contractile force on lipid tubes [10]. If this is true *in vivo*, then the orientation of FtsZ filaments should influence the direction of the contractile force. It is possible that the *in vitro* system has larger number of filaments in the bundle, which would facilitate alignment. Alternatively, from basic physical analysis of cell wall growth, there appears to be a geometric shape-instability in bacteria that could be responsible for cell shape changes in *E. coli* [20]. In this mechanism, mechanical reinforcements from MreB would regulate the invagination process instead of contractile force from the Z-ring. Thus, bacterial cell division could be the result of a phenomenon rooted in the physics of growing surfaces. By recruiting cell wall synthesis and turnover proteins, FtsZ may simply regulate the timing of cell division and do not directly generate mechanical forces. Recent observations on protoplasts from *B. subtilis* also revealed that FtsZ is not needed during division of wall-less bacteria [67, 68]. Our results and others indicate that new mechanistic models for FtsZ maybe needed to arrive at a consistent picture of bacterial cytokinesis.

Chapter 3

Bacterial morphology and growth under mechanical compression

We carry out microfluidic experiments to quantitatively examine growth rate, division, DNA replication, and protein synthesis in *E. coli* cells under external mechanical compression. We apply long-term, uniform forces on the lateral cell wall and find that the shape of *E. coli* cells reversibly goes from rod-like to pancake-like. The cell volume and growth rate (volume/time) of cells are nearly insensitive to mechanical compression for reasonable compression depths. Growth of the cell wall (PG synthesis) occurs on the entire cell periphery with no discernable inert poles. The average division time of the pancake-like cells is comparable with normal cells, but the division time shows greater variation. We show that the rate of cell radius of curvature (ROC) change is inversely proportional to the local ROC. Interestingly, there

exists a stable ROC at which the rate of ROC change vanishes. The stable ROC is consistent with predictions of the mechanochemical model. MreB can influence this steady ROC, which suggests a mechanical role for MreB during cell wall growth that influences the final shape of the cell.

3.1 Air-driven microfluidic device applying compression force to bacterial cells

Air-driven valve is an easy-to-use method of controlling flows in microchannels, and has been widely used in microfluidic devices such as largescale biochips [69]. The deformation of PDMS driven by air pressure can be utilized to apply mechanical forces to cells and tissues [70, 71].

3.1.1 Design of air-driven microfluidic device

Here we employed air-driven deformation of PDMS to apply compression force to bacterial cells. We fabricated a microfluidic device with upper and lower chambers separated by a PDMS layer of 200μm in thickness. The upper chamber can be inflated by positive air pressure. The lower chamber is where cells were cultured, and was 5×5mm in size and 250μm in height Fig. 3.1, left). The variable air pressure in the upper chamber deforms the PDMS membrane downward and applies a mechanical

force on the *E. coli* cells.

Within this device, the compressive force applied on individual cells can be estimated, but the precise value of the compressive force depends on the pressure in the air chamber, and the thickness and elastic modulus of the PDMS layer. In addition, the elastic modulus of PDMS (2.2MPa, measured in our experiments) and *E. coli* cells (20MPa [72]) are of similar order, therefore the assumption that either the PDMS layer or the cell body is rigid is not applicable. Thus, instead of controlling the compressive force, we use a design where we can precisely control the deflection of PDMS by introducing micropillars. Micropillars made by photoresist were deposited onto the bottom cover glass of the lower chamber, and were used to support the membrane, providing a maximum limit of the PDMS membrane deformation as well as the deformation of the underlying cells. The typical height of micropillar is 0.8-0.9μm, which is slightly thinner than average *E. coli* cell thickness (typically 1 μm), and thus achieving a moderate deformation of the cell body. To prevent possible buckling, the diameter of micropillar is set to 6μm, much larger than its height. All micropillars were patterned hexagonally on the cover glass substrate with 10μm distance between each pillar. In this fashion, PDMS layer sagging can be ignored (Fig. 3.1, right).

3.1.2 Fabrication of air-driven microfluidic device

Molds to print the culture chamber and air chamber were fabricated by negative photoresist (SU8-2100, MicroChem Corp.). Typical soft lithography procedure was

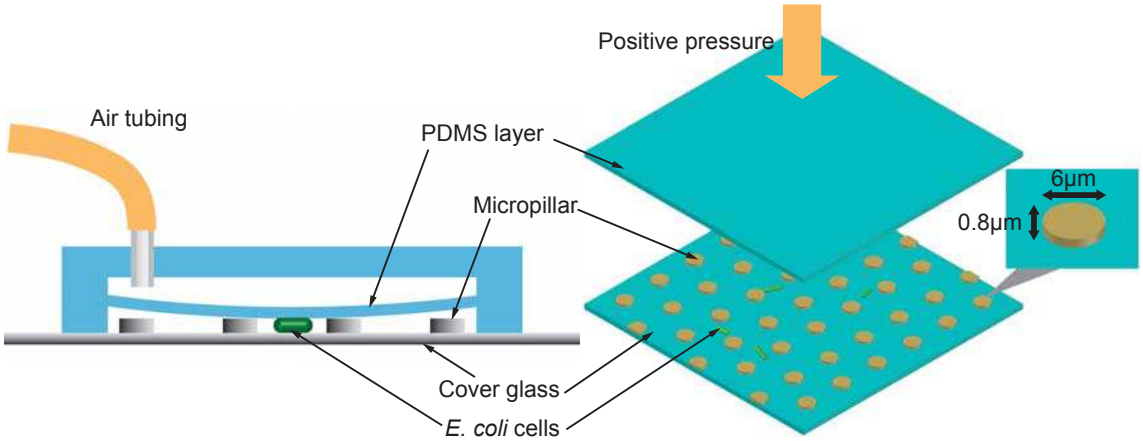

Figure 3.1: Design of air-driven microfluidic device. Left: Side view of the device. The device contains two chambers. The upper air chamber and lower cell culture chambers are separated by a PDMS layer of 200μm in thickness. The PDMS layer is deformed downward to compress cells in the culture chamber when there is positive pressure in the air chamber. Micropillars made by a photoresist are deposited onto the coverglass, which support the PDMS layer when pressure is applied. Right: 3D view of the device. Mircopillars are patterned hexagonally with a distance of 10μm between pillars. Pillar diameter is 6μm and typical height is 0.8-0.9μm.

applied to fabricate our microfluidic devices; 200μm thick layer of PDMS (1:10 of agent to base, Sylgard 184, Dow Corning Corp.) was spun onto the mold of culture chamber and 7mm thick PDMS was poured onto the mold of air chamber. Both layers with half-cured PDMS was carefully aligned and then baked until completely cured. Micropillars were fabricated by patterning positive photoresist (s1813, MicroChem Corp.) onto pre-cleaned cover glass (premium cover glasses, Fisher Scientific), and the height of micropillars was measured by profilometer (Dektak II) after every experiment. The PDMS and coverglass were bonded after oxygen plasma treatment and baked overnight for use.

Before the experiment, 1% poly-ethylenimine (Sigma-Aldrich, Inc.) with LB

medium was added into culture chamber, left standing for 1 hour for coating. Diluted cell culture was then injected into culture chamber through tubing, with some cells immobilized by the poly-ethylenimine coating. Fresh LB medium was then constantly pumped through chamber to assure exponential growth of cells.

3.1.3 Culturing cells in microfluidic device

E. coli cells were flown with LB medium into the culture chamber (Fig. 3.2. To ensure a number of cells are immobilized during the loading and unloading processes of compression, 1% poly-ethylenimine was added with LB medium. A moderate pressure (∼5psi or 34kPa) in the air chamber was kept constant by a pressure regulator. The downward movement of PDMS layer stopped when the layer contacted micropillars and applied a constant force on the bacterial cells. During compression, temperature of 37 C° was maintained and fresh LB medium was supplied by a constant flow of the growth medium, thus assuring that *E. coli* cells stay in the growth phase.

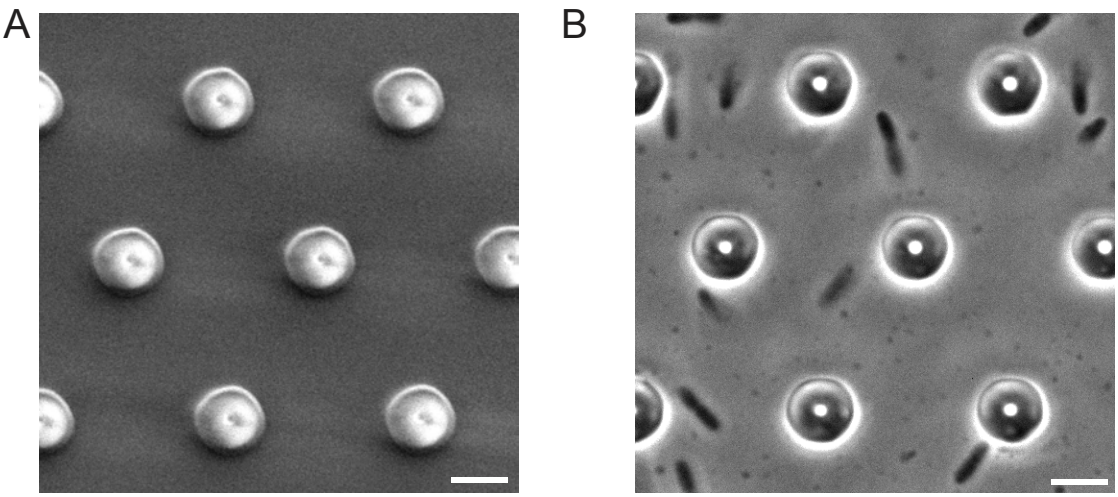

Figure 3.2: Culturing cells in microfluidic device. (**A**) Low vacuum scanning electron microscopy image of micropillars on the coverglass. (**B**) Phase contrast image of live *E. coli* cells distributed in the culture chamber between micropillars. Before compression, cells swim and diffuse within the chamber normally. Some cells adhere onto the bottom from the poly-ethylenimine coating. (Scale bars, 5μm)

3.2 Bacterial strains and growth conditions

The bacterial strain used for measurement of cell volume, radius of curvature, DNA content and cell division was WM2724, a lac- derivative of E. coli MG1655 (WM1074) that expresses ftsZ-gfp from an ectopic site on the chromosome under control of the IPTG-inducible trc promoter. The strain for measuring protein synthesis was WM3497, a derivative of WM1074 that carries plasmid pDSW209, which expresses gfp only. The strain for measuring colocalization of MreB with areas of cell wall synthesis was WM4235, which carries an mreB-mCherry-mreB sandwich fusion at the native mreB locus [73]. WM1283, harboring a thermosensitive plasmid ex-

pressing ftsZ and an ftsZ chromosomal null mutation, was shifted to 42°C to inhibit cell division.

WM2724 and WM3497 were cultured in LB broth overnight at 37°C, whereas WM4235 was cultured at 30°C. One hour prior to microscopy, cell cultures were diluted and grown until reaching an OD600 of 0.1. IPTG was then added to WM2724 (0.05 mM) and WM3497 (0.5 mM) to induce FtsZ-GFP or GFP, respectively.

To stain the cell wall, wheat germ agglutinin and oregon green 488 or Texas Red conjugate (WGA488 or WGA-TexasRed, Life Technologies) with final concentration of 10μg/ml was added with diluted cell culture 10min prior to microscopy, also together with fresh medium. To stain the DNA, Hoechst 33342 (Life Technologies) with final concentration of 10μg/ml was added with fresh medium after cells were compressed into irregular shapes.

3.3 Microscopy and data analysis

All microscopy was done on Nikon TE2000 microscope with phase contrast and epifluoescence. Before compression, cells were allowed to grow at proper temperature in an incubator box (live cell unit, Pathology Devices) for 20 minutes to reach exponential growth. During compression, multiple positions within the contact region in the culture chamber were selected and captured for every 10-12 minutes. After 3 hours of compression, pressure in the air chamber was unloaded, and the capture

was continued for another 8-12 hours to record the cell growth when compression was removed. The analysis of cell volume, protein synthesis, DNA content, MreB-cell wall co-localization and change of radius of curvature were all performed by custom algorithms in Matlab (MathWorks, Inc.).

3.4 Bacterial cell growth rate, protein synthesis and DNA synthesis under compression

3.4.1 Growth rate of bacterial cell under compression

E. coli cells were immobilized when compressed by the PDMS layer. The contact region between cells and the bottom cover glass (or the upper PDMS layer) increased immediately after compression, suggesting that cells were mechanically squeezed (Fig. 3.3A, 1st and 2nd frame). Cells also immediately restored their original shape when we released pressure after a short (<1 min) compression (data not shown): confirming that the deformation during the initial phase of compression is elastic. When the compression was applied for 60-90 minutes, instead of axial elongation seen in constraint-free cells, compressed cells expanded outward along the whole periphery,

including the original pole regions. Cells eventually developed into flatten shapes with ruffled outline and bulges (Fig. 3.3, A and B).

These observations raised two possibilities: that the irregular expansion of the cell wall is due to either cell growth or a physical deformation stemming from a viscoelastic response of the cell wall to mechanical force. To find out which of these mechanisms underlies the long-term response of cell shape change, we first measured the rate of cell volume change for both compressed and normal cells. For the compressed cells, the volume was calculated by multiplying the cell-substrate contact area (by a cell-outlining algorithm) by the height of micropillars (Fig. 3.3B).

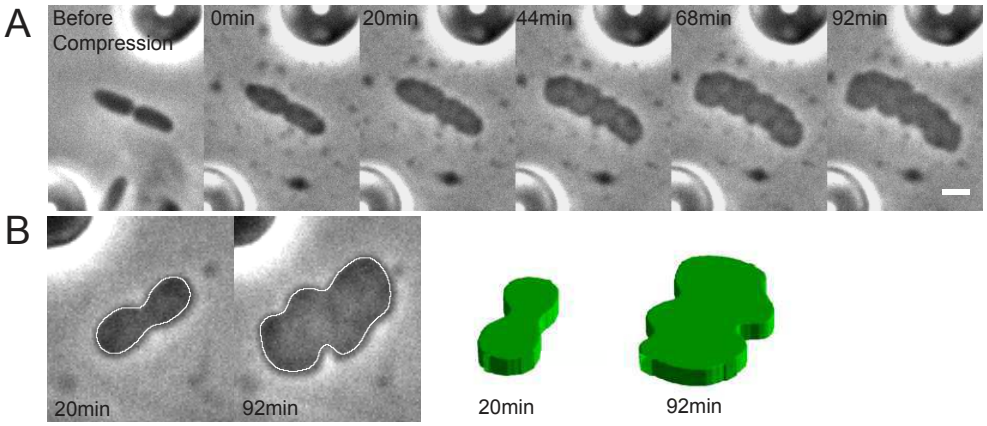

Figure 3.3: Cell shape in *E. coli* cells during mechanical compression. (**A**) Phase contrast images of cell shape evolution before and after compression is applied. (**B**) Outline of cell cross-sectional area under compression and the corresponding 3D view of reconstructed cell shape. (Scale bars, 2μm)

For the normal cells, volume was obtained by calculating the volume of a cylinder with two hemispherical caps. We found (Fig. 3.3B) similar increase of cell volume versus time for both compressed and normal cells (Fig. 3.4A). Their rates of volume

change also showed little difference (Fig. 3.4B), which suggests that the expansion rate of compressed cells is comparable to that of normal cells. We also fit the increase of cell size by an exponential function $V_t = V_0 2^{at}$ where V_t and V_0 are the current and initial cell volume, t is time and a is growth rate. The growth rates for normal and compressed cells are very close (Fig. 3.5A and B). In addition, we explored cell volume change under different amounts of compression controlled by micropillars of different heights. For micropillars taller than 0.7μm, the rate of volume increase was close to that of normal cells. However, the rate of volume increase was near zero when micropillar height is 0.5μm (Fig. 3.6). The reason for this is not known, but may be related to altered functions of FtsZ and ribosome under pressure [74, 75]

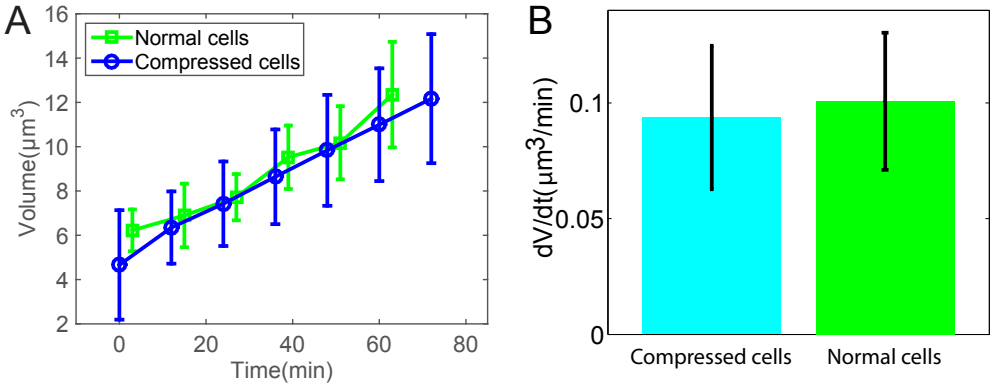

Figure 3.4: Cell volume changes in *E. coli* cells during mechanical compression. (**A**) Volume change of compressed and normal *E. coli* cells within 80 minutes. (n=7 and 9 for compressed and normal cells, respectively. Error bars indicate standard deviation.) (**B**) volume growth rates for compressed and normal cells. The micropillar height is 0.8μm.

We also examined cell wall synthesis in compressed cells. The cell wall was labeled by fluorescent wheat germ agglutinin (WGA-oregon green 488 conjugate, or

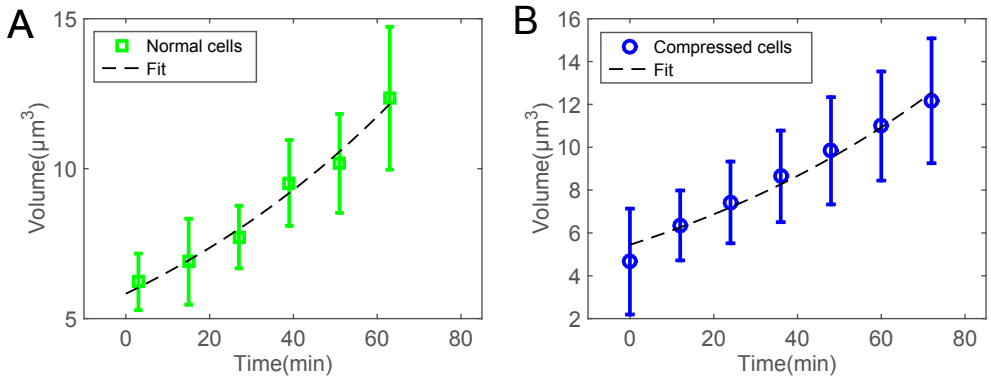

Figure 3.5: Growth rates in *E. coli* cells during mechanical compression. The increase of cell size was fit by exponential function $V_t = V_0 2^{at}$, where $a = 0.0168$ and 0.0167 for normal (**A**) and compressed cells (**B**), respectively

WGA488). During compression, fresh LB medium with 10μg/ml WGA488 was constantly supplied to visualize any newly synthesized cell wall. Fig. 3.7 shows that the cell periphery expanded with continuous fluorescence without obvious gaps. From these results, we conclude that the observed shape changes are due to alterations in cell wall growth dynamics.

3.4.2 Protein synthesis bacterial cell under compression

To further check if the compressed cells are growing with normal physiological processes, we investigated protein and DNA synthesis. *E. coli* cells expressing freely diffusible green fluorescence protein (GFP) from exogenous plasmids were examined. During compression, GFP fluorescence was not disrupted in irregular cells (Fig. 3.8A).

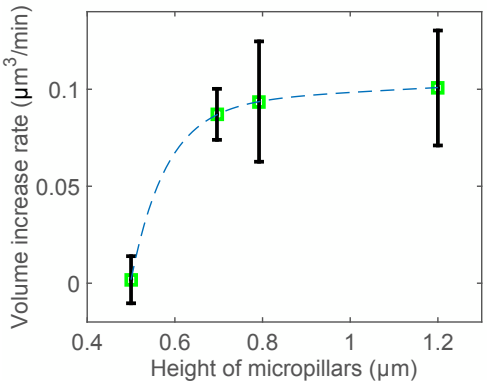

Figure 3.6: Volume change rates in *E. coli* cells at different compression. Volume change rate as a function of mircopillar height (equal to the thickness of compressed cells). Cells no longer grows when the height is 0.5μm. (n$\geq$7 for each point. Error bars indicate standard deviation.)

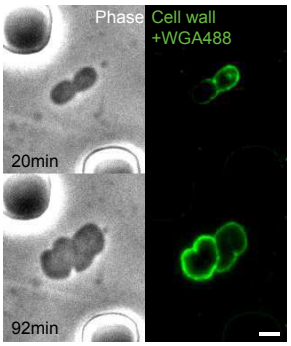

Figure 3.7: Cell wall stained by WGA Oregon green 488. *E. coli* cell stained by WGA 488 at 20 min (upper) and 92 min (lower) after compression. (Scale bars, 2μm)

The GFP fluorescence density, calculated as the ratio of total fluorescence intensity to the cell volume, was also constant as a function of time for both compressed and normal cells, indicating that the cytoplasmic concentration of GFP is constant in compressed and normal cells (Fig. 3.8B). We also examined an endogenous protein, chromosomally fused MreB-mcherry, which is the only source of MreB in the cell. During compression, the intensity of MreB-mcherry was also constant (Fig. 3.9),

demonstrating that both exogenous and endogenous proteins are expressed at comparable rates in compressed and normal cells.

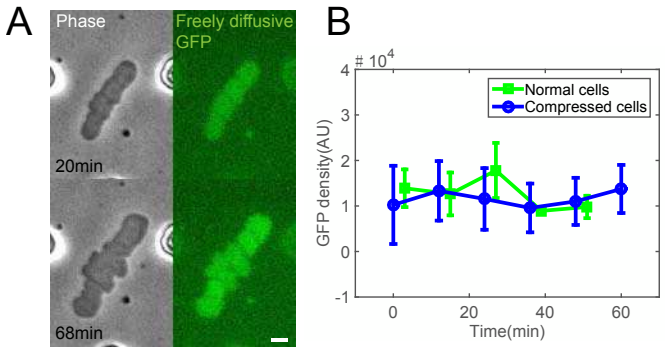

Figure 3.8: Synthesis of exogenous protein in compressed cells. (**A**) Phase contrast and fluorescence images of *E. coli* cells expressing freely diffusive GFP at 20 min (upper) and 68 min (lower) after compression. (**B**) temporal change of GFP density of compressed and normal *E. coli* cells. GFP density was calculated by integrating the total fluorescence intensity of GFP over the cell divided by the cell volume. (n=5 for both compressed and normal cells. Error bars indicate standard deviation.) (Scale bars, 2μm)

3.4.3 DNA synthesis of bacterial cell under compression

Furthermore, we asked whether the DNA replication activity was changed during compression. We labeled the bacterial DNA with Hoechst 33342 (10μg/ml) to determine DNA content in the growing cell under compression. Fig. 3.10 shows that the measured DNA content density (the ratio of total DNA content to cell volume) was higher in compressed cells than in normal cells. This might be due to increased permeability of the cell envelope or altered chromosomal structure in compressed cells.

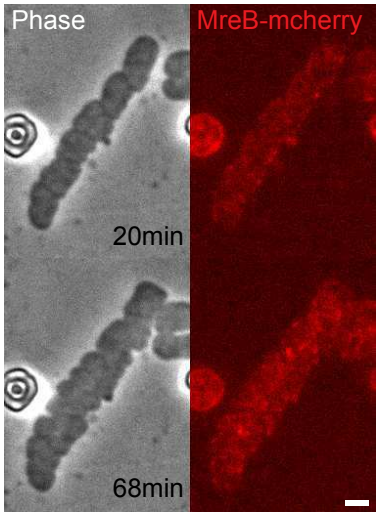

Figure 3.9: Synthesis of endogenous protein in compressed cells. Phase contrast and fluorescence images of *E.coli* cells expressing MreB-mcherry at 20 min (upper) and 68 min (lower) after compression. (Scale bars, 2μm)

Nevertheless, it shows that, in compressed cells, the DNA content increased with increasing cell volume, indicating the DNA replication was progressing. We conclude from these results that during compression, *E. coli* cells can adapt their shapes to cope with external compressive force while maintaining their physiological processes such as growth, protein synthesis, and DNA replication.

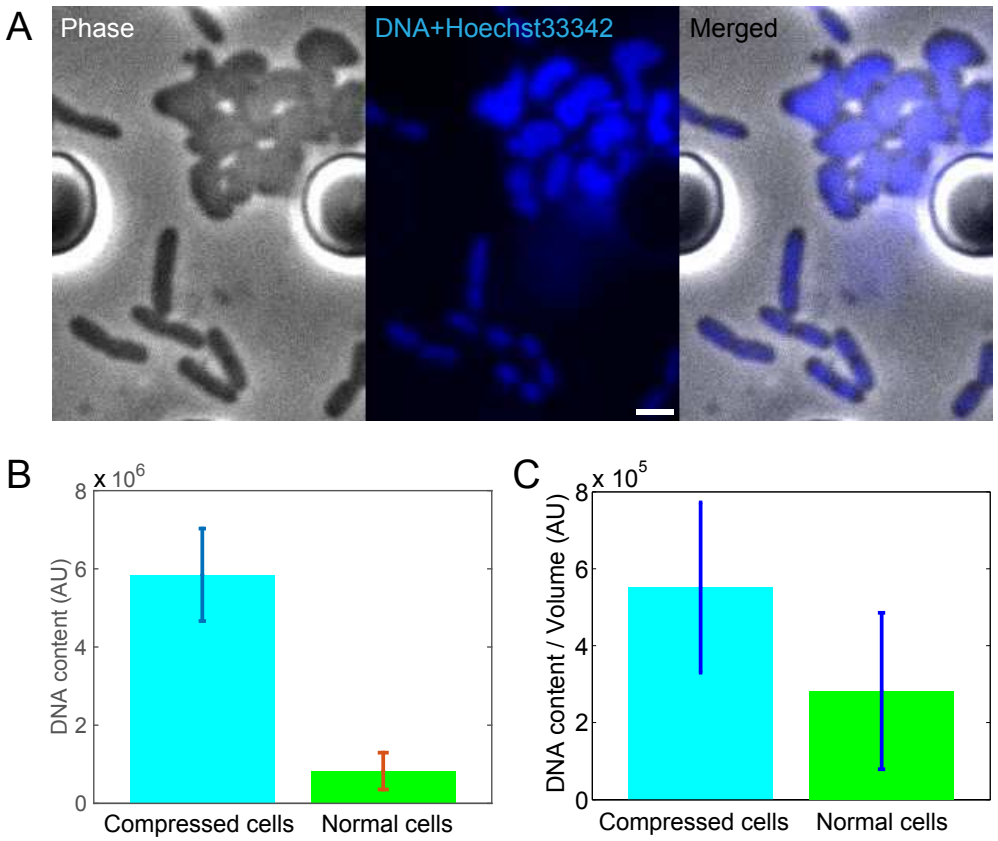

Figure 3.10: DNA synthesis in compressed cells. (**A**) *E.coli* cell was stained with Hoechst33342 for DNA, for both compressed and normal cells. DNA content (**B**) and density (ratio of DNA content to cell volume, **C**) were compared for compressed and normal cells. DNA density was calculated by integration of fluorescence intensity over whole cell. (n=9 and 10 for compressed and normal cells, respectively. Error bars indicate standard deviation.) (Scale bars, 2μm)

3.5 Bacterial cell division under compression

3.5.1 Bacterial cells divide under compression with near normal division rate

In this section, we investigate the process of cell division during mechanical compression. We showed that the cell wall was still being synthesized. Cells formed

new septa and were being separated into new cell compartments (Fig. 3.11). The daughter cells also divided normally. Next we examined the essential protein of cell division, FtsZ, which forms a ring-like structure (FtsZ-ring or Z-ring) at septum sites during cell division. In compressed cells, FtsZ-GFP still formed Z-rings, although the ring was typically not continuous around the cell. The Z-ring constricted during cytokinesis and disassembled when daughter cells segregated (Fig. 3.12A). In normal rod-shaped cells, Z-ring is oriented perpendicular to the axial direction of cell. In compressed cells with irregular shapes without a well-defined long axis, Z-ring still tended to orient in perpendicular to the long axis if the cell was slightly elongated. The Z-ring orientation is likely determined by the oscillating minCDE system [2, 76], as well as nucleoid occlusion [77], which both negatively impacts FtsZ assembly.

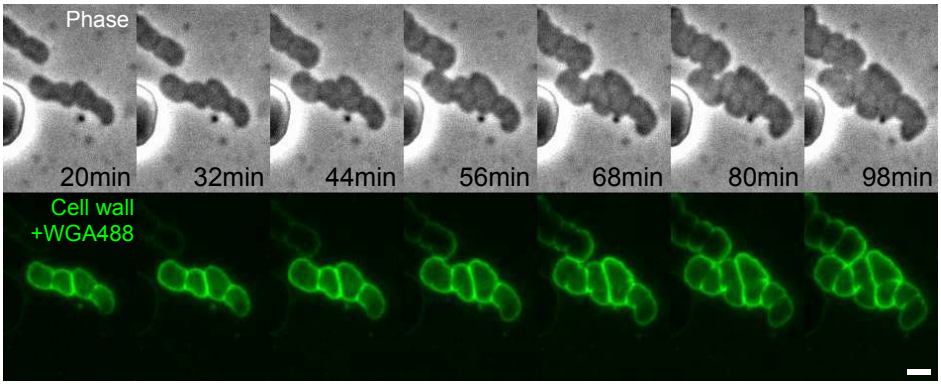

Figure 3.11: Septum formation in compressed cells. Phase contrast and fluorescence images of *E.coli* cells stained with WGA488 showing septum formation and cell division occur during compression (Scale bars, 2μm)

To identify whether the external force alters cell cycle time, we measured the division time of compressed cells. In our experiment, one cell cycle is the time between

two successive Z-ring disassembly events. The average division time of compressed and normal cells was 29±9 min and 29±6 min, respectively, which showed the average division time of the compressed cells is comparable with normal cells. However, the probability distribution of cell cycle time of compressed cells was wider than that of normal cells (Fig. 3.12B). These results showed that the variation of cell proliferation was somewhat disturbed by the compressive force.

3.5.2 Added cell size during single cell cycle under compression

Recently, a mechanism of constant added size through cell cycle was investigated for rod-shaped *E. coli* cells [78, 79]. More interestingly, for compression cells, the added cell volume (cell volume at division subtracts that at birth) increases as birth volume increases (Fig. 3.13). To explain this, although more direct evidences are still needed, one possibility is that the DNA segregation is disturbed under compression. The variations of DNA content as well DNA density are larger in compressed cells (Fig. 3.10C), indicating the copy number of DNA varies a lot more. Therefore, it is reasonable that cell born with more copies of DNA would proportionally add more cell volume throughout cell cycle. And this would also explain the larger variation of cell cycle time (Fig. 3.12B).

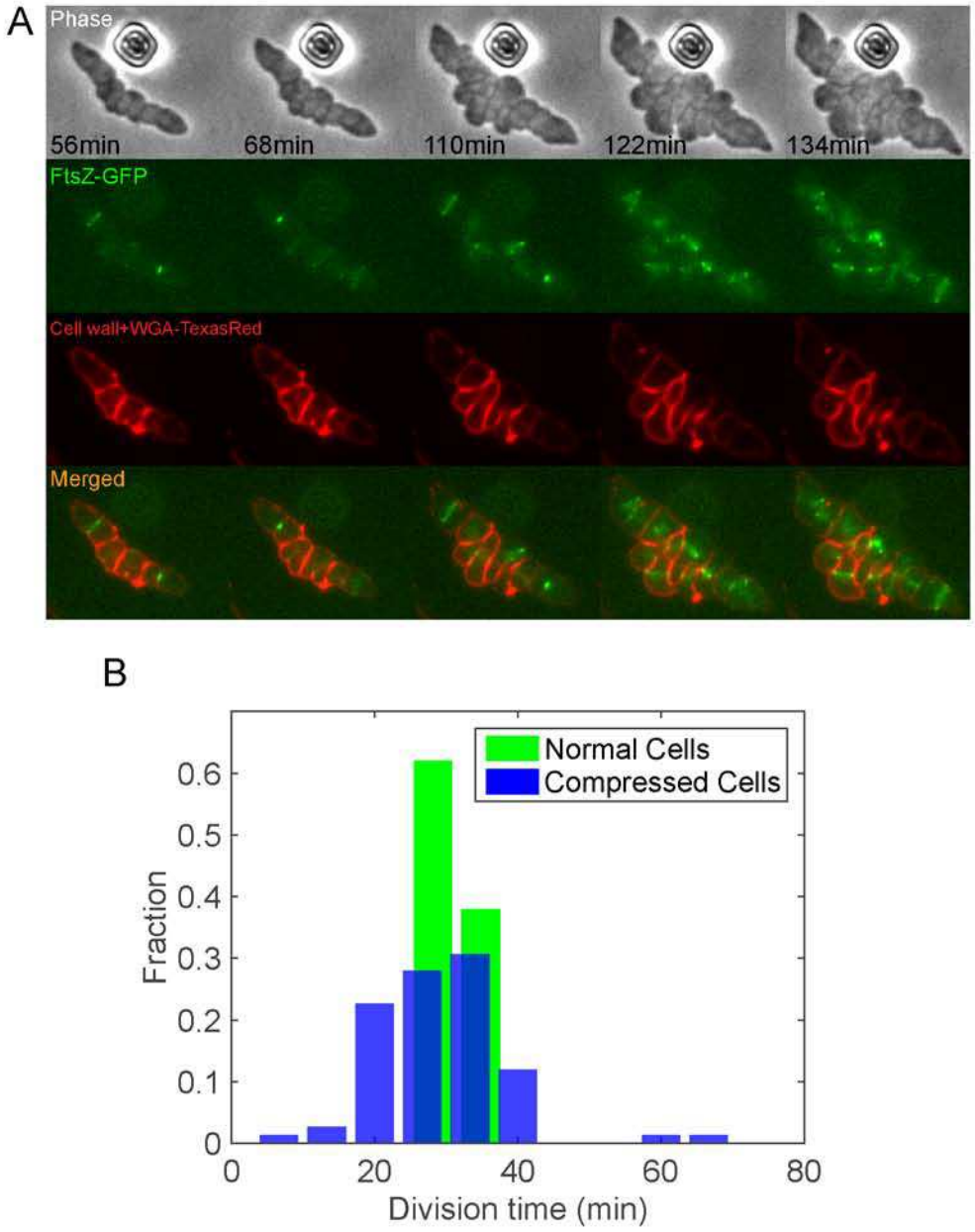

Figure 3.12: Division of *E. coli* cells under compression. (**A**) *E. coli* cells expressing FtsZ-GFP shows FtsZ-ring still forms during cell division. The FtsZ-ring is not always continuous. (**B**) Comparison of division times between compressed and normal cells. The average cell cycle length of compressed cells is not significantly different from the normal cells. However, the standard deviation of cell cycle length of compressed cells is larger. (n=75 and 71 for compressed and normal cells, respectively) (Scale bars, 2μm)

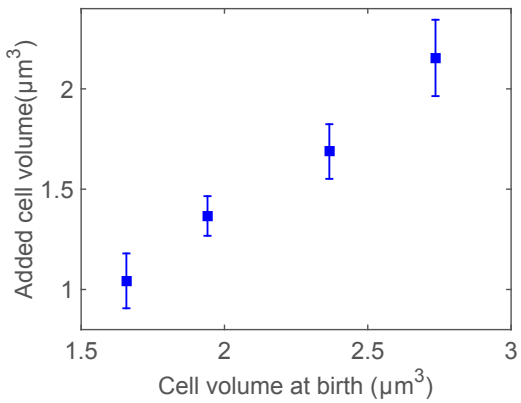

Figure 3.13: Added cell volume versus cell volume at birth throughout one cell cycle. (n≥12 for each point. Error bars indicate standard error of the mean.)

3.6 Recovery of cell shape after compression is removed

Cell growth dynamics was also monitored when the compression force was removed. The PDMS layer was lifted by unloading pressure in the air chamber, and cells continued to grow and divide. The cell shape gradually transitioned from irregular to rod-like after 2-4 cell generations (Fig. 3.14A). The recovery of cell shape cannot be accomplished within a single cell cycle but was accompanied with cell divisions and subsequent cell elongation. This shape recovery is reminiscent of recovery after removal of A22, which depolymerizes MreB. Here we observed that the shape can transition between rod-like to flat pancake-like in a similar manner using mechanical forces.

The external bending force has been shown to cause the elastic and plastic deformation of *E. coli* cells [38]. Similarly, when compression removed, the cell shape immediately recovered partly, but still largely with the pancake-like shape maintained (Fig. 3.14B). This again proved that the deformation of compressed cells also consists of both elasticity and plasticity. Moreover, when cell growth arrested by using Hoechst dye, the pancake-like cells still stayed deformed (Fig. 3.10A), which showed that the two parts of deformation do exist.

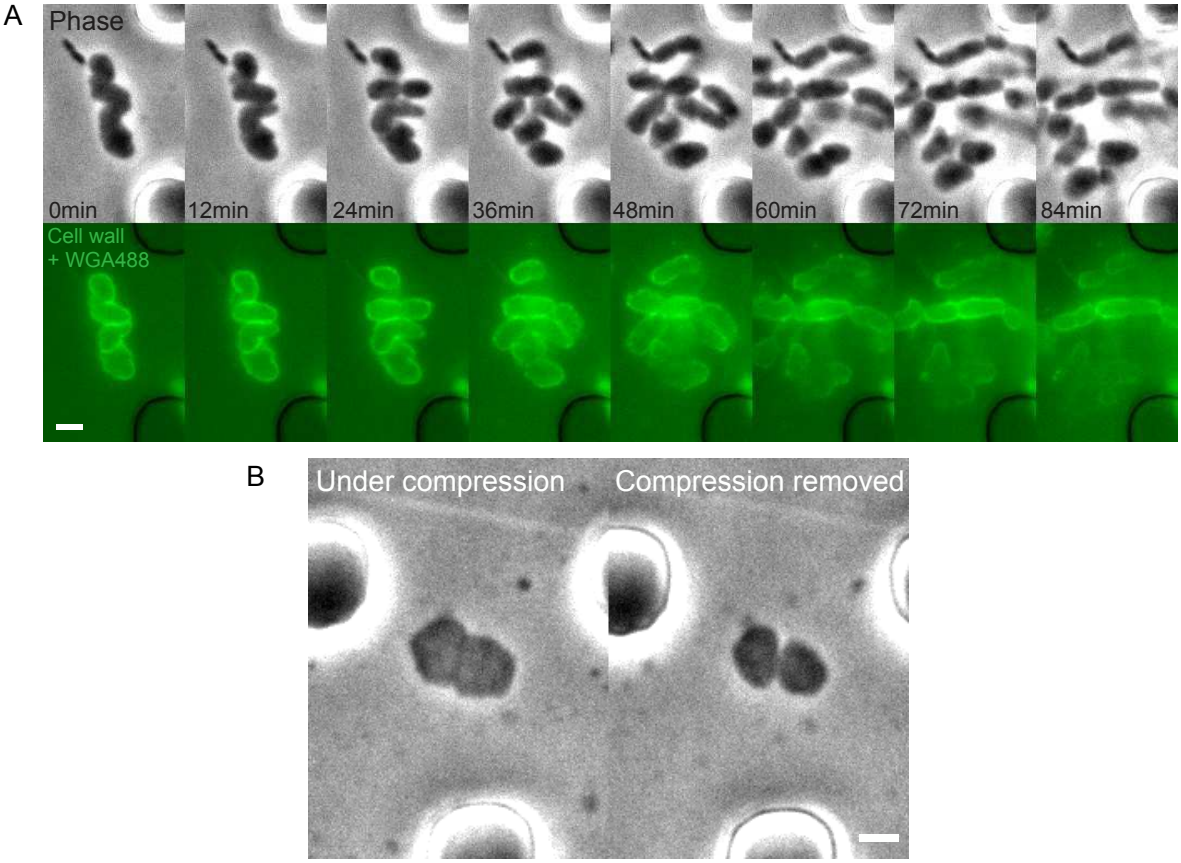

Figure 3.14: Recovery of cell shape after compression is removed. (**A**) The recovery process occurrs along with cell division and elongation. (**B**) Change of cell shape during compression and right after compression removed. (Scale bar = 2μm)

3.7 MreB dynamcis of bacterial cell under compression

3.7.1 Mechanical compression disrupts organization of the cell poles

To reveal the physical and biological mechanisms underpinning the observed robust cell growth with irregular shape, we studied the dynamics of cell wall and other

proteins involved in PG synthesis. Cell wall synthesis can be visualized using pulse labeling of fluorescent WGA [29]. During cell growth, only old parts of the cell wall were stained, but the newly synthesized cell wall does not exhibit fluorescence. Our time-lapsed images of normal cells after pulse labeling showed that cell poles remained persistently fluorescent after several cell generations (Fig. 3.15A). This is consistent with the idea that the cell poles remain inert during most of the cell cycle [29, 72]. Intriguingly, in compressed cells, cell wall growth occurred at midcell and cell poles. Cell wall elements were inserted into existing peptidoglycan network uniformly along the entire cell periphery (Fig. 3.15B), and MreB was distributed uniformly in compressed cells. Thus, mechanical compression disrupts organization of the cell poles.

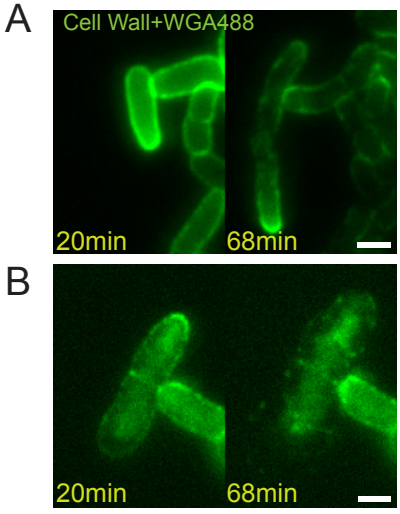

Figure 3.15: Mechanical compression disrupts organization of the cell poles. Pulse labeling of cell wall with WGA488. Cell wall keeps continuously labeled at early time and later becomes discrete when new cell wall materials inserted. (**A**) In normal cells, cellular poles remain labeled when cell is elongating with new cell wall materials inserted at midcell. (**B**) In compressed cells, cell wall materials are inserted at both polar and midcell sites. (Scale bars, 2μm)

3.7.2 Sites of cell wall synthesis is co-localized with MreB

Together with other proteins such as MreC and PBP2, MreB is involved in cell wall synthesis, and has been shown to co-localize with new cell wall insertion in rod-like cells [80, 81]. Here, we examined if a similar correlation between MreB dynamics and new cell wall exists in compressed cells. Pulse-labeled cell wall with WGA488 and chromosomal fusion of MreB-mcherry were monitored during compression. After compression was applied, the fluorescence of WGA was initially continuous with spots of MreB-mcherry distributed across the whole cell. Twenty minutes later, fluorescence of WGA became more discrete as cell expanded. In addition, MreB assembly appeared more often at the sites where little WGA488 was observed (Fig. 3.16A). By plotting the correlation between the normalized intensities of MreB-mcherry and WGA488, we see a clear transition from no correlation at initial time (T1 data) to a negative correlation (T2 data) in Fig. 3.16B. This indicates that MreB is located at the non-fluorescent sites of WGA488 where new cell wall was synthesized.

3.7.3 MreB motion in compressed cells

MreB has been found to rotate circumferentially in rod-like bacterial cells such as *B. subtilis* and *E. coli* [30, 65, 66]. This active rotational motion of MreB is driven by the cell wall assembly and maintains the rod-like shape of the cell [30]. Here we ask if

the MreB rotational motion depends on the cell shape. In compressed cells, we found that MreB was moving in a similar manner as in rod-like cells, perpendicular to the cell periphery (Fig. 3.17A). The velocities and directions of MreB motion had similar distribution as those in rod-like cells (Fig. 3.17B). Taken together, we found that there is similar degree of coordination between MreB motion and cell wall assembly in compressed cells. Therefore, the cell wall synthesis machinery is not significantly disturbed by external forces.

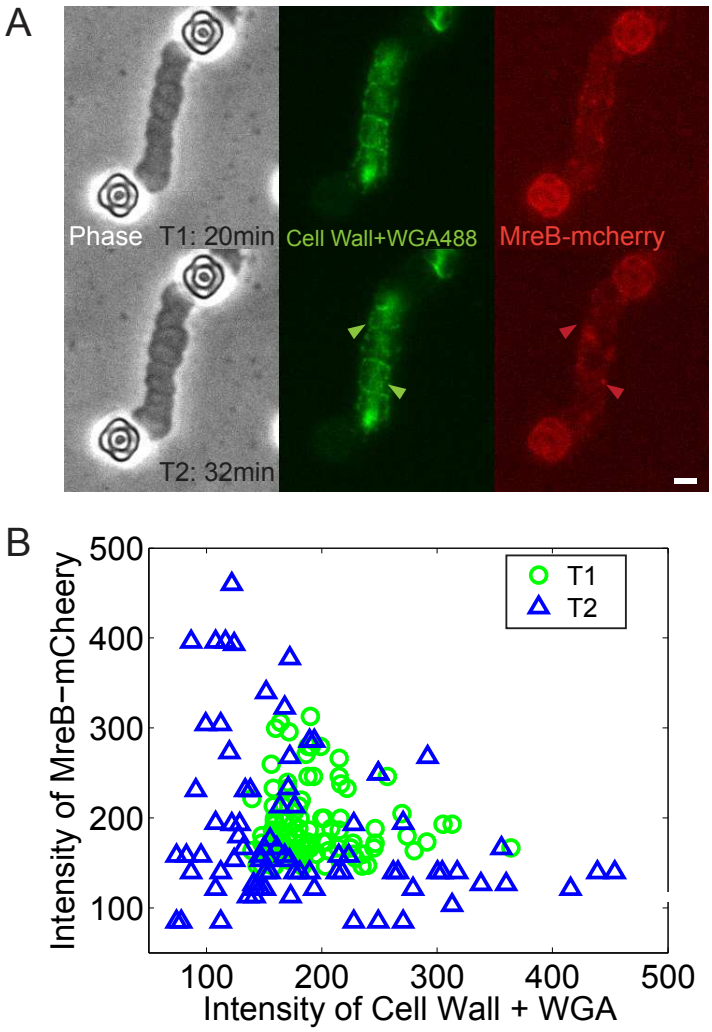

Figure 3.16: Co-localization of newly inserted cell wall and MreB in compressed cells. (**A**) Pulse-labeled cell wall together with chromosomal MreB-mcherry. Arrows show at later time after compression (32min), a negative correlation between MreB-mcherry (red) and cell wall+WGA488 (green) appears. (**B**) The correlation between intensities of MreB-mcherry and cell wall+WGA488 at earlier (T1) and later time (T2) after compression. (n=6) (Scale bars, 2μm)

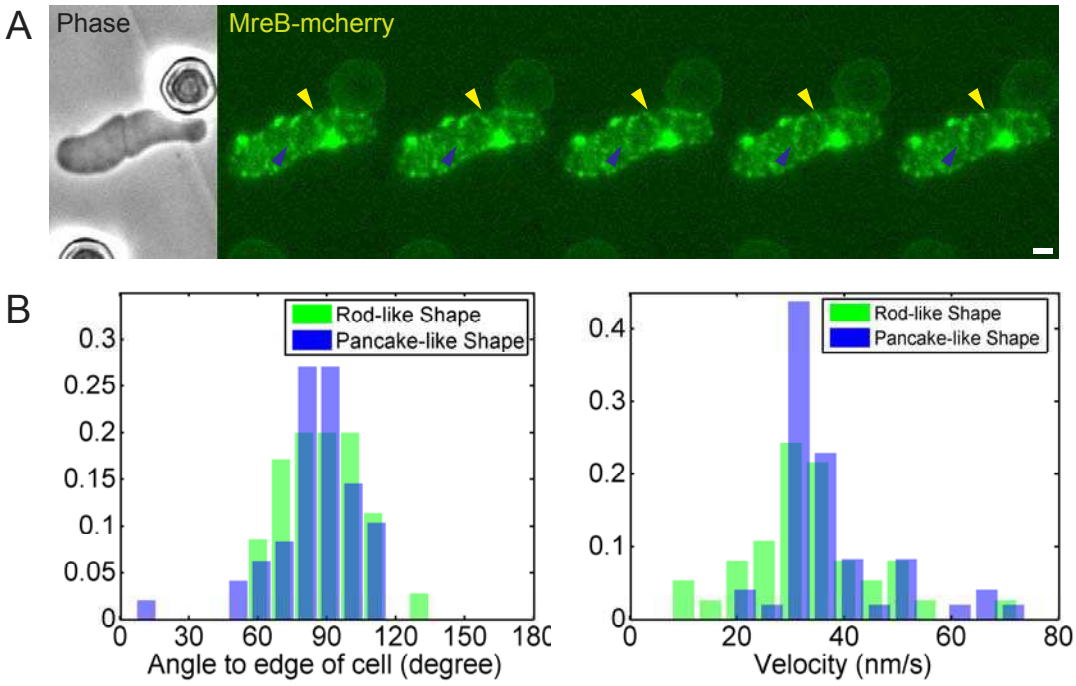

Figure 3.17: MreB motion in compressed cells. (**A**) Fluorescent spots of MreB-mcherry are moving perpendicular to cell periphery. (Fault color was used for better contrast of images) (**B**) Probability distribution of angle and velocities of MreB motion. Here the angle was defined by the direction of MreB motion with respect to the nearest cell periphery. (n=48 and 37 for compressed and normal cells, respectively) (Scale bar = 2μm)

3.8 Quantitative measure of cell wall growth rates

In addition to cell wall synthesis, MreB also play a mechanical role in *E. coli* cells [20, 28]. It has been suggested that MreB helps to suppress a shape instability in growing rod-like bacteria. To further investigate the mechanical role of MreB, we examined the rate of shape change of *E. coli* cells under compression with normal and partly depolymerized MreB. In particular, we are interested in changes in the radius of cell wall curvature. In normal rod-like cells, the cell radius does not change and elongation of the cell is controlled by metabolic and replication activity in the cell. Under mechanical compression, the cell wall radius of curvature presumably changes, and should also depend on mechanical factors. We investigate this in cells with MreB and in cells treated with A22, which partially disassemble MreB.

3.8.1 Change of radius of curvature of cell wall with MreB

For cells with MreB under compression, the shape was identified as the fluorescent periphery labeled with WGA488. The radius of curvature, R, was found by fitting a circular arc to a section of cell wall image (Fig. 3.18A). The change rates of R ($\mathrm{d}R/\mathrm{d}t$) were calculated and plotted against the ROC. Interestingly, for compressed cells with

MreB, $\mathrm{d}R/\mathrm{d}t$ decreases when R increases and reaches negative values around a radius of 2μm. The positive values of $\mathrm{d}R/\mathrm{d}t$ at small radius indicate that the bent cell wall tends to straighten, while the negative values at large R suggest a relatively straight cell wall tends to bend as the cell wall grows (Fig. 3.18B). Furthermore, there exists an intersection point at radius around 2um where $\mathrm{d}R/\mathrm{d}t$ equals to zero. The vanished $\mathrm{d}R/\mathrm{d}t$ manifests that a stable ROC exists when cells are subjected to mechanical perturbation.

3.8.2 Mathematical model of bacterial growth

To quantitatively explain the rate of change of R, we employed a biophysical model considered previously [33]. The model describes the relationship between local cell wall growth velocity and the cell wall mechanochemical energy as:

$$\frac{\mathrm{d}R}{\mathrm{d}t} \propto -\gamma \frac{\partial G}{\partial R} \tag{3.1}$$

where R is the cell radius specifying the current cell shape, G is the cell wall energy [33] and γ is a constant proportional to the cell wall synthesis rate. γ does not depend on cell wall geometry, and therefore scales the overall rate of cell wall change. The cell wall energy G can be calculated as

$$G = U - PV - \epsilon A \tag{3.2}$$

where U is the mechanical deformation energy of the cell wall, PV is the work done by the current turgor pressure (P), V is the current cell volume, and ϵA is

the chemical free energy change of adding new cell wall (ϵ can be thought of as the chemical bond energy per unit surface area of the cell wall). For compressed cells after long-term growth, the cell becomes as two layers of flat cell wall on top and bottom together with a lateral cell wall $0.8-0.9\mu m$ in height. Since the cell can only expand horizontally outward, cell growth can be described as the two-dimensional expansion of top and bottom layer of cell wall plus the lateral wall. Locally, the cell wall therefore can be approximated by a cylinder with height $h = 0.8 - 0.9\mu m$ and cross-sectional area proportional to R. We can apply Eq. 3.1 for the growth of this flatten cylinder. For irregular cell shapes, the local curvature R varies. However, local cell wall growth is still well approximated by growth equations for a section of cell wall with local radius R. Thus, we use Eq. 3.1 to estimate local cell growth rate.

To obtain the total cell wall energy G, we first calculated the strain energy stored in the top and bottom flat layers. Due to symmetry of the flatten cylinder, the displacement in the layer in polar coordinates (r, θ) can be given as

$$u_r = u_r(r),\ v_\theta = 0 \tag{3.3}$$

The elastic strains are

$$\varepsilon_r = \frac{\mathrm{d}u_r}{\mathrm{d}r},\ \varepsilon_\theta = \frac{u_r}{r},\ \gamma_{r\theta} = 0 \tag{3.4}$$

The stresses are

$$\begin{aligned} \sigma_r &= \tfrac{E}{1-\nu^2}\left(\tfrac{\mathrm{d}u_r}{\mathrm{d}r} + \nu\tfrac{u_r}{r}\right) \\ \sigma_\theta &= \tfrac{E}{1-\nu^2}\left(\tfrac{u_r}{r} + \nu\tfrac{\mathrm{d}u_r}{\mathrm{d}r}\right) \\ \tau_{r\theta} &= 0 \end{aligned} \tag{3.5}$$

where E and are the Youngs modulus and Poisson ratio of cell wall, respectively. The Mechanical equilibrium reads

$$\frac{\mathrm{d}\sigma_r}{\mathrm{d}r} + \frac{\sigma_r - \sigma_\theta}{r} = 0 \tag{3.6}$$

Substituting Eq. 3.5 into Eq. 3.6 leads to

$$\frac{\mathrm{d}^2 u_r}{\mathrm{d}r^2} + \frac{1}{r}\frac{\mathrm{d}u_r}{\mathrm{d}r} - \frac{u_r}{r^2} = 0 \tag{3.7}$$

The solution of Eq. 3.7 is

$$u_r = C_1 r + \frac{C_2}{r} \tag{3.8}$$

where $C_2 = 0$ due to the finite displacement at $r = 0$. At $r = R$, we have $\sigma_r = Ph/(2d)$, where h is the height of the micropillars, equal to the height of the flattened cell cylinder. d is the thickness of the cell wall layer. Then we get

$$C_1 = \frac{Ph(1-\nu)}{2Ed} \tag{3.9}$$

So we have

$$\sigma_r = \sigma_\theta = \frac{Ph}{2d},\ \varepsilon_r = \varepsilon_\theta = \frac{Ph(1-\nu)}{2Ed} \tag{3.10}$$

The strain energy in the two flat layers is

$$U_1 = 2\pi \int_0^R (\sigma_r \varepsilon_r + \sigma_\theta \varepsilon_\theta) r \mathrm{d}r = \frac{2\pi P^2 h^2 R^2 (1-\nu)}{2Ed^2} \tag{3.11}$$

The stress and strain in the lateral cell wall are

$$\sigma_\theta = \frac{PR}{d},\ \varepsilon_\theta = \frac{PR}{Ed} \tag{3.12}$$

The strain energy in the lateral cell wall is

$$U_2 = \frac{\pi P^2 h R^3}{E d^2} \tag{3.13}$$

Therefore, the total strain energy becomes

$$U = U_1 + U_2 = \frac{\pi P^2 h R^3}{E d^2} + \frac{2\pi P^2 h^2 (1-\nu) R^2}{2 E d^2} \tag{3.14}$$

The total energy is

$$G = U - PV - \epsilon A \tag{3.15}$$

where $PV = \pi P h R^2$ is the work done by turgor pressure and V is the cell volume and ϵA is the chemical energy. ϵ is the released energy per unit area and $A = 2\pi R^2 + 2\pi h R$ is the surface area of cell wall. So we have

$$G = \frac{\pi P^2 h R^3}{E d^2} + \left[\frac{2\pi P^2 h^2 (1-\nu)}{2 E d^2} - \pi P h - 2\pi\epsilon\right] R^2 - 2\pi h R \tag{3.16}$$

Hence, Eq. 3.1 can be expressed as

$$\begin{aligned} \tfrac{\mathrm{d}R}{\mathrm{d}t} &\propto -\gamma \left\{ \tfrac{3\pi P^2 h R^2}{E d^2} + \left[\tfrac{2\pi P^2 h^2 (1-\nu)}{E d^2} - 2\pi P h - 4\pi\epsilon\right] R - 2\pi h \right\} \\ &\propto -\gamma (3 C R^2 + 2 B R - 2\pi h) \end{aligned} \tag{3.17}$$

where $C = \frac{\pi P^2 h}{E d^2}$ and $B = \frac{\pi P^2 h^2 (1-\nu)}{E d^2} - \pi P h - 2\pi\epsilon$. Therefore, C and B have complex dependence on cell wall stiffness, cell height, wall thickness and turgor pressure.

In a growing cell, parameters C and B are expected to vary with space and time, due to complexities of the cell wall structure and possible mechanical contributions from other structures such as MreB. For example, if MreB applies any active forces on the cell wall, then the local Young's modulus would change. However, scaling

with respect to geometric parameters such as R should remain the same. Specifically, if we compare growth dynamics with and without MreB, it is possible to resolve mechanical contribution of MreB to cell wall growth. We find that MreB changes relative magnitudes of C and B, therefore indicating that MreB is contributing a mechanical role for cell wall growth.

Note that the parameters in the model such as the cell wall Young's modulus, turgor pressure, chemical energy ϵ, are all potentially controlled by the cell, and may vary in time as the cell is being compressed. The modulus will also depend on whether there are additional mechanical reinforcements from MreB. Therefore, the parameter C should depend on cell wall properties, and possibly forces from MreB, and is not known. Parameter B depends on the effective turgor pressure and is also not known. However, the scaling relationship with respect to the cell radius of curvature, i.e., $\mathrm{d}R/\mathrm{d}t$ proportional to R^2, should remain valid. By substituting all parameters measured or estimated (Table 3.1), within the range of $R = 1 - 3\mu$m, $\mathrm{d}R/\mathrm{d}t$ decreases when R increases, and $\mathrm{d}R/\mathrm{d}t$ reaches zeros at $R \approx 2\mu$m, agreeing well with our experimental results in Fig. 3.18B.

3.8.3 Change of radius of curvature of cell wall without MreB

Treating *E. coli* cells with A22 would partially inhibit MreB polymerization [82] and reduce any mechanical forces from MreB. In our experiment, a moderate concentration of A22 (20μg/ml) was added, and cells were then compressed and similarly grew into a pancake-like shape. The rates of R change were also measured, and we also found that $\mathrm{d}R/\mathrm{d}t$ decreased as R increases (Fig. 3.18B). However, the quantitative results are different from the cells with intact MreB: $\mathrm{d}R/\mathrm{d}t$ reaches zeros at larger values of R (Fig. 3.18B). This indicates that the cell wall prefers to relax to a straighter configuration when MreB is disassembled. We know that in rod-shaped cells, MreB is functioning to maintain the rod-like shape, preventing cell wall from bulging. And for compressed cells with irregular shape observed here, MreB also functions to restrict the overall cell size, preventing cells from over-expansion, in line with our model. According to Eq. 3.17, when MreB was inhibited, both C and B are changed. If MreB only affects PG synthesis rates, then the magnitude of $\mathrm{d}R/\mathrm{d}t$ would change, but not the scaling with respect to R. Therefore, MreB must have a mechanical influence during cell growth, and within the framework of our model, results are consistent with the interpretation that MreB changes mechanical stiffness of the cell wall. This was proven by substituting all parameters (Table 3.1) into our model. The best fit for A22- data corresponds to Young's modulus of cell wall about

40MPa compared to 20MPa for A22+ data, whereas the cell wall synthesis rate for A22- data is about 6 times higher than that of A22+ (Fig. 3.18B). Therefore, MreB likely serves a mechanical role during cell wall growth. In addition, it was found recent MreB preferentially binds to regions of negative curvature [29], which also suggests an active role for MreB.

Note that as compression continues, the cell may change cell properties associated with variables C and B. Therefore the stable radius can vary with time. Therefore, to make a consistent comparison between cells with and without A22 addition, the data in Fig. 3.18 are collected at the same time point after 15min of compression.

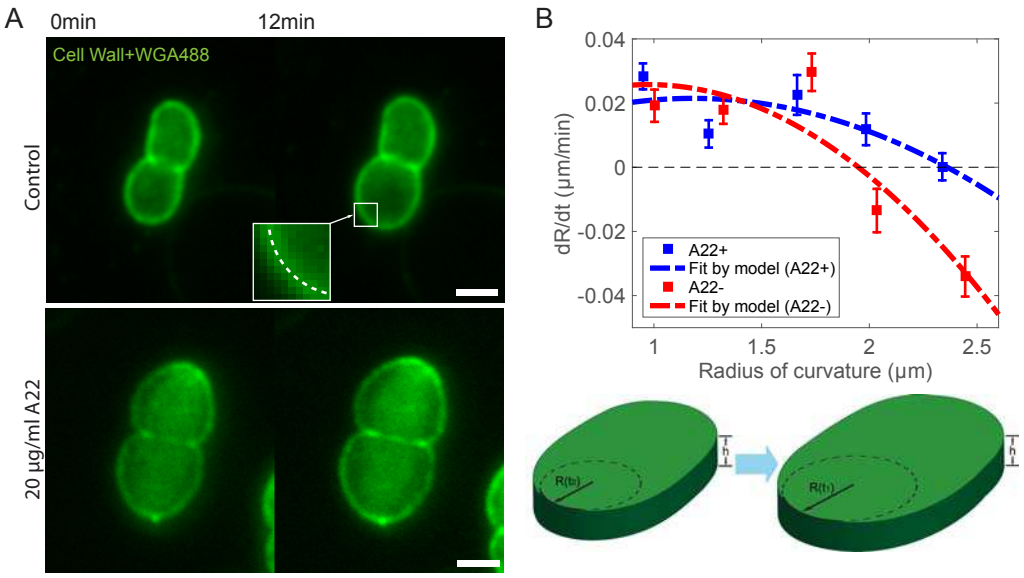

Figure 3.18: The rate of change of the local cell wall radius of curvature (ROC). (**A**) Cells with MreB polymerization inhibited by A22 have different expansion rates under compression. Local radius of cell periphery was measured by fitting a circle (upper, inset) to the cropped arc for both control (upper panel) and cells with 20μg/ml A22 (lower panel). (**B**) Upper: the rates of local ROC change, dR/dt, are plotted against local radii for both control (compressed) and cells with 20μg/ml A22. Experimental data are fitted by model predictions (dashed curves, Eq. 3.17). Cells in the presence of A22 show a different scaling with respect to R. (n$\geq$20 for each point. Error bars indicate standard error of the mean.) The fitted Young's moduli of cell wall are 40MPa and 20MPa for A22- and A22+, respectively, and synthesis rates of cell wall are 1.3×10^{-5} and 0.2×10^{-5} for A22- and A22+, respectively. ALl others parameters were used as in Table 3.1. Lower: 3D cartoons showing the local ROC changing as cells expands under compression (case of dR/d$t>0$). (Scale bars, 2μm)

Constant parameters	Description	Value for A22-	Value for A22+	Unit
d	Height of chamber	0.8	0.8	μm
h	Thickness of cell wall	10*	10*	nm
ν	Poisson's ratio of cell wall	0.3*	0.3*	
Fitted parameters	**Description**	**Value for A22-**	**Value for A22+**	**Unit**
ϵ	Chemical energy released per unit area	22	48	$J{\cdot}m^{-2}$
γ	Constant proportional to the cell wall synthesis rate	3.2×10^{-6}	1.0×10^{-6}	
E	Young's modulus of cell wall	22	14	MPa
P	Turgor pressure	1.4×10^{5}	1.6×10^{5}	Pa

Table 3.1: Parameters used in the model

$*$ estimated from reference

3.9 Discussion

In this chapter, we investigate bacterial cell growth dynamics under mechanical compression. We find that *E. coli* cells no longer maintain their rod-like shapes when subjected to compression, and gradually develop into irregular pancake-like shape. On short time scales, the deformation would dramatically alter the distribution of the mechanical stress in cell wall. Our finite element simulation shows that the stress would concentrate at the periphery of flattened cell (Fig. 3.19). Such stress concentration could create many defects in the cell wall, which could be seen in the cells whose cell wall is not expanding continuously but discretely or even with inner membrane bubbled out (Fig. 3.20). These defects locate with higher density at the side wall of the compressed cells than normal cells, leaving a lot of new bind sites for insertion of new glycan chains [33]. This leads to the cell expansion happens not necessarily along the cell axis but uniformly along the whole periphery. We also show that the physiological processes of cells are largely undisturbed by external force and the protein and DNA synthesis is progressing normally in these compressed cells. Moreover, the mechanical compression influences bacterial growth in different ways from hydrostatic pressure [83]. Bacterial cells likely adapt widely range of hydrostatic pressure by adjusting turgor pressure through actively pumping. However, under large compression, over-stretching or compressing of chromosome and protein macromolecules could totally arrest cell growth (micropillar height $< 0.5\mu m$ in Fig. 3.6).

On longer time scales, the sudden stress change in the cell wall is relieved by

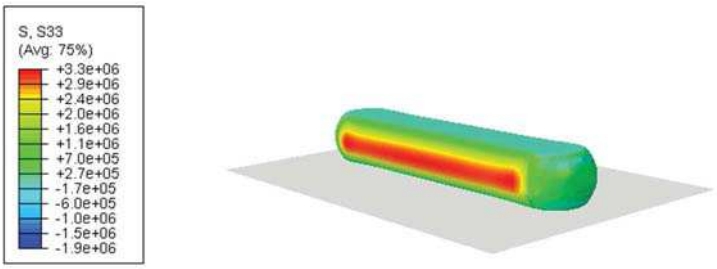

Figure 3.19: Finite element simulation of an *E.coli* cell compressed by PDMS layer. Tensile stress (Pa) is concentrated at the lateral wall of the flattened cell.

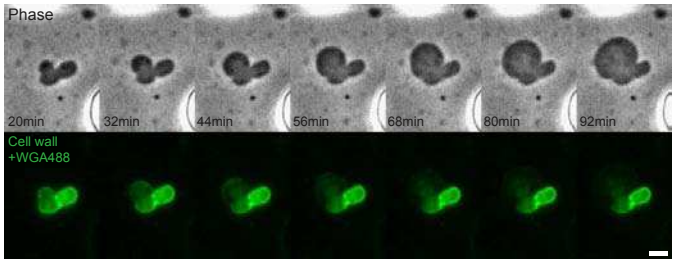

Figure 3.20: Cells can lyse and develop blebs when compressed. (Scale bar = 2μm)

new cell wall growth. This type of plastic deformation due to growth under external force has been discussed before. The subsequent growth dynamics, according to the mechanochemical model, should depend on the current geometry of the cell. Indeed, we find that under compression, the long term growth dynamics depends on the local curvature of the cell wall, and quantitative results are consistent with scaling results based on a mechanochemical model proposed previously.

In compressed cells, we find that MreB is still functioning normally and catalyzing cell wall growth. MreB is co-localized with newly inserted cell wall in compressed cells, similar to what was found in rod-shaped cell [29]. Therefore, MreB movement and

function in cell wall synthesis are robust, regardless of the cell shape. In addition, we found that the presence of MreB alters the scaling of growth dynamics with respect to the local curvature. If MreB's role is entirely biochemical, then the rate of cell wall growth described by the parameter γ in Eq. 3.1 would change, but the scaling with respect to cell wall geometry should not change. Instead, we found that MreB alters the growth rate as a function of cell wall curvature, implying that MreB affects relative magnitudes of parameters such as C and B in Eq. 3.17. These parameters depend on the local cell wall stiffness and internal pressure. Therefore, this result is convincing evidence that MreB not only biochemically catalyzes PG insertion, but also alters mechanical environment of the cell, possibly by changing the cell wall stiffness or internal cell wall pressure.

We also find that there exists an upper limit in cell size when bacterial cells are under compression. Our experiment and theoretical model showed that there may exist a stable local radius at which PG synthesis is in a dynamic equilibrium. However, this stable radius depends on local cell wall mechanical properties and any other forces acting on the cell wall. Given that the cell wall may be heterogeneous with spatially varying defects, a fixed stable radius is likely difficult to resolve. Nevertheless, our work, together with other experiments on cell wall growth dynamics under external forces, show that mechanical forces do influence cell wall growth dynamics and geometry of the cell wall in bacteria. MreB alters mechanical forces on the cell wall or mechanical stiffness of the cell wall. In addition, the mechanochemical pic-

ture should be valid in any living biomaterial with active growth and turnover. Our experimental approach can be extended to examine other situations as well.

Bibliography

[1] A. Briegel, X. X. Li, A. M. Bilwes, K. T. Hughes, G. J. Jensen, and B. R. Crane, "Bacterial chemoreceptor arrays are hexagonally packed trimers of receptor dimers networked by rings of kinase and coupling proteins." *Proc. Natl. Acad. Sci. U. S. A.*, vol. 109, pp. 3766–3771, 2012.

[2] D. M. Raskin and P. A. de Boer, "Rapid pole-to-pole oscillation of a protein required for directing division to the middle of it Escherichia coli." *Proc. Natl. Acad. Sci. USA*, vol. 96, pp. 4971–4976, 1999.

[3] M. T. Cabeen and C. Jacobs-Wagner, "Bacterial cell shape." *Nat. Rev. Microbiol.*, vol. 3, pp. 601–610, 2005.

[4] Y. Chen and H. P. Erickson, "Ftsz filament dynamics at steady state: subunit exchange with and without nucleotide hydrolysis." *Biochemistry*, vol. 48, pp. 6664–6673, 2009.

[5] F. Bi and J. Lutkenhaus, "Ftsz ring structure associated with division in *escherichia coli*." *Nature*, vol. 354, pp. 161–164, 1991.

[6] S. Pichoff and J. Lutkenhaus, "Unique and overlapping roles for zipa and ftsa in septal ring assembly in *escherichia coli*." *EMBO J.*, vol. 21, pp. 685–693, 2002.

[7] M. Osawa, D. E. Anderson, and H. P. Erickson, "Curved ftsz protofilaments generate bending forces on liposome membranes." *EMBO J.*, vol. 28, pp. 3476–3484, 2009.

[8] G. H. Lan, B. R. Daniels, T. M. Dobrowsky, D. Wirtz, and S. X. Sun, "Condensation of ftsz filaments can drive bacterial cell division." *Proc. Natl. Acad. Sci. U. S. A.*, vol. 106, pp. 121–126, 2009.

[9] J. Stricker, P. Maddox, E. D. Salmon, and H. P. Erickson, "Rapid assembly dynamics of the *escherichia coli* ftsz-ring demonstrated by fluorescence recovery after photobleaching." *Proc. Natl. Acad. Sci. USA.*, vol. 99, pp. 3171–3175, 2002.

[10] M. Osawa, D. E. Anderson, and H. P. Erickson, "Reconstitution of contractile ftsz rings in liposomes." *Science*, vol. 320, pp. 792–794, 2008.

[11] Z. Li, M. J. Trimble, Y. V. Brun, and G. J. Jensen, "The structure of ftsz filaments *in vivo* suggests a force-generating role in cell division." *EMBO J.*, vol. 26, pp. 4694–4708, 2007.

[12] B. Zuber, M. Haenni, T. Ribeiro, K. Minnig, F. Lopes, P. Moreillon, and J. Dubochet, "Granular layer in the periplasmic space of gram-positive bacteria and fine structures of enterococcus gallinarum and streptococcus gordonii septa revealed

by cryo-electron microscopy of vitreous sections." *J. Bacteriol.*, vol. 188, pp. 6652–6660, 2006.

[13] G. Fu, H. Tao, J. Buss, C. Coltharp, Z. Hensel, and J. Xiao, "*In vivo* structure of the *e. coli* ftsz-ring revealed by photoactivated localization microscopy (palm)." *PLoS One*, vol. 5, p. e12068, 2010.

[14] P. C. Jennings, G. C. Cox, L. G. Monahan, and E. J. Harry, "Super-resolution imaging of the bacterial cytokinetic protein ftsz." *Micron*, vol. 42, pp. 336–341, 2011.

[15] M. P. Strauss, A. T. F. Liew, L. Turnbull, C. B. Whitchurch, L. G. Monahan, and E. J. Harry, "3d-sim super-resolution microscopy reveals a bead-like arrangement for ftsz and the division machinery, implications for triggering cytokinesis." *PLoS Biol.*, vol. 10, p. e1001389, 2012.

[16] K. D. Young, "The selective value of bacterial shape." *Microbiol Mol. Biol. Rev.*, vol. 70, pp. 660–703, 2006.

[17] X. Yao, M. Jericho, D. Pink, and T. Beveridge, "Thickness and elasticity of gram-negative murein sacculi measured by atomic force microscopy." *J. Bacteriol.*, vol. 181, pp. 6865–6875, 1999.

[18] W. Vollmer and J. V. Holtje, "Morphogenesis of *escherichia coli*." *Curr. Opin. Microbiol.*, vol. 4, pp. 625–633, 2001.

[19] S. X. Sun and H. Jiang, "Physics of bacterial morphogenesis." *Microbiol. Mol. Biol. Rev.*, vol. 75, pp. 543–565, 2011.

[20] H. Y. Jiang, F. W. Si, W. Margolin, and S. X. Sun, "Mechanical control of bacterial cell shape." *Biophys. J.*, vol. 101, pp. 327–335, 2011.

[21] F. Chang and K. C. Huang, "How and why cells grow as rods." *BMC Biol.*, vol. 12, p. 54, 2014.

[22] R. A. Daniel and J. Errington, "Control of cell morphogenesis in bacteria: two distinct ways to make a rod-shaped cell." *Cell*, vol. 113, pp. 767–776, 2003.

[23] A. Typas, M. Banzhaf, C. A. Gross, and W. Vollmer, "From the regulation of peptidoglycan synthesis to bacterial growth and morphology." *Nat. Rev. Microbiol.*, vol. 10, pp. 123–136, 2012.

[24] A. L. Koch, "Biophysics of bacterial walls viewed as stress-bearing fabric." *Microbiol. Rev.*, vol. 52, pp. 337–353, 1988.

[25] Z. Gitai, N. Dye, and L. Shapiro, "An actin-like gene can determine cell polarity in bacteria." *Proc. Natl. Acad. Sci. USA*, vol. 101, pp. 8643–8648, 2004.

[26] T. Kruse, J. Bork-Jensen, and K. Gerdes, "The morphogenetic mrebcd proteins of *escherichia coli* form an essential membrane-bound complex." *Mol. Microbiol.*, vol. 55, pp. 78–89, 2005.

[27] Z. Gitai, N. A. Dye, A. Reisenauer, M. Wachi, and L. Shapiro, "Mreb actin-mediated segregation of a specific region of a bacterial chromosome." *Cell*, vol. 120, pp. 329–341, 2005.

[28] S. Wang, H. Arellano-Santoyo, P. A. Combs, and J. W. Shaevitz, "Actin-like cytoskeleton filaments contribute to cell mechanics in bacteria." *Proc. Natl. Acad. Sci. USA*, vol. 107, pp. 9182–9185, 2010.

[29] T. S. Ursell, J. Nguyen, R. D. Monds, A. Colavin, G. Billings, N. Ouzounov, Z. Gitai, J. W. Shaevitz, and K. C. Huang, "Rod-like bacterial shape is maintained by feedback between cell curvature and cytoskeletal localization." *Proc. Natl. Acad. Sci. USA*, vol. 111, pp. E1025–E1034, 2014.

[30] S. van Teeffelen, S. Wang, L. Furchtgott, K. C. Huang, N. S. Wingreen, J. W. Shaevitz, and Z. Gitai, "The bacterial actin mreb rotates, and rotation depends on cell-wall assembly." *Proc. Natl. Acad. Sci. USA*, vol. 108, pp. 15 822–15 827, 2011.

[31] H. H. Tuson, G. K. Auer, L. D. Renner, M. Hasebe, C. Tropini, M. Salick, W. C. Crone, A. Gopinathan, K. C. Huang, and D. B. Weibel, "Measuring the stiffness of bacterial cells from growth rates in hydrogels of tunable elasticity." *Mol. Microbiol.*, vol. 84, pp. 874–891, 2012.

[32] A. Amir and S. van Teeffelen, "Getting into shape: how do rod-like bacteria control their geometry?" *Syst. Synth. Biol.*, vol. 8, pp. 227–235, 2014.

[33] H. Y. Jiang and S. X. Sun, "Morphology, growth, and size limit of bacterial cells." *Phys. Rev. Lett.*, vol. 105, p. 028101, 2010.

[34] S. Takeuchi, W. R. DiLuzio, D. B. Weibel, and G. M. Whitesides, "Controlling the shape of filamentous cells of *escherichia coli*." *Nano Lett.*, vol. 5, pp. 1819–1823, 2005.

[35] J. Männik, R. Driessen, P. Galajda, J. E. Keymer, and C. Dekker, "Bacterial growth and motility in sub-micron constrictions." *Proc. Natl. Acad. Sci. USA*, vol. 106, pp. 14 861–14 866, 2009.

[36] O. Sliusarenko, M. T. Cabeen, C. W. Wolgemuth, C. Jacobs-Wagner, and T. Emonet, "Processivity of peptidoglycan synthesis provides a built-in mechanism for the robustness of straight-rod cell morphology." *Proc. Natl. Acad. Sci. USA*, vol. 107, pp. 10 086–10 091, 2010.

[37] P. Wang, L. Robert, J. Pelletier, W. L. Dang, F. Taddei, A. Wright, and S. Jun, "Robust growth of *escherichia coli*." *Curr. Biol.*, vol. 20, pp. 1099–1103, 2010.

[38] A. Amir, F. Babaeipour, D. B. Mclntosh, D. R. Nelson, and S. Jun, "Bending forces plastically deform growing bacterial cell walls." *Proc. Natl. Acad. Sci. USA*, vol. 111, pp. 5778–5783, 2014.

[39] S. Inoue, O. Shimomura, M. Goda, M. Shribak, and P. T. Tran., "Fluorescence

polarization of green fluorescence protein." *Proc. Natl. Acad. Sci. USA.*, vol. 99, no. 1, pp. 4272–4277, 2002.

[40] J. Lakowicz, "Principles of fluorescence spectroscopy [third edition]," *Springer Science+Business Media, LLC, New York*, p. 954, 2006.

[41] C. Picart and D. E. Discher, "Actin protofilament orientation at the erythrocyte membrane." *Biophys. J.*, vol. 77, pp. 865–878, 1999.

[42] A. L. Mattheyses, M. Kampmann, C. E. Atkinson, and S. M. Simon, "Fluorescence anisotropy reveals order and disorder of protein domains in the nuclear pore complex." *Biophys. J.*, vol. 99, pp. 1706–1717, 2010.

[43] A. M. Vrabioiu and T. J. Mitchison, "Structural insights into yeast septin organization from polarized fluorescence microscopy." *Nature*, vol. 443, pp. 466–469, 2006.

[44] Q. Sun and W. Margolin, "Ftsz dynamics during the division cycle of live *escherichia coli* cells," *J. Bacteriol.*, vol. 180, pp. 2050–2056, 1998.

[45] R. Johnson and B. Ely, "Isolation of spontaneously derived mutants of *caulobacter crescentus*." *Genetics*, vol. 86, pp. 25–32, 1977.

[46] D. J. Ferullo, D. L. Cooper, H. R. Moore, and S. T. Lovett, "Cell cycle synchronization of *escherichia coli* using the stringent response, with fluorescence labeling assays for dna content and replication." *Methods*, vol. 48, pp. 8–13, 2009.

[47] M. Kampmann, C. E. Atkinson, A. L. Mattheyses, and S. M. Simon, "Mapping the orientation of nuclear pore proteins in living cells with polarized fluorescence microscopy." *Nat. Struct. Biol.*, vol. 18, pp. 643–649, 2011.

[48] C. R. Desper and I. Kmura, "Mathematics of the polarized fluorescence experiment." *J. Appl. Phys.*, vol. 88, pp. 4225–4233, 1967.

[49] A. Volkmer, V. Subramaniam, D. J. S. Birch, , and T. M. Jovin, "One- and two-photon excited fluorescence lifetimes and anisotropy decays of green fluorescent proteins." *Biophys. J.*, vol. 78, pp. 1589–1598, 2000.

[50] B. Richards and E. Wolf, "Electromagnetic diffraction in optical systems 2. structure of the image field in an aplanatic system." *Proc. R. Soc. London A*, vol. 253, pp. 358–379, 1959.

[51] T. Ha, T. A. Laurence, D. S. Chemla, and S. Weiss, "Polarization spectroscopy of single fluorescent molecules." *J. Phys. Chem. B*, vol. 103, pp. 6839–6950, 1999.

[52] X. H. Shi, J. Basran., H. E. Seward, W. Childs, C. R. Bagshaw, and S. G. Boxer, "Anomalous negative fluorescence anisotropy in yellow fluorescent protein (yfp 10c): Quantitative analysis of fret in yfp dimers." *Biochemistry*, vol. 46, pp. 14 403–14 417, 2007.

[53] D. E. Andersen, F. J. Gueiros-Filho, and H. P. Erickson, "Assembly dynamics

of ftsz rings in *bacillus subtilis* and *escherichia coli* and effects of ftsz-regulating proteins." *J. Bacteriol.*, vol. 186, pp. 5775–5781, 2004.

[54] H. P. Erickson, D. E. Anderson, and M. Osawa, "Ftsz in bacterial cytokinesis: cytoskeleton and force generator all in one." *Microbiol. Rev.*, vol. 74, pp. 504–528, 2010.

[55] K. Katoh, K. Hammar, P. J. Smith, and R. Oldenbourg, "Birefringence imaging directly reveals architectural dynamics of filamentous actin in living growth cones." *Mol. Biol. Cell.*, vol. 10, no. 1, p. 197210, 1999.

[56] S. Pichoff and J. Lutkenhaus, "Tethering the z ring to the membrane through a conserved membrane targeting sequence in ftsa." *Mol. Microbiol.*, vol. 55, pp. 1722–1734, 2005.

[57] B. Geissler, D. Shiomi, and W. Margolin, "The $ftsA*$ gain-of-function allele of *escherichia coli* and its effects on the stability and dynamics of the z ring." *Microbiology*, vol. 153, pp. 814–825, 2007.

[58] E. Fischer-Friedrich and N. Gov, "Modeling ftsz ring formation in the bacterial cell-anisotropic aggregation via mutual interactions of polymer rods." *Phys. Biol.*, vol. 8, p. 026007, 2011.

[59] R. Tsukanov, G. Reshes, G. Carmon, E. Fischer-Friedrich, N. S. Gov, I. Fishov,

and M. Feingold, "Timing of z-ring localization in *escherichia coli*." *Phys. Biol.*, vol. 8, p. 066003, 2011.

[60] S. Arumugam., G. Chwastek, E. Fischer-Friedrich, C. Ehrig, I. Moench, and P. Schwille, "Surface topology engineering of membranes for the mechanical investigation of the tubulin homologue ftsz." *Angew. Chem. Int. Edit.*, vol. 51, pp. 11 858–11 862, 2012.

[61] E. Fischer-Friedrich, B. M. Friedrich, and N. Gov, "Ftsz rings and helices: physical mechanisms for the dynamic alignment of biopolymers in rod-shaped bacteria." *Phys. Biol.*, vol. 9, p. 016009, 2012.

[62] S. Thanedar and W. Margolin, "Ftsz exhibits rapid movement and oscillation waves in helix-like patterns in *escherichia coli*." *Curr. Biol.*, vol. 14, pp. 1167–1173, 2004.

[63] L. Niu and J. Yu, "Investigating intracellular dynamics of ftsz cytoskeleton with photoactivation single-molecule tracking." *Biophys. J.*, vol. 95, pp. 2009–2016, 2008.

[64] P. Vats, Y. Shih, and L. Rothfield, "Assembly of the mreb-associated cytoskeletal ring of *escherichia coli*." *Mol. Microbiol.*, vol. 72, pp. 170–182, 2009.

[65] E. Garner, R. Bernard, W. Q. Wang, X. W. Zhuang, D. Z. Rudner, and T. Mitchi-

son, "Coupled, circumferential motions of the cell wall synthesis machinery and mreb filaments in *b. subtilis*." *Science*, vol. 333, pp. 222–225, 2011.

[66] J. Dominguez-Escobar, A. Chastanet, A. H. Crevenna, V. Fromion, R. Wedlich-Soeldner, and R. Carballido-Lopez, "Processive movement of mreb-associated cell wall biosynthetic complexes in bacteria." *Science*, vol. 333, pp. 225–228, 2011.

[67] R. Mercier, Y. Kawai, and J. Errington, "Excess membrane synthesis drives a primitive mode of cell proliferation." *Cell*, vol. 152, pp. 97–1007, 2013.

[68] M. Leaver, P. Dominguez-Cuevas, J. M. Coxhead, R. A. Daniel, and J. Errington, "Life without a wall or division machine in *bacillus subtilis*." *Nature*, vol. 457, pp. 849–853, 2009.

[69] T. Thorsen, S. J. Maerkl, and S. R. Quake, "Microfluidic large-scale integration." *Science*, vol. 298, pp. 580–584, 2001.

[70] S. Hosmane, A. Fournier, R. Wright, L. Rajbhandari, R. Siddique, I. Yang, K. Ramesh, A. Venkatesan, and N. Thakor, "Valve-based microfluidic compression platform: single axon injury and regrowth." *Lab Chip*, vol. 11, pp. 3888–3895, 2011.

[71] D. Huh, B. D. Matthews, A. Mammoto, M. Montoya-Zavala, H. Y. Hsin, and

D. E. Ingber, "Reconstituting organ-level lung functions on a chip." *Science*, vol. 328, pp. 1662–1668, 2010.

[72] J. J. Thwaites and N. H. Mendelson, "Mechanical behaviour of bacterial cell walls." *Adv. Microb. Physiol.*, vol. 32, pp. 173–222, 1991.

[73] F. O. Bendez, C. A. Hale, T. G. Bernhardt, and P. A. J. de Boer, "Rodz (yfga) is required for proper assembly of the mreb actin cytoskeleton and cell shape in it E. coli." *EMBO J.*, vol. 28, pp. 193–204, 2009.

[74] A. Ishii, T. Sato, M. Wachi, and K. Nagai, "Effects of high hydrostatic pressure on bacterial cytoskeleton ftsz polymers *in vivo* and *in vitro*." *Microbiol.*, vol. 150, pp. 1965–1972, 2004.

[75] G. W. Niven, C. A. Miles, and B. M. Macke, "The effects of hydrostatic pressure on ribosome conformation in *escherichia coli*: an *in vivo* study using differential scanning calorimetry." *Microbial.*, vol. 145, pp. 419–425, 1999.

[76] Z. Hu, A. Mukherjee, S. Pichoff, and J. Lutkenhaus, "The minc component of the division site selection system in *escherichia coli* interacts with ftsz to prevent polymerization." *Proc. Natl. Acad. Sci. USA*, vol. 96, pp. 14 819–14 824, 1999.

[77] C. L. Woldringh, E. Mulder, J. A. Valkenburg, F. B. Wientjes, A. Zaritsky, and N. Nanninga, "Role of the nucleoid in the toporegulation of division." *Res. Microbiol.*, vol. 141, pp. 39–49, 1990.

[78] S. Taheri-Araghi, S. Bradde, J. T. Sauls, N. S. Hill, P. A. Levin, J. Paulsson, M. Vergassola, and S. Jun, "Cell-size control and homeostasis in bacteria." *Curr. Biol.*, vol. 25, pp. 385–391, 2015.

[79] M. Campos, I. V. Surovtsev, S. Kato, A. Paintdakhi, B. Beltran, S. E. Ebmeier, and C. Jacobs-Wagner, "A constant size extension drives bacterial cell size homeostasis." *Cell*, vol. 159, pp. 1433–1446, 2015.

[80] F. van den Ent, L. A. Amos, and J. Lowe, "Prokaryotic origin of the actin cytoskeleton." *Nature*, vol. 413, no. 1, pp. 39–44, 2001.

[81] R. Carballido-Lopez, "The bacterial actin-like cytoskeleton." *Microbiol. Mol. Biol. Rev.*, vol. 70, no. 1, pp. 888–909, 2006.

[82] G. J. Bean, S. T. Flickinger, W. M. Westler, M. E. McCully, D. Sept, D. B. Weibel, and K. J. Amann, "A22 disrupts the bacterial actin cytoskeleton by directly binding and inducing a low-affinity state in mreb." *Biochemistry*, vol. 48, no. 1, pp. 4852–4857, 2009.

[83] P. Kumar and A. Libchaber, "Pressure and temperature dependence of growth and morphology of it Escherichia coli: Experiments and stochastic model." *Biophys. J.*, vol. 105, no. 1, pp. 783–793, 2013.

Curriculum Vitae

Fangwei Si

Education

Ph.D. 2015	Mechanical engineering, 2009-2015, Johns Hopkins University
B.S. 2009	Theoretical and applied mechanics, 2005-2009, Peking University

Research Interests

Biophysics of bacterial cell shape regulation, growth and division

Biophysics of mammalian cell shape regulation, migration and division

Quantitative experiment and modeling of bacterial and mammalian cell cycle

Microfluidics and light microscopy for single cell manipulation and imaging

Publications

Journal Papers	1. Yellin, F., **Si, F. W.** & Sun, S. X. Electromechanics and volume regulation in non-excitable cells. Manuscript in preparation. 2. Rochman N.*, **Si, F. W.*** & Sun, S. X. To grow is not enough: the impact of noise on cell environmental response and fitness. Under review.

3. Tao, J. X., He, L. J., **Si, F. W.**, Wirtz D. & Sun, S. X. Biomechanical regulation of cell membrane tension. *Biophys. J.* Under review.

4. Kim D. H.*, Li, B.*, **Si, F. W.***, Phillips, J. M., Wirtz D. & Sun, S. X. Volume regulation and shape bifurcation in the cell nucleus. *J. Cell Sci.* DOI: 10.1242/jcs.166330 (2015).

5. **Si, F. W.***, Li, B.*, Margolin, W. & Sun, S. X. Bacterial growth and form under mechanical compression. *Sci. Rep.* **5**, 11367; DOI: 10.1038/srep11367 (2015).

6. **Si, F. W.**, Busiek, K., Margolin, W. & Sun, S. X. Organization of FtsZ filaments in the bacterial division ring measured from polarized fluorescence microscopy. *Biophys. J.* **105,** 1976-1986 (2013).

7. Jiang, H. Y., **Si, F. W.**, Margolin, W. & Sun, S. X. Mechanical control of bacterial cell shape. *Biophys. J.* **101,** 327-335 (2011).

8. Zhang, K., **Si, F. W.**, Duan, H. L. & Wang, J. Microstructures and mechanical properties of silks of silkworm and honeybee. *Acta Biomater.* **6,** 2165-2171 (2010).

* co-first author

Conference Posters

1. Rochman N., **Si, F. W.** & Sun, S. X. To grow is not enough: the impact of cell response time on fitness. *59th Annual Meeting of the Biophysical-Society* (2015).

2. **Si, F. W.**, Li, B. & Sun, S. X. Bacterial growth and shape regulation by external compression. *59th Annual Meeting of the Biophysical-Society* (2015).

3. **Si, F. W.** & Sun, S. X. Polarized Fluorescence Microscopy Reveals Structural Transitions of FtsZ-Ring During Cell Division. *55th Annual Meeting of the Biophysical-Society* (2011).

4. Jiang, H. Y., **Si, F. W.**, Margolin, W. & Sun, S. X. Mechanical control of bacterial cell shape. *55th Annual Meeting of the Biophysical-Society* (2011).

Techinical Expertise

Protocols

Cell biology	Culture, staining, transfection and microscopy
	Cell confinement in micropattern
	Cell migration in 1D channel
	Cell migration and proliferation in 3D matrix
	Mechanical compression test of mammalian cell in microfluidic device
	3D shape of live cell by using 3D confocal
	or epi-fluorescence+negative staining
Microbiology	Bacterial cell culture, staining and microscopy

	Single bacterial cell cycle monitoring in microfluidic device
	Spheroplast form culture and manipulation
	Mechanical compression test of bacterial cell in microfluidic device
	Manipulation of single bacterial cell by magnetic tweezers

Experimental Techniques

Microfluidics	Soft-lithography
	Micropatterning
	Wet etching
Light Microscopy	Epi-fluorescence microscopy
	Confocal microscopy
	Spinning disk microscopy
	Multi-photon microscopy
	Total internal reflection fluorescence microscopy (TIRF)
	Polarized fluorescence microscopy (PFM)
	Super-resolution microscopy
	(e.g. Photoactivated localization microscopy or PALM)
	Fluorescence recovery after photobleaching (FRAP)
	Forster resonance energy transfer (FRET)
Electron Microscopy	Transmission electron microscope (TEM)
	Scanning electron microscope (SEM)

	Environmental scanning electron microscope (ESEM)
Spectroscopy	Fluorescence correlation spectroscopy (FCS)
	Fourier transform infrared spectroscopy (FTIR)
Micro-manipulation	Magnetic tweezers
Mechanical tests	Atomic force microscopy (AFM)
	Nanoindentation
	Tensile testing

Computation, Design and Programing

Computation	Finite element method (FEM) in COMSOL or Abaqus
	Finite difference method (FDM) in Matlab
	Imaging processing in Matlab
Design	Computer-aided design (CAD) in AutoCAD
Programming	C, C++ and Matlab

Awards and Fellowships

Departmental fellowship by Johns Hopkins University Mechanical Engineering. (2009-2010)

Dean's Award by Peking University for Academic Excellence. (2008).

Tung OOCL Scholarship by Peking University and Hong Kong Tung Foundation (2008).

Dean's Award by Peking University for Social Work Excellence (2006).

Teaching Experience

Spring 2014	Teaching assistant of ME.530.231 - Mechanical engineering thermodynamics, Johns Hopkins University Mechanical Engineering Department
Fall 2013	Teaching assistant of ME.530.231 - Mechanical engineering thermodynamics, Johns Hopkins University Mechanical Engineering Department